



## EDITORIAL BOARD

E.O. Paton Electric Welding Institute, Kyiv, Ukraine:

**B.E. Paton** (*Editor-in-Chief*),

**S.I. Kuchuk-Yatsenko** (*Deputy Editor-in-Chief*),

**V.M. Lipodaev** (*Deputy Editor-in-Chief*),

**O.M. Berdnikova, Yu.S. Borisov,**

**V.V. Knysh, V.M. Korzhyk, I.V. Krivtsun,**

**Yu.M. Lankin, L.M. Lobanov, S.Yu. Maksimov,**

**M.O. Pashchin, V.D. Poznyakov,**

**I.O. Ryabtsev, K.A. Yushchenko;**

**V.V. Dmitrik, NTUU**

«Kharkiv Polytechnic Institute», Kharkiv, Ukraine;

**V.V. Kvasnitsky, NTUU**

«Igor Sikorsky Kyiv Polytechnic Institute»,

Kyiv, Ukraine;

**E.P. Chvertko, NTUU**

«Igor Sikorsky Kyiv Polytechnic Institute»,

Kyiv, Ukraine;

**M.M. Student, Karpenko Physico-Mechanical**

Institute, Lviv, Ukraine;

**M. Zinigrad, Ariel University, Israel;**

**Ya. Pilarczyk, Welding Institute, Gliwice, Poland;**

**U. Reisgen, Welding and Joining Institute,**

Aachen, Germany

### Founders

E.O. Paton Electric Welding Institute

International Association «Welding»

### Publisher

International Association «Welding»

### Translators

A.O. Fomin, I.M. Kutianova

### Editor

N.G. Khomenko

*Electron galley*

D.I. Sereda, T.Yu. Snegiryova

### Address

E.O. Paton Electric Welding Institute,

International Association «Welding»

11 Kazymyr Malevych Str. (former Bozhenko),

03150, Kyiv, Ukraine

Tel./Fax: (38044) 200 82 77

E-mail: journal@paton.kiev.ua

www://patonpublishinghouse.com/eng/journals/tpwj

State Registration Certificate

KV 4790 of 09.01.2001

ISSN 0957-798X

DOI: <http://dx.doi.org/10.37434/tpwj>

### Subscriptions

12 issues per year, back issues available.

\$384, subscriptions for the printed (hard copy) version, air postage and packaging included.

\$312, subscriptions for the electronic version (sending issues of Journal in pdf format or providing access to IP addresses).

Institutions with current subscriptions on printed version can purchase online access to the electronic versions of any back issues that they have not subscribed to.

Issues of the Journal (more than two years old) are available at a substantially reduced price.

All rights reserved.

This publication and each of the articles contained herein are protected by copyright.

Permission to reproduce material contained in this journal must be obtained in writing from the Publisher.

## CONTENTS

### SCIENTIFIC AND TECHNICAL

*Boyi Wu and Krivtsun I.V.* Processes of nonconsumable electrode welding with welding current modulation (Review). Part III. Modeling of the processes of TIG welding by modulated current ..... 2

*Milenin O.S., Velikoivanenko O.A., Kozlitina S.S., Kandala S.M. and Babenko A.E.* Numerical prediction of the state of beam products of different thickness during layer-by-layer electron beam surfacing ..... 14

*Bernatskii A.V., Shelyagin V.D., Siora O.V., Sydorets V.M. and Berdnikova O.M.* Impact of spatial position in laser welding on quality level of welded joints of AISI 321 steel ..... 24

*Adzhamsky S.V. and Kononenko G.A.* Regularities of influence of SLM process parameters on the formation of single layer from the high-temperature nickel alloy Inconel 718 ..... 31

*Knysh V.V., Solovei S.O., Nyrkova L.L., Gryshanov A.O. and Kuzmenko V.P.* Impact of high-frequency peening and moderate climate atmosphere on cyclic fatigue life of tee welded joints with surface fatigue cracks ..... 37

### INDUSTRIAL

*Kachynskiy V.S., Kuchuk-Yatsenko S.I. and Koval M.P.* Press magnetically-impelled arc welding of high-strength steel tubular parts of hydraulic cylinders ..... 43

*Skryabinskyi V.V., Nesterenkov V.M. and Rusynyk M.O.* Electron beam welding with programming of beam power density distribution ..... 49

*Khaskin V.Yu., Korzhyk V.M., Dong Ch. and Illyashenko E.V.* Improvement of the effectiveness of laser welding processes by reciprocating movement of the focus ..... 54

*Kostornoy O.S. and Laktionov M.O.* Arc and plasma-powder surfacing of sealing surfaces of pump impellers ..... 61

### INFORMATION

International Cooperation ..... 64

# PROCESSES OF NONCONSUMABLE ELECTRODE WELDING WITH WELDING CURRENT MODULATION (Review)

## Part III. Modeling of the processes of TIG welding by modulated current

Boyi Wu<sup>1</sup> and I.V. Krivtsun<sup>2</sup>

<sup>1</sup>Guangdong Institute of Welding (China-Ukraine E.O. Paton Institute of Welding)

363 Chiansin Str., 510650, Guangzhou, Tianhe. E-mail: wuby@gwi.gd.cn

<sup>2</sup>E.O. Paton Electric Welding Institute of the NAS of Ukraine

11 Kazymyr Malevych Str., 03150, Kyiv, Ukraine. E-mail: office@paton.kiev.ua

A review of investigations devoted to the processes of inert-gas nonconsumable electrode welding with welding current modulation was performed. The third part of the review is devoted to analysis of the works, dealing with theoretical study and mathematical modeling of the processes of heat-, mass- and electric transfer in arc plasma and welded metal in TIG welding by modulated current. Different approaches to theoretical study of the above-mentioned processes are described, as well as respective mathematical models, allowing for the conditions of nonconsumable electrode welding with low-frequency (up to 10 Hz) and high-frequency (above 10 kHz) pulse modulation of welding current. Results of numerical analysis of the distributed and integral characteristics of an argon arc with refractory cathode at pulse variation of current are given. It was performed on the base of models of a nonstationary arc with distributed and concentrated parameters. Results of computer modeling of thermal, hydrodynamic and electromagnetic processes in the welded metal (also at self-consistent accounting of the processes that proceed in arc plasma) were analyzed for the case of spot TIG welding with low-frequency pulse modulation of current. Presented are the analytical dependencies that describe the impact of the shape and parameters of welding current pulses on the characteristics of dynamic action of an arc with a refractory cathode on weld pool metal. 21 Ref., 4 Tables, 19 Figures.

*Keywords:* arc with refractory cathode, TIG welding, arc plasma, metal being welded, penetration, welding current modulation, pulse, frequency, duty cycle, amplitude, mathematical modeling

The features of arc burning, metal penetration and weld formation in nonconsumable electrode welding with welding current modulation, considered in the first [1] and second [2] parts of this review, which were established experimentally, required conducting theoretical investigations, development of mathematical models and numerical modeling of the above-mentioned processes, in order to clarify and predict the nature of their passage at practical realization of different technologies of TIG welding by modulated current.

In work [3] it is assumed that the effect of the arc contraction at HFP modulation of current, which is observed experimentally, and increase of its pressure on weld pool surface, compared with an arc of direct current, equal to average value of modulated current, is related to increase of effective value of modulated current, compared to its average value. This assumption is written as the following ratio

$$P_{PC} = P_{DC} \frac{I_{eff}^2}{I_{av}^2}, \quad (1)$$

where  $P_{PC}$  is the pressure of modulated current arc;  $P_{DC}$  is the pressure of direct current arc;  $I_{eff}$ ,  $I_{av}$  is the effective and average value of current.

By the data of work [3], the thus calculated arc pressure at HFP modulation of current fits in well with experimental data.

At modulation of arc current by rectangular and triangular pulses the square of effective value of current can be approximately calculated as follows:

$$I_{eff}^2 \approx I_p I_{av} \quad (2)$$

for rectangular pulses and

$$I_{eff}^2 \approx \frac{2}{3} I_p I_{av} \quad (3)$$

for triangular pulses, where  $I_p$  is the peak value of current (when writing (2), (3), it was assumed that base current value  $I_b$  is much smaller than  $I_p$ ).

As in the frequency range  $f = 10\text{--}20$  kHz the pulse shape is close to a triangular one, peak current at fixed power of the power source (by direct current) can be assessed by the following ratio:

$$I_p \sqrt{\frac{I_{av}}{fL}}, \quad (4)$$

where  $L$  is the welding circuit inductance.

In this case, using (1), (3), (4), the ratio of pressure of an arc with HFP modulation of current to that of an arc of direct current (that characterizes the degree of arc constriction) can be presented in the following form

$$\frac{P_{PC}}{P_{DC}} \sim \sqrt{\frac{1}{I_{av} f L}}. \quad (5)$$

Thus, the effect of arc constriction at HFP modulation of current is the most pronounced in the cases of small values of average current.

Work [4] is devoted to comparative analysis of pressure on weld pool surface that is applied by an arc with nonconsumable electrode at pulse modulation of welding current and by an arc of direct current, the value of which is determined under the condition of equal power of the considered arcs. At evaluation of arc pressure the authors used the assumption that the current channel has the shape of a truncated cone with the height equal to arc length that expands from the cathode, where the channel radius is selected equal to  $r_0$  towards the anode where the radius is equal to  $R$  ( $R > r_0$ ). It is assumed that the current density is uniformly distributed over the cross-section of the current channel. This allows writing the pressure of an arc of constant current  $I_c$  on the anode surface in the following form

$$P_C = \frac{\mu I_c^2}{4\pi^2 R^2} \ln\left(\frac{R}{r_0}\right), \quad (6)$$

where  $\mu$  is the universal magnetic constant.

The power of constant current arc is defined as the product of current  $I_c$  by voltage  $U(I_c)$  that is calculated using the approximation of the measured experimental static volt-ampere characteristics (VAC) of the arc:

$$U(I) = B_1 I + B_2 + B_3 / I, \quad (7)$$

where  $B_1, B_2, B_3$  are the constant coefficients, which depend on arc burning conditions.

In view of [7], the power of an arc of constant current  $I_c$  can be written as follows:

$$W_C = B_1 I_c^2 + B_2 I_c + B_3. \quad (8)$$

In the case of an arc of modulated current, assuming that modulation is performed by rectangular pulses with duty cycle  $\delta$ , the average and effective value of current can be calculated by the following expressions:

$$I_{av} = \delta I_p + (1 - \delta) I_b; I_{eff} = \left[ \delta I_p^2 + (1 - \delta) I_b^2 \right]^{1/2}, \quad (9)$$

where  $I_p, I_b$  are the peak and base current values.

Average value of power of such an arc  $W_p \equiv \frac{1}{T} \int_0^T I(t)U(t)dt$  in work [4] is defined under the condition that the change of arc voltage in time at the change of current takes place along a static VAC (7) that gives

$$W_p = B_1 I_{eff}^2 + B_2 I_{av} + B_3. \quad (10)$$

It should be noted that the last assumption essentially limits the modulation frequency, with increase of which the change of voltage at the change of arc current that occurs in keeping with a dynamic VAC of the arc, differs ever more from dependence (7) [5].

Comparing expressions (8) and (10), the authors find duty cycle  $\delta$  which at set  $I_c, I_p, I_b$  values provides the condition of equality of powers of the arc for constant and modulated current:

$$\delta = \frac{B_1 (I_c^2 - I_b^2) + B_2 (I_c - I_b)}{B_1 (I_p^2 - I_b^2) + B_2 (I_p - I_b)}. \quad (11)$$

Assuming further that the dimensions of the current channel of an arc with pulse modulation of current are equal to respective dimensions for an arc of constant current and using expression (6), the authors of [4] write

$$P_P = \frac{\mu I_{eff}^2}{4\pi^2 R^2} \ln\left(\frac{R}{r_0}\right), \quad (12)$$

that leads them to a conclusion, similar to the one made in work [3] (see (1)), namely:

$$P_R \equiv P_P / P_C = I_{eff}^2 / I_c^2. \quad (13)$$

Using the obtained relationships, work [4] gives the calculated dependencies of  $P_R, W_p, I_{eff}/I_{av}$ , as well as  $I_c, I_{av}, I_{eff}$  on the duty cycle at the following parameters of arc burning mode: arc length of 1 mm, shielding gas Ar,  $I_p = 500$  A,  $I_b = 5$  A. For instance Figure 1 gives dependence  $P_R(\delta)$  which shows that pressure on the surface of the anode of an arc with pulse modulation of current at small values of the duty cycle can be ten and more times higher than the relative value of an arc of constant current ( $\delta = 1$ ).

In work [6] a computer modeling of thermal, hydrodynamic and electromagnetic processes in metal being welded was performed at spot argon-arc welding (welding by a stationary arc) of a sample from 3 mm stainless steel AISI 304 by an arc burning at constant current and with low-frequency modulation of welding current by rectangular pulses. The follow-

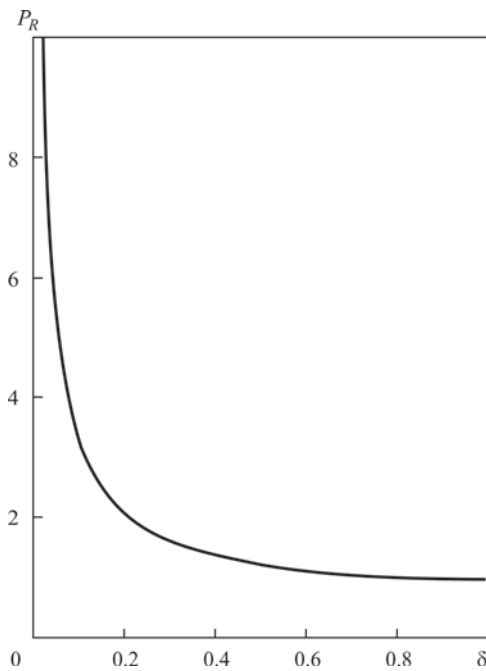


**Figure 1.** Dependence of the ratio of pressure on the anode surface of modulated current arc to pressure of a direct current arc on the duty cycle at the same power ( $I_b = 5$  A,  $I_p = 500$  A, 1 mm arc length) [4]

ing assumptions were used when constructing the mathematical model: 1) considered system is assumed to be axisymmetric; 2) molten metal is a viscous liquid which is incompressible, its flow in the weld pool is laminar; 3) at analysis of hydrodynamic processes in the metal pool the Lorenz and Archimedean forces acting in the pool volume were taken into account, as well as Marangoni force, pressure and force of friction

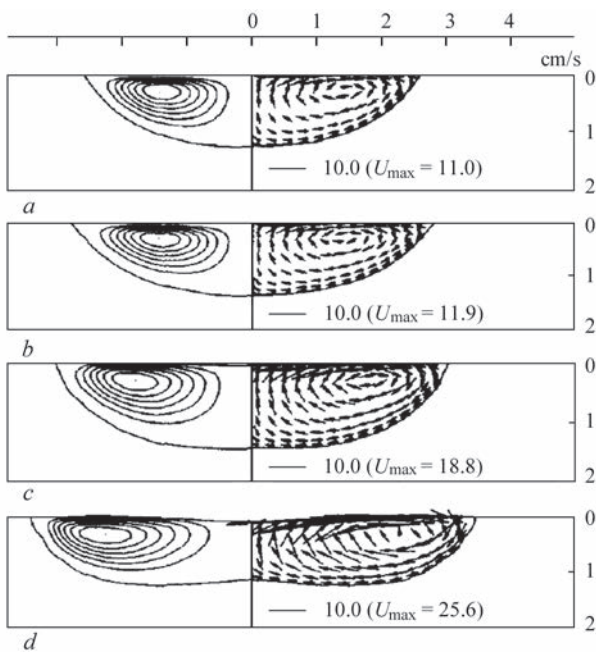


**Figure 2.** Patterns of the flow (left) and fields of movement velocities (right) of the melt at the action on welded metal for 1.92 s: a — direct current arc (100 A); b–d — modulated current arc (variants 1–3 in Table 1, respectively) [6]

**Table 1.** Parameters of burning mode of an arc with current modulation [6]

| Parameter                   | Variant 1 | Variant 2 | Variant 3 |
|-----------------------------|-----------|-----------|-----------|
| Base current $I_b$ , A      | 36        | 40        | 48        |
| Pause duration $t_b$ , s    | 0.16      | 0.24      | 0.32      |
| Peak current $I_p$ , A      | 120       | 136       | 160       |
| Pulse duration $t_p$ , s    | 0.32      | 0.24      | 0.16      |
| Effective current $I_E$ , A | 100       | 100       | 100       |
| Mean current $I_M$ , A      | 92        | 88        | 85        |
| Duty cycle $r_I$            | 0.67      | 0.50      | 0.33      |
| Frequency $F_I$ , Hz        | 2.08      | 2.08      | 2.08      |
| Ratio $t_p/t_b$             | 2.0       | 1.0       | 0.5       |
| Ratio $I_M/I_E$             | 0.92      | 0.88      | 0.85      |

of arc plasma on the pool surface; 4) welded metal properties are assumed independent on temperature, except for the surface tension factor, density, specific heat capacity and heat conductivity factor; 5) distribution of the heat flow, electric current density, pressure and force of friction of arc plasma on the surface of the metal being welded were determined on the base of the results of modeling a constant current arc [7, 8] at different current values (quasistationary arc).

Numerical modeling was performed using the parameters of the mode of burning of an arc of modulated current (Table 1) and constant current given below.

**Параметри режиму горіння дуги постійного струму [6]**

|                                     |            |
|-------------------------------------|------------|
| Arc length, mm                      | 2.0        |
| Arc current, A                      | 100        |
| Arc voltage, V                      | 14.0       |
| Electrode                           | W + 2 % Th |
| Electrode diameter, mm              | 3.2        |
| Electrode sharpening angle, deg     | 60         |
| Nozzle diameter, mm                 | 12.7       |
| Shielding gas flow rate (Ar), l/min | 10.0       |

Figure 2 shows patterns of the flow and fields of velocities (cm/s) of weld pool liquid metal (arc of direct and modulated current) for 1.92 s.

Results of conducted in work [6] computer modeling allowed the authors to conclude that increase of  $t_p/t_b$  ratio or duty cycle results in increase of penetration depth at other conditions being equal.

Work [9] is also devoted to modeling the processes proceeding in the metal being welded at TIG welding with low-frequency modulation of arc current. Thermal, hydrodynamic and electromagnetic processes in a 3 mm sample of stainless steel 304 were considered at the following parameters of the welding mode: arc voltage  $U = 13$  V, welding current is modulated by rectangular pulses, durations of the pulse  $t_p$  and pause  $t_b$  were assigned as  $t_p = t_b = 1$  s, pulse current  $I_p = 170$  A, base current  $I_b = 35$  A, welding speed  $v = 1.6$  mm/s. The mathematical model was constructed

using the following assumptions: 1) weld pool metal is assumed to be a viscous incompressible liquid, flowing mode is laminar; 2) distributions of the heat flow, current density and arc pressure on the sample surface are Gaussian; 3) properties of the metal being welded are independent on temperature, except for the melt surface tension factor (in order to allow for Marangoni effect); 4) weld pool surface is considered to be flat.

Figure 3 shows the calculated dependencies of penetration depth and weld half-width on welding time. As follows from the presented curves, the most marked changes of weld depth and width with the change of arc current are observed at the very start of the welding process ( $t < 4$  s). After four periods of welding current alternation the amplitude of oscillation of the considered characteristics somewhat decreases, their maximum and minimum values becoming practically independent on time.

In order to verify the developed model, the authors of [9] performed comparison of calculated data with experimental ones, obtained by video recording of weld pool surface. As it was impossible to conduct such video recording during the action of current pulse  $I_p$ , Figure 4 gives the data on the change of weld width only during arc burning at minimum current  $I_b$ . Comparison of calculated and experimental data showed their quite satisfactory agreement.

Book [10] is devoted to detailed description of the currently available approaches and mathematical models used for modeling the thermal and hydrodynamic processes in the metal being welded at different methods of arc (MIG/MAG, TIG) and plasma welding. The equations of the respective mathematical models are written in a nonstationary form that allows using them for modeling the processes of arc welding both by constant current and with pulse modulation of arc current.

In works [11, 12] a detailed numerical study was performed of the processes of spot TIG welding (welding by a stationary heat source) of stainless steel AISI 304 at low-frequency modulation of welding current by rectangular pulses in the form of a meander. Work [11] proposes a 2D model of thermal, hydrodynamic and electromagnetic processes in the metal being welded at its partial (10 mm thick sample) and complete (4 mm thick sample) penetration. When constructing the model, the authors used the following assumptions: 1) considered system has axial symmetry; 2) molten metal is a viscous incompressible liquid, flow mode is laminar; 3) metal flow in the weld pool forms due to action of Archimedean, Lorenz and Marangoni forces (force of friction of plasma flow against the melt surface is ignored), as

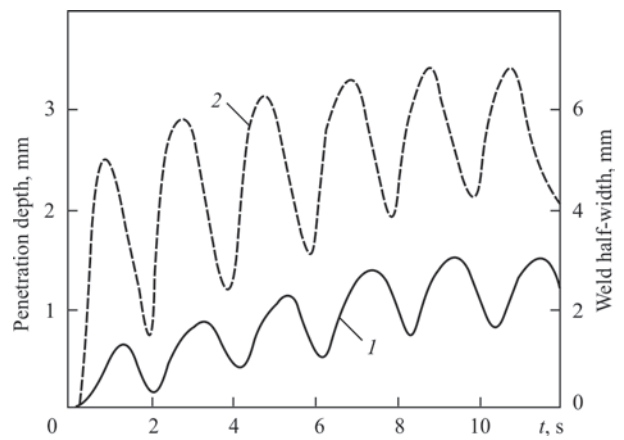


Figure 3. Dependencies of penetration depth ( $I$ ) and weld half-width ( $2$ ) on time [9]

well as pressure of arc plasma on the pool surface; 4) the energy equation takes into account the latent heat of melting-solidification; 5) characteristics of the electromagnetic field in the metal being welded are defined taking into account the eddy currents. Distributions of electric current density, heat flow and arc pressure on the welded metal surface required for determination of boundary conditions on this surface, were assigned based on the respective distributions for direct current arcs in the range of 80–200 A. However, the authors of [11] did not specify the reference from which these data were taken. Calculations were conducted using the parameters of pulse modulation of welding current given below. Weld pool behaviour was considered for 3.5 s from the start of the welding process (7, 14 and 21 modulation period at 2, 4, and 6 Hz frequency, respectively).

**Parameters of arc current modulation [11]**

|   |       |                    |
|---|-------|--------------------|
| Maximum peak value of current $I_p$ , A | ..... | 200                |
| Minimum base value of current $I_b$ , A | ..... | 80                 |
| Pulse duration $t_p$ , s                | ..... | 0.25; 0.125; 0.083 |
| Pause duration $t_b$ , s                | ..... | 0.25; 0.125; 0.083 |
| Frequency $f$ , Hz                      | ..... | 2; 4; 6            |

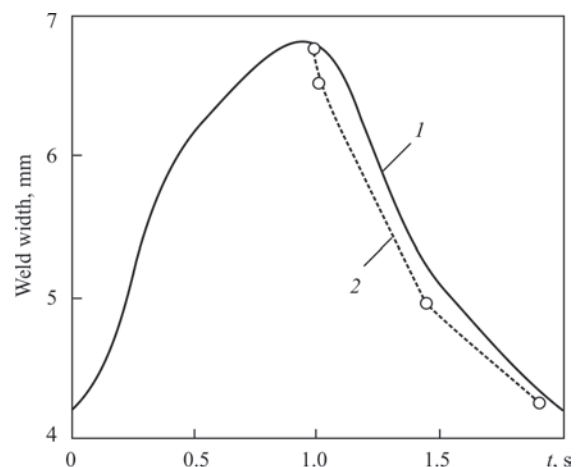
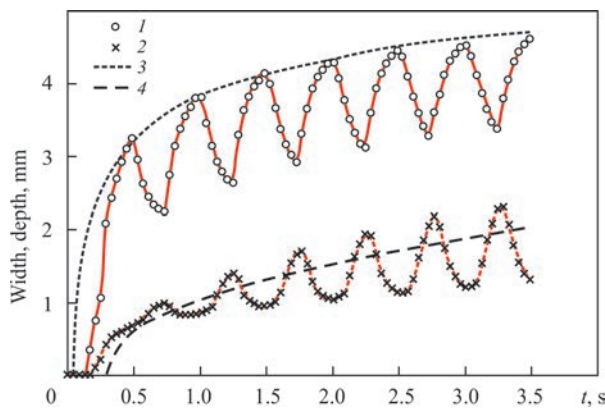


Figure 4. Comparison of calculated ( $I$ ) and experimental ( $2$ ) dependence of weld width on time for one period of welding current modulation [9]



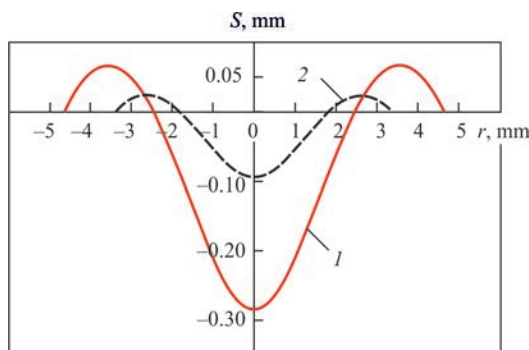
**Figure 5.** Time dependencies of penetration width (1) and depth (2) in TIG welding by modulated current, compared to penetration width (3) and depth (4) in direct current welding [11]

Figure 5 presents calculated dependencies of penetration width (weld spot diameter) and depth during welding 10 mm sample at pulse modulation of arc current in the range of 80–200 A (140 A average current) that is performed at 2 Hz frequency, compared to the respective dependencies at spot welding by constant current of 170 A.

The calculated data given in this Figure show that the change in time of weld pool maximum diameter at pulse modulation of arc current corresponds to the behaviour of pool diameter in welding at constant current of 170 A. At the same time, the energy applied to the sample during 3.5 s is equal to 4565 J in the first case, whereas in the second case this energy turns out to be much greater and equal to 5867 J, that is an important advantage of TIG welding with pulse modulation of current, as it allows lowering the residual stresses and strains.

Another important feature of TIG welding by modulated current is a considerable change of weld pool surface shape in time. Characteristic shapes of the pool surface during the pulse and pause of current for the above modulation mode are shown in Figure 6.

Figure 7 gives the calculated data on time dependence of weld pool dimensions at complete penetration of 4 mm sample in the case of spot welding



**Figure 6.** Shapes of weld pool surface at peak (1 — 200 A) and base (2 — 80 A) values of arc current after six periods of modulation at 2 Hz frequency [11]

with pulse modulation of arc current in the range of 80–200 A at 2 Hz frequency.

In order to verify the proposed model, the calculated geometrical dimensions and shape of penetration of a 10 mm sample at the action of a modulated current arc on it for 3.5 s were compared with the respective dimensions and shape of macrosections of weld spots, determined experimentally. The results of such a comparison are given in Figure 8 for different values of current modulation amplitude (average value of current of 140 A) at the frequency of 2 Hz. These results are indicative of sufficient adequacy of the mathematical model, proposed by the authors [11].

In work [12] the considered model was generalized for self-consistent accounting for the processes that proceed in the electrode (cathode), arc column and metal being welded at spot TIG welding with a low-frequency modulation of current. Such a generalized model was used to perform a detailed computer modeling of the above-listed processes in welding samples of the same steel (AISI 304) 8 and 4 mm thick by a 3 mm argon arc with tungsten cathode of 3.2 mm diameter (sharpening angle of 60 deg) at the following parameters of current modulation: rectangular pulses in the form of a meander, repetition rate of 1 Hz; pulse current  $I_p = 160$  A, pause current  $I_b = 80$  A.

Figure 9, a gives the results of comparison of the dynamics of the change in time of weld pool half-width calculated on the base of model [12], and determined experimentally by video recording of weld pool surface, at spot TIG welding of an 8 mm sample by an argon arc of modulated current with the above-given parameters. Figure 9, b shows the calculated shape and dimensions of penetration zone of the metal being welded, as well as the respective macrosection of the weld spot, achieved during 15 s of the arc action on the sample being welded. As follows from com-

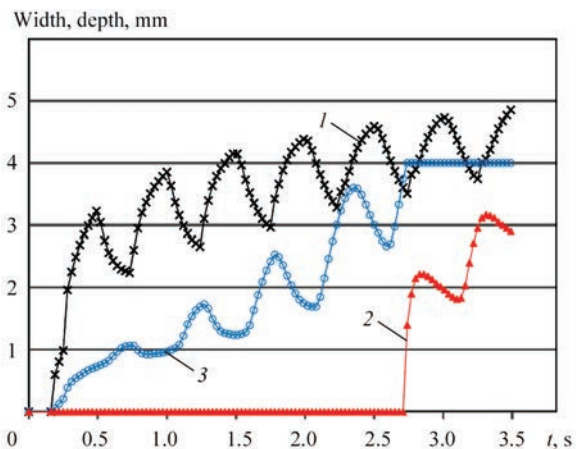


**Figure 7.** Time dependencies of weld pool width from the face (1) and reverse (2) sides of the sample, as well as penetration depth (3) at spot TIG welding by modulated current with complete penetration [11]

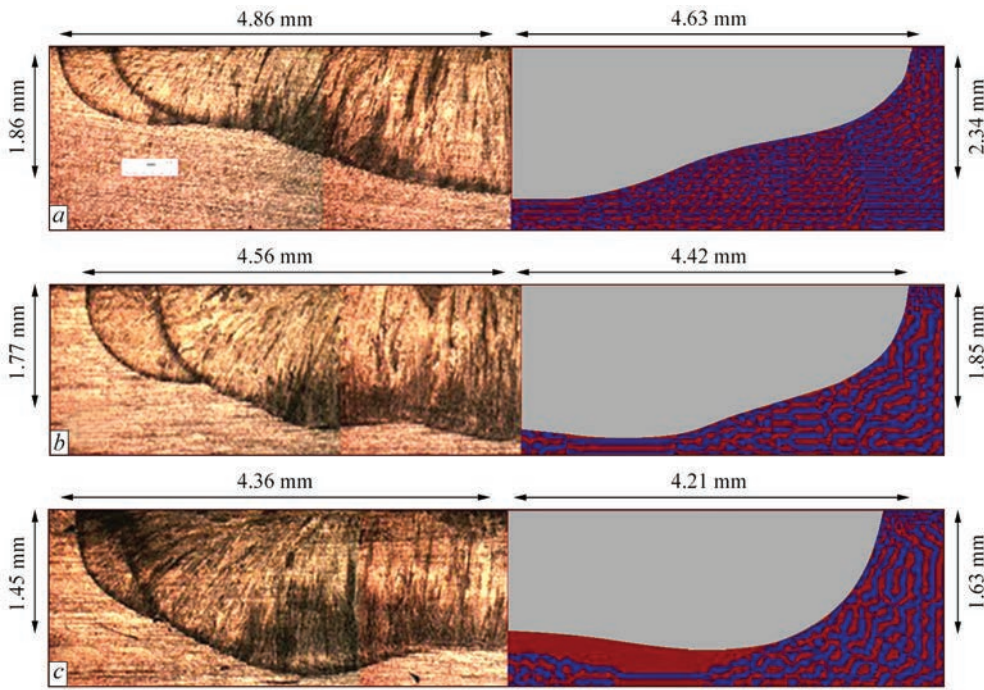


**Figure 8.** Macrosections of weld spots (left) and calculated shapes of metal penetration (right) at spot TIG welding of samples from steel AISI 304 with low-frequency modulation of current in the following range: *a* — 80–200; *b* — 100–180; *c* — 120–160 A [11]

parison of modeling results and experimental data, the proposed by the authors [12] mathematical model allows predicting with a high accuracy, both the dynamics of the change of geometrical characteristics of the weld pool, and the resultant shape of the penetration zone, achieved in a certain time.

Work [13] of the Chinese scientists is devoted to studying the electromagnetic force that acts on the arc plasma at TIG welding with high-frequency ( $f = 20\text{--}80\text{ kHz}$ ) pulse modulation of welding current.

The authors assume that the current density in the arc column has, as shown in Figure 10 an axial and radial components, and is distributed by Gaussian law:

$$\begin{cases} J_z = \frac{Id}{\pi R_r^2} \exp\left(-\frac{r^2 d}{R_r^2}\right); \\ J_r = J_z \operatorname{tg}\varphi, \end{cases} \quad (14)$$

where  $I$  is the arc current;  $d = 3$  is the concentration coefficient;  $R_r$  is the radius of electrically conducting section of the arc column, which is considered to be conical;  $\varphi$  is the angle of inclination of the current line to the arc axis (see Figure 10). This allows writing the expressions for the components of electromagnetic force acting on the plasma, in the following form:

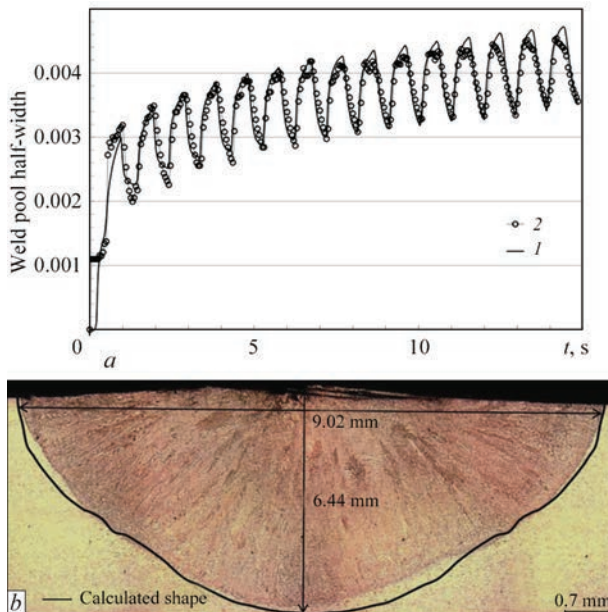


**Figure 9.** Comparison of calculated (*I*) and experimental (2) data by the dynamics of the change of weld pool half-width (*a*) and resultant form of penetration zone (*b*) in spot TIG welding by modulated current [12]

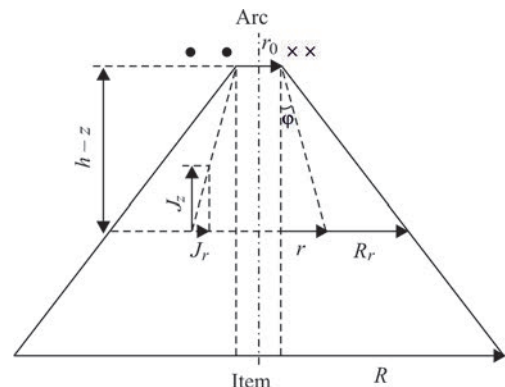


**Figure 10.** Scheme of distribution of current density in the arc column [13]

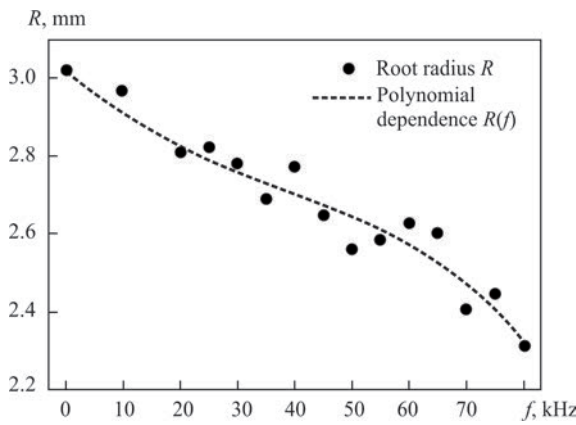


**Figure 11.** Arc root radius, depending on current modulation frequency [13]

$$\begin{cases} F_r = C_1 t \exp(-t) [1 - \exp(-t)]; \\ F_z = 0, (r \leq r_0); C_2 t \exp(-t) [1 - \exp(-t)], \\ (r \geq r_0). \end{cases} \quad (15)$$

Here  $t = r^2 d / R_r^2$ ;  $C_1 = -\mu I^2 / (2\pi^2 r^2 (h - z))$ ;  $C_2 = -\mu I^2 (r - r_0) / [2\pi^2 r^2 (h - z)]$ ; where  $\mu$  is the magnetic permeability;  $h$  is the arc length; coordinate  $z$  is calculated from the item surface. It should be noted that the expression for  $F_z$  (formulas (4) and (6)) in work [13] is written incorrectly.

Alongside the distributed characteristics of electromagnetic force in the arc column, such an integral characteristic of force action as arc pressure on anode surface, which written in the following form, was also studied in this work (see also [4]):

$$P_{ez} = \frac{\mu I^2}{4\pi^2 R^2} \ln \frac{R}{r_0}. \quad (16)$$

At analysis of this dependence, it is assumed that value  $r_0$  is constant and is equal to half of electrode diameter. Arc root radius  $R$  is determined experimentally by photo recording of the transverse size of the arc anode zone in TIG welding of titanium alloy Ti-6Al-4V 2.5 mm thick with different frequencies of welding current modulation. Experiments were performed using 3 mm argon arc with refractory (W + 2 % Ce) cathode of 2.4 mm diameter; welding mode parameters are given in Table 2.

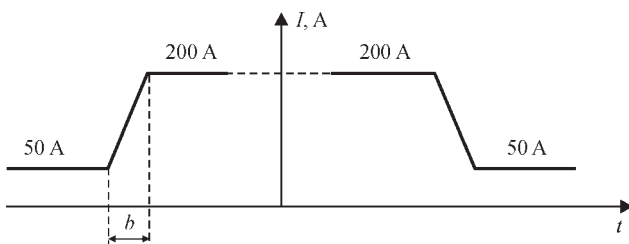


**Figure 12.** Diagram of pulsed change of arc current [14]

**Table 2.** Parameters of the studied welding modes [13]

| Experiment number | Base current $I_b$ , A | Pulse current $I_p$ , A | Frequency $f$ , kHz | Duty cycle $\delta$ , % |
|-------------------|------------------------|-------------------------|---------------------|-------------------------|
| 1                 | 75                     | —                       | —                   | —                       |
| 2–14              | 40                     | 100                     | 20–80               | 50                      |

Figure 11 shows the dependence of arc root radius on current modulation frequency, which is indicative of increase of the degree of arc contraction on the anode (reduction of  $R$ ) with frequency increase. The following polynomial dependence was proposed for approximation of the derived experimental data:  $R(f) = -0.0014f^3 + 0.0307f^2 - 0.2755f + 6.2086$ .

Rewriting formula (16) in the following form

$$P_{ez} = \frac{\mu I^2}{4\pi^2 r_0^2} \frac{1}{n^2} \ln n, \quad \text{where } n = \frac{R}{r_0},$$

and studying this expression, the authors of [13] find that at  $n < 1.6$  (more exactly, at  $n < \exp(1/2)$ ) value  $P_{ez}$  is an ascending function of  $n$ , and at  $n > 1.6$  it is a descending function. It means that the arc pressure on the anode surface becomes greater with increase of  $R$  at  $R < R_c$  and decreases at  $R > R_c$ , where for the set value  $r_0 = 1.2$  mm the critical value of arc root radius  $R_c$  is equal to 1.92 mm.

As, according to experimental data, given in Figure 11, value  $R$  turns out to be greater than  $R_c$  for all the values of modulation frequency and decreases with  $f$  increase, the conclusion is made that with increase of current modulation frequency the pressure of the arc on the weld pool surface rises, that leads to the heat source moving deeper into the metal being welded, and, therefore, to increase of the arc penetrability.

In work [14], the self-consistent mathematical model of nonstationary processes of energy- mass- and electric transfer in the column and anode region of the electric arc with a refractory cathode [15] was the base to perform a detailed numerical analysis of the characteristics of an argon arc with a copper water-cooled anode at pulsed change of electric current (Figure 12).

It is found that arc burning at an abrupt increase (decrease) of current is accompanied by an essential restructuring of the electromagnetic, thermal and gas-dynamic characteristics of arc plasma, as well as the characteristics of its action on the anode surface. Here, the dynamic behaviour of the above-mentioned characteristics depends not only on the rate of arc current change, but also on its increasing or decreasing. Here, at a high rate of current change ( $\left| \frac{dI}{dt} \right| > 5 \cdot 10^6$  A/s) the change of the arc column and anode region characteristics proceeds in two stages,

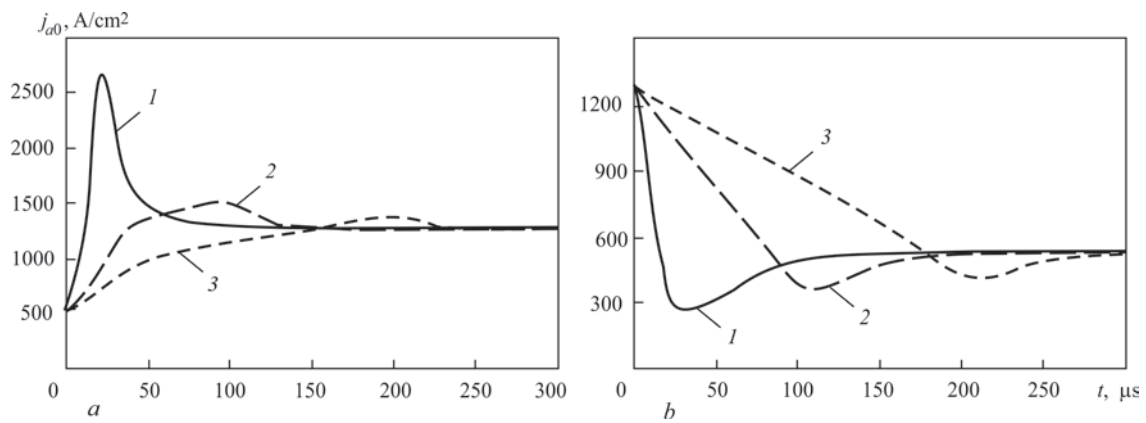


**Figure 13.** Change of axial value of electric current density on the anode at pulsed increase (a) and decrease (b) of arc current ( $I - b = 20$ ; 2 — 100; 3 — 200  $\mu\text{s}$ ) [14]

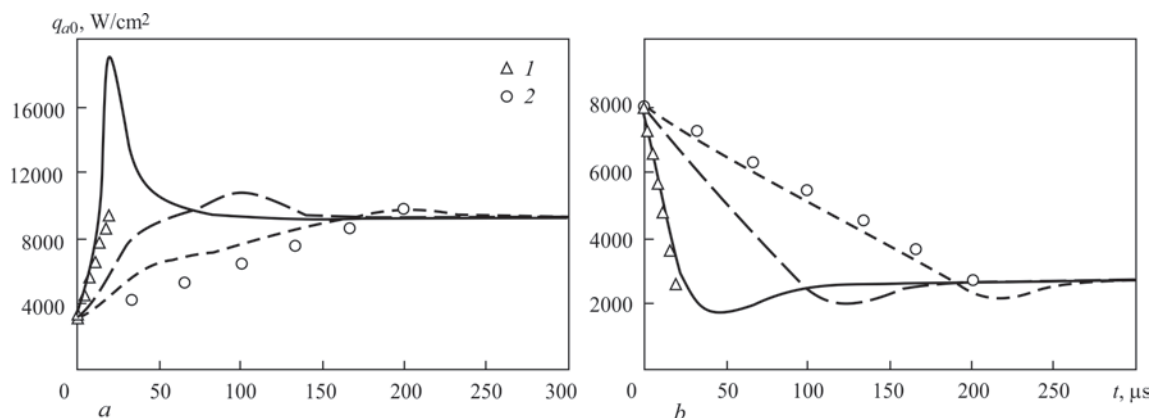


**Figure 14.** Change of axial value of the density of heat flow to the anode at pulsed increase (a) and decrease (b) of arc current (markers show values  $q_{a0}$  for a stationary arc at respective current values: 1 —  $b = 20$ ; 2 — 200  $\mu\text{m}$ ) [14]

namely stage of the change together with arc current and stage of transient processes. As follows from the calculated data given in Figures 13, 14, at increase (decrease) of arc current the density of electric current and heat flow on the anode can become two times higher (1.5 times smaller) than the respective values for an arc of direct current equal to the larger (smaller) value, respectively.

At the transient process stage, relaxation of the thermal and gas-dynamic state of arc plasma to values characteristic for a stationary arc at the respective current value, takes place. Durations of the relaxation processes depend on values of maximum and minimum current, and can differ essentially from the local and integral characteristics of arc column plasma and anode region.

At current change at a rate lower than  $10^6$  A ( $b > 100 \mu\text{s}$ ), the processes associated with increase (decrease) of current and relaxation processes proceed simultaneously. As a result of that the nonstationary process of arc burning is realized in the form of a successive change of states, characteristic for a stationary arc at the respective current values (see, for instance, Figure 14), that is the change of arc characteristics occurs in the quasistationary mode.

Work [16] is devoted to investigation of the impact of high-frequency pulse modulation of current on depression of weld pool surface in TIG welding of samples of 2.5 mm titanium alloy Ti-6Al-4V. This study includes experimental measurement of the force, with which the arc acts on the surface of the sample being welded, and geometrical characteristics of its penetration (weld width  $B$  and penetration depth  $H$ ), as well as mathematical modeling of the processes proceeding in the metal being welded, taking into account the depression of the free surface of the weld pool.

A special test rig, which allows measuring the force acting on the sample in TIG welding, was developed, in order to conduct the experiments. A 3 mm argon arc with refractory (W + 2 % Ce) cathode of 1.2 mm radius was used in the experiments, welding mode parameters are given in Table 3, welding speed

**Table 3.** Welding mode parameters [16]

| Experiment number | Base current $I_b$ , A | Pulse current $I_p$ , A | Frequency $f$ , kHz | Duty cycle $\delta$ , % |
|-------------------|------------------------|-------------------------|---------------------|-------------------------|
| 1                 | 80                     | —                       | —                   | —                       |
| 2                 | 40                     | 100                     | 20                  | 50                      |
| 3                 | 40                     | 100                     | 40                  | 50                      |
| 4                 | 40                     | 100                     | 60                  | 50                      |
| 5                 | 40                     | 100                     | 80                  | 50                      |

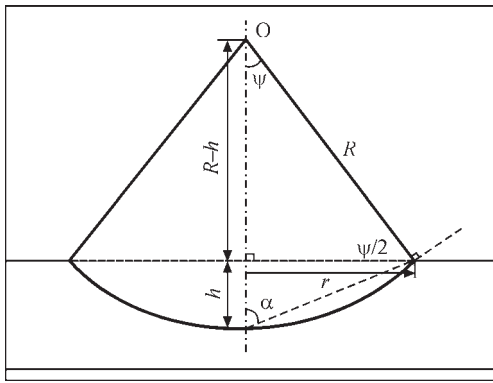


Figure 15. Approximation of weld pool free surface [16]

was constant and equal to 150 mm/min in all the experiments.

For mathematical modeling of thermal, hydrodynamic and electromagnetic processes in the metal being welded, a 2D model was used, which was constructed with the following assumptions: 1) molten metal is a viscous incompressible liquid, its flow in the weld pool is laminar; 2) at analysis of hydrodynamic processes in the weld pool the volumetric forces (Lorenz and Archimedean), as well as surface forces (Marangoni and arc pressure) are taken into account; 3) properties of the material being welded are considered to be independent on temperature, except for specific heat capacity and heat conductivity factor, as well as surface tension factor, viscosity and density of the melt (Boissinesq approximation).

At evaluation of the degree of curving of the weld pool free surface, its approximation by part of a spherical surface was used, as shown in Figure 15.

Writing the balance of forces on this surface, the authors of [16] obtain the following expression:

$$\Phi(h) = F - \frac{\pi}{6} \rho g h^3 - \frac{3\pi}{2} \rho g r^2 h - 8\sigma r \arctg \frac{h}{r}, \quad (17)$$

where  $F$  is the force of arc action on the surface of metal being welded;  $\rho$ ,  $\sigma$  is the density and surface tension factor of the melt;  $g$  is the free fall acceleration;

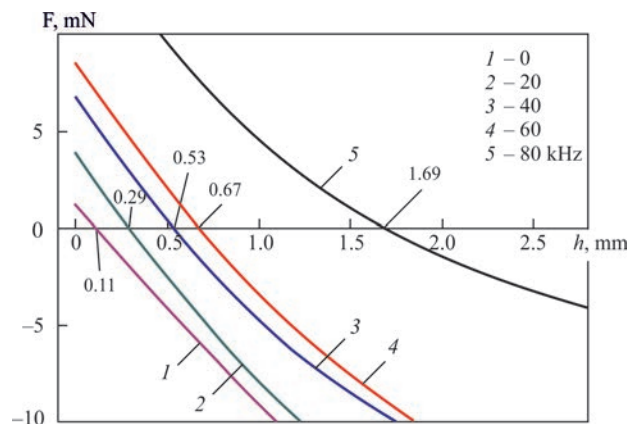


Figure 16.  $F(h)$  dependencies at different values of arc current modulation frequency [16]

tion;  $r$ ,  $h$  are the weld pool radius and depression of its free surface (see Figure 15). The root of equation  $\Phi(h) = 0$  corresponds to value  $h$ , at which the balance of forces is fulfilled (17).

Weld pool radius  $r$ , included into equation (17), was defined as half of experimentally measured value of weld width  $B$ . After that dependencies  $\Phi(h)$  were plotted for different values of modulation frequency, which are presented in Figure 16. The same Figure shows the respective values of the roots of equation  $\Phi(h) = 0$ .

The experimental and calculated values of parameters which determine the depression of weld pool surface are given in Table 4.

Completing the review of work [16], it should be noted that force  $F$ , which is measured experimentally, contains two components — the force proper of action of arc plasma on the metal being welded and force acting on the sample being welded, due to current flowing in its volume (a similar force, acting on arc column plasma, was defined in [4]). Calculations show that, for instance, at arc current, equal to 178 A, the force acting on a sample from 5 mm stainless steel, is equal to 4.4 mN. Thus, the used in [16] values of the force of arc action on weld pool surface, and, hence, of depression of this surface, are much too high.

In work [17] an attempt was made to analyze the force of action of arc plasma flow on the surface of the metal being welded at TIG welding with HFP modulation of arc current. Without any substantiation, the authors assume that the distribution of plasma flow pressure in the area of anode binding of the arc has the following form:

$$P_r = P_{peak} \exp(-a|r|), \quad (18)$$

where  $P_{peak}$  is the gas-dynamic pressure on the arc axis;  $a$  is the distribution coefficient;  $r$  is the radial coordinate. Then the value of the respective force acting on weld pool surface is mathematically incorrectly calculated, and it is compared with experimentally measured (by the procedure described in [16]) value of this force, which, as was noted above, is greatly

Table 4. Values of parameters that determine the weld pool surface depression [16]

| Frequency $f$ , Hz | Force action of the arc $F$ , mN | Weld width $B$ , mm | Penetration depth $H$ , mm | Surface depression $h$ , mm |
|--------------------|----------------------------------|---------------------|----------------------------|-----------------------------|
| 0                  | 1.79                             | 4.16                | 2.29                       | 0.11                        |
| 20                 | 4.19                             | 3.10                | 1.75                       | 0.29                        |
| 40                 | 7.00                             | 2.77                | 1.85                       | 0.53                        |
| 60                 | 8.84                             | 3.21                | 2.15                       | 0.67                        |
| 80                 | 16.06                            | 2.59                | 2.06                       | 1.63                        |

overestimated. Therefore, the conclusions made in work [17] do not seem to be reasonable.

Work [5] is devoted to use of the model of a non-stationary arc with concentrated parameters for analysis of the dynamics of the change of its characteristics in TIG welding at pulsed change of current. When constructing such a model, the Kirchhoff equations, describing the electric circuit, were complemented by equations of the dynamic model of the arc as an element of the electric circuit [18]. Static VAC of the arc column and time constant of the transient process which is to be determined are used as parameters of the model with concentrated parameters. In order to identify these parameters, experimental studies of static VACs of an argon arc with a tungsten cathode and copper water-cooled anode were conducted. Time constant  $\theta$  of the transient process was defined, proceeding from the calculated data on the dynamics of the change of arc voltage, derived using the model with distributed parameters [15].

The impact on the arc of trapezoidal current pulses with different front durations (20; 100; 200  $\mu$ s) was considered. Calculations were conducted for a 3 mm argon arc with a refractory cathode. It was assumed that after current rise (drop) the arc burns at constant current until the steady state sets in. Results of calculation of dynamic VAC of such an arc for models with distributed and concentrated parameters are presented in Figure 17. The same Figure shows the respective values of  $\theta$ , selected by the criterion of the best fit of the results of calculation using the above models.

As follows from the calculated data given in this Figure, the time constant decreases with reduction of the pulse front duration. A characteristic feature of the dynamic VAC of the arc is the fact that it is presented in the form of a hysteresis loop, in which the upper and lower curves correspond to the pulse leading and trailing edges, and the vertical sections — to transition into the arc stationary state. VAC of the arc in the form of a hysteresis loop was derived experimentally in works [19, 20]. The cause for its appearance is the different degree of inertia of the processes of transfer

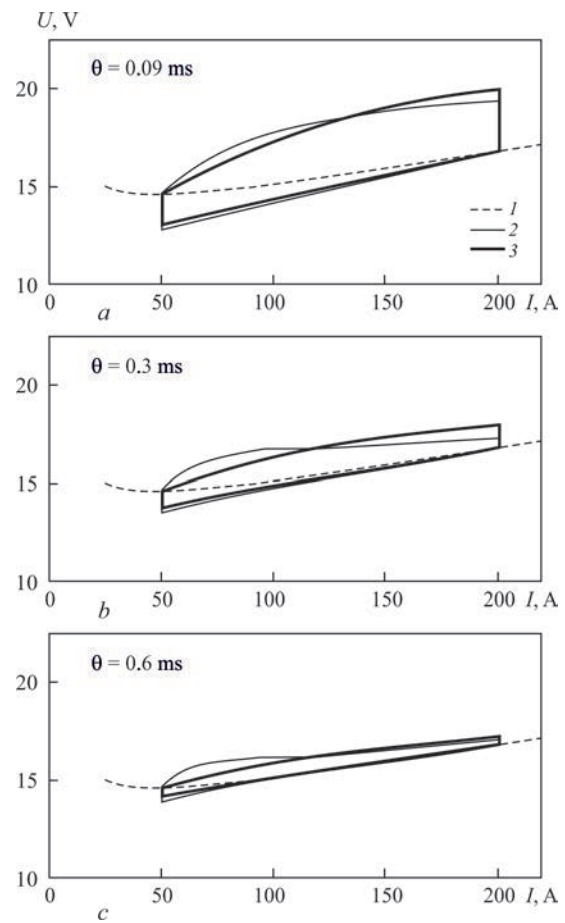


**Figure 17.** Dynamic VACs of the arc at the following duration of pulse fronts: 20  $\mu$ s: (a) 100  $\mu$ s (b) and 200  $\mu$ s (c): 1 — static VAC of the arc; 2 — dynamic VAC of the arc (model with distributed parameters); 3 — dynamic VAC (model with concentrated parameters) [5]

of energy, pulse and charge at current rise and drop. Note that with increase of pulse front duration the range of the hysteresis loop decreases, and dynamic VAC of the arc becomes closer to that of a stationary arc (see Figure 17, c).

Study [12] provides brief analysis of the impact of the parameters of pulse modulation of welding current on the characteristics of dynamic action of an arc with refractory cathode on weld pool metal. It is shown that the larger the square of the acting (effective) value of current  $I_E$ , the greater is the force applied to the molten metal. Thus, in order to ensure the

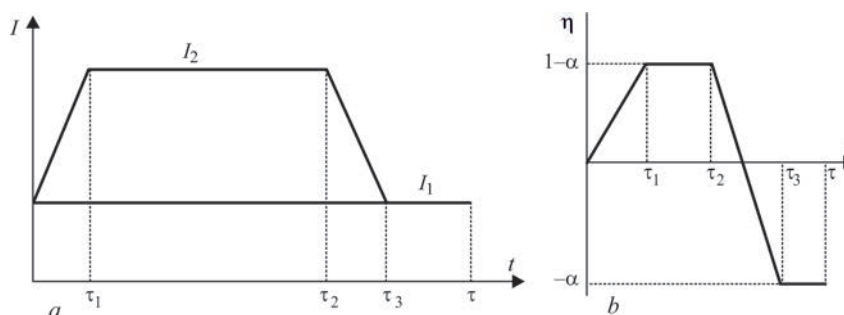


**Figure 18.** Schematic presentation of arc current pulse: a — trapezoidal pulse with a pause; b — respective normalized pulse (function)  $\eta(t)$  [21]

maximum above-mentioned action (at fixed average value of current  $I_A$ ), the shape and time parameters of modulation pulses should be selected by the criterion of  $I_E$  maximum.

For any current  $I(t)$  that periodically changes in time, the following representation is in place:

$$I(t) = I_A + A\eta(t), \quad (19)$$

where  $A = I_2 - I_1$  is the current modulation amplitude;  $I_1, I_2$  are the minimum and maximum values of current;  $\eta(t)$  is a certain normalized function, which contains information on the shape and time parameters of pulses. Considering a rather general case of welding current modulation by pulses of a trapezoidal shape, presented in Figure 18, the authors showed that

$$I_E^2 = I_A^2 + A^2 f(\xi, \gamma); \quad (20)$$

$$f(\xi, \gamma) = \xi \left[ \frac{2}{3}(1 + 2\gamma) - \xi(1 + \gamma)^2 \right],$$

where dimensionless parameters  $\xi = \frac{\tau_3}{2\tau} (0 < \xi \leq \frac{1}{2})$  and  $\gamma = \frac{\tau_2 - \tau_1}{\tau_3} (0 \leq \gamma \leq 1)$  characterize relative pulse duration (equal to half of the duty cycle) and its shape (at  $\gamma = 0$  the trapezoidal pulse becomes triangular, and at  $\gamma = 1$  — it is rectangular, respectively), and the average value of current can be written as  $I_A = (1 - \alpha)I_1 + \alpha I_2$ , where  $\alpha = \frac{\tau_3 + \tau_2 - \tau_1}{2\tau} (0 \leq \alpha \leq 1)$ .

Figure 19 shows the behaviour of function  $f(\xi, \gamma)$ , from the explicit form of which it follows that the effective value of modulated current depends on the duty cycle and shape of pulses and does not depend on the frequency of their flowing. Note also that  $f(\xi, \gamma) \geq 0$ , i.e. the square of effective value of current is always greater than the square of its average value.

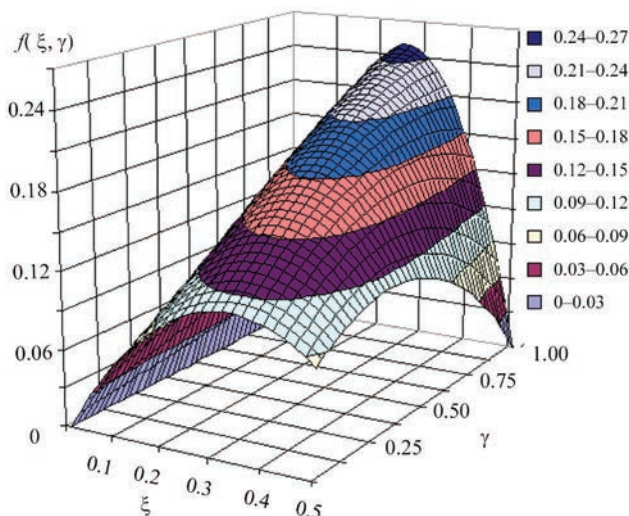


Figure 19. Appearance of function  $f(\xi, \gamma)$  [21]

As follows from (20), in order to ensure maximum value of  $I_E$  at fixed values of  $I_A$  and  $A$ , the parameters should be chosen so that function  $f(\xi, \gamma)$  took the greatest value. For trapezoidal pulses (see Figure 18) parameter  $\alpha$  is equal to  $\xi(1 + \gamma)$ . Therefore, at analysis of function  $f(\xi, \gamma)$  not the entire range of the change of parameters  $\xi, \gamma$ , but just their values satisfying equations  $\alpha = \xi(1 + \gamma)$  should be considered. Expressing from this equation  $\gamma$  through  $\xi, \alpha$ , we get  $f(\xi, \alpha) = \frac{4}{3}\alpha - \alpha^2 - \frac{2}{3}\xi$ . This function decreases monotonically with  $\xi$  increase and has the greatest value at minimum value  $\xi_{\min}$ . In the case of triangular pulses ( $\gamma = 0$ ) we find  $\xi = \alpha$ , and in the case of rectangular pulses ( $\gamma = 1$ ), we have  $\xi = \frac{\alpha}{2}$ . Thus, minimum

value of  $\xi_{\min} = \frac{\alpha}{2}$ , that provides the greatest value of function  $f(\xi_{\min}, \alpha) = \alpha - \alpha^2$  at the set  $\alpha$ , is achieved in the case, when  $\gamma = 0$ . Function  $\alpha - \alpha^2$  has a maximum at  $\alpha = 0.5$ , that gives  $\xi = 0.25$ , i.e. this set of dimensionless parameters corresponds to rectangular pulses in the form of a meander.

As it is impossible to achieve a rectangular shape of current pulses in practice, in [21] the behaviour of function  $f(\xi, \gamma)$  was studied for the case of a trapezoidal current pulse. Designating as  $\tau_f = \tau_1 + \tau_3 - \tau_2$  the total duration of the pulse leading and trailing edges (see Figure 18, a), we can show that the minimum value of  $\xi$  is determined

as follows:  $\xi_{\min} = \frac{\alpha}{2 - \bar{\tau}_f}$ , where  $\bar{\tau}_f = \frac{\tau_f}{\tau_3}$ . Hence,

$f(\xi_{\min}, \alpha) = \frac{2}{3} \left( 2 - \frac{1}{2 - \bar{\tau}_f} \right) \alpha - \alpha^2$ . This function has

a maximum, equal to  $f(\bar{\tau}_f) = \frac{1}{9} \left( 2 - \frac{1}{\bar{\tau}_f} \right)^2$ , at  $\alpha = \frac{1}{3} \left( 2 - \frac{1}{\bar{\tau}_f} \right)$ .

Analysis of the results of the works, devoted to modeling the processes of TIG welding by modulated current, leads to the following conclusions:

1. Results of theoretical analysis of the characteristics of an arc with a refractory cathode at high-frequency pulse modulation of current confirm the effects of arc constriction and increase of pressure of arc plasma flow on the anode surface, compared to that of a direct current arc that was observed experimentally. It is shown, for instance, that the pressure of an arc with HFP modulation of current rises with decrease of the duty cycle (at constant average value of arc power) in proportion to the ratio of squares of effective and average values of modulated current.

2. Mathematical models of thermal, hydrodynamic and electromagnetic processes in the metal being welded (also at self-consistent accounting for the processes proceeding in arc plasma) were developed, according to the conditions of spot TIG welding with low-frequency ( $f < 10$  Hz) modulation of welding current. Detailed computer modeling of the above-mentioned processes was performed, the results of which are in good agreement with the experimental data.

3. The questions of modeling the distributed characteristics of plasma of a nonstationary arc with a refractory cathode and its action on the surface of the metal being welded, in TIG welding with HFP modulation of welding current ( $f > 10$  kHz) is not given sufficient attention in modern scientific-technical publications (except for works [5, 14]). Therefore, it is believed to be rational to conduct detailed theoretical studies and mathematical modeling of the processes of energy-, mass- and electric transfer in the system of «nonstationary arc–metal being welded» at TIG welding with HFP modulation of current.

1. Boyi, Wu, Krivtsun, I.V. (2019) Processes of nonconsumable electrode welding with welding current modulation (Review). Part 1. Peculiarities of burning of nonstationary arcs with refractory cathode. *The Paton Welding J.*, **11**, 23–32.
2. Boyi, Wu, Krivtsun, I.V. (2019) Processes of nonconsumable electrode welding with welding current modulation (Review). Part 2. Effects of arc impact on the metal being welded. *The Paton Welding J.*, **12**, 11–23.
3. Yamaoto, T., Shimada, W., Gotoh, T. (1976) *Characteristics of high frequency pulsed DC TIG welding process*. Doc. IIW 212-628-76, 11–23.
4. Cook, G.E., Eassa, H.E.-D.E.H. (1985) The effect of high-frequency pulsing of a welding arc. *IEEE Transact. on Industrial Application*, 1A-21, **5**, 1294–1299.
5. Sydorets, V.N., Krivtsun, I.V., Demchenko, V.F. et al. (2016) Calculation and experimental research of static and dynamic volt-ampere characteristics of argon arc with refractory cathode. *The Paton Welding J.*, **2**, 2–8.
6. Kim, W.H., Na, S.J. (1998) Heat and fluid flow in pulsed current GTA weld pool. *Int. J. of Heat and Mass Transfer*, **41**(21), 3213–3227.
7. Lee, S.Y., Na, S.J. (1996) A numerical analysis of a stationary gas tungsten welding arc considering various electrode angle. *Weld. J., Res. Suppl.*, 269–279.
8. Kim, W.H., Fan, H.G., Na, S.J. (1997) A mathematical model of gas tungsten arc welding considering the cathode and the free surface. *Metall. Transact.*, **28B**, 679–686.
9. Wu, C.S., Zheng, W., Wu, L. (1999) Modelling the transient behaviour of pulsed current tungsten-inert-gas weld pools. *Modelling and Simul. Mater. Sci. Eng.*, **7**(1), 15–23.
10. Wu, C.S. (2008) *Welding heat process and pool geometry*. Beijing, China Machine Press, 102–104.
11. Traidia, A., Roger, F., Guyot, E. (2010) Optimal parameters for pulsed gas tungsten arc welding in partially and fully penetrated weld pools. *Int. J. of Thermal Sci.*, **49**, 1197–1208.
12. Traidia, A., Roger, F. (2011) Numerical and experimental study of arc and weld pool behaviour for pulsed current GTA welding. *Int. J. of Heat and Mass Transfer*, **54**, 2163–2179.
13. Yang, M., Qi, B., Cong, B. et al. (2013) Study on electromagnetic force in arc plasma with UHFP-GTAW of Ti-6Al-4V. *IEEE Transact. on Plasma Sci.*, **41**(9), 2561–2568.
14. Krivtsun, I.V., Krikent, I.V., Demchenko, V.F. (2013) Modeling of dynamic characteristics of a pulsed arc with refractory cathode. *The Paton Welding J.*, **7**, 13–23.
15. Krikent, I.V., Krivtsun, I.V., Demchenko, V.F. (2012) Modeling of processes of heat-, mass- and electric transfer in column and anode region of arc with refractory cathode. *Ibid.*, **3**, 2–6.
16. Yang, M., Yang, Z., Cong, B. et al. (2014) A study on the surface depression of the molten pool with pulsed welding. *Welding J., Res. Suppl.*, **93**(8), 312–319.
17. Yang, M., Yang, Z., Qi, B. (2015) The effect of pulsed frequency on the plasma jet force with ultra high frequency pulsed arc welding. *IW*, **8**, 875–882.
18. Sydorets, V.N., Pentegov, I.V. (2013) *Deterministic chaos in nonlinear circuits with electric arc*. Kiev, IAW [in Russian].
19. Sokolov, O.I., Gladkov, E.A. (1977) Dynamic characteristics of free and constricted welding arcs of direct current with nonconsumable electrode. *Svarochn. Proizvodstvo*, **4**, 3–5 [in Russian].
20. Trofimov, N.M., Sinitzky, R.V. (1967) Dynamic characteristics of pulsed arc in argon arc welding. *Ibid.*, **8**, 18–19 [in Russian].
21. Demchenko, V.F., Boi, U., Krivtsun, I.V., Shuba, I.V. (2017) Effective values of electrodynamic characteristics of the process of nonconsumable electrode welding with pulse modulation of arc current. *The Paton Welding J.*, **8**, 2–11.

Received 21.12.2019

## NEW BOOK

(2019) «**Beam Technologies in Welding and Materials Processing**»: Proceedings of the Ninth International Conference. Edited by Prof. I.V. Krivtsun. — Kyiv: International Association «Welding», 2019. — 126 p.

Collection in the open access:

<http://patonpublishinghouse.com/proceedings/ltwmp2019.pdf>

Orders for the collection, please send to the Editorial Board.



# NUMERICAL PREDICTION OF THE STATE OF BEAM PRODUCTS OF DIFFERENT THICKNESS DURING LAYER-BY-LAYER ELECTRON BEAM SURFACING

O.S. Milenin<sup>1</sup>, O.A. Velikoivanenko<sup>1</sup>, S.S. Kozlitina<sup>1</sup>, S.M. Kandala<sup>1</sup> and A.E. Babenko<sup>2</sup>

<sup>1</sup>E.O. Paton Electric Welding Institute of the NAS of Ukraine

11 Kazymyr Malevych Str., 03150, Kyiv, Ukraine. E-mail: office@paton.kiev.ua

<sup>2</sup>National Technical University of Ukraine «Igor Sikorsky Kyiv Polytechnic Institute»

37 Peremohy Prosp., 03056. Kyiv, Ukraine

A complex of mathematical models and their computer realization means for numerical prediction of the kinetics of temperature fields, phase and structural states, mechanical stresses and strains in layer-by-layer formation of typical products of titanium-based alloys was developed. The peculiarities of VT6 titanium alloy state kinetics, depending on the technological parameters of production, were investigated on the typical examples of electron beam surfacing of T-shaped beam structures, from these alloys produced by xBeam 3D Metal Printer technology. The impact of the substrate thickness on the regularities of temperature field development during layer-by-layer formation of beam elements and on the structural state of the metal after complete cooling is shown. In the case of forming a thick-walled T-shaped product, it is shown that an important factor that allows obtaining a low level of residual stresses, is optimization of the delay time between deposition of each of the beads, to provide the conditions for uniform cooling of the structure. 11 Ref., 14 Figures.

*Keywords: additive technologies, electron beam surfacing, xbeam 3D Metal Printer, mathematical modeling, macro-structure, mechanical properties, stress-strain state*

Broad introduction of additive technologies is a sustainable modern trend, when designing production schemes of critical structural elements of a complex shape. In particular, the schemes of electron beam surfacing (EBS) of parts from light metals (primarily, titanium and aluminium alloys) for the needs of aerospace industry have found their application [1–3]. xBeam 3D Metal Printer, developed at PJSC

«NVO «Chervona Hvilya» is a characteristic example of realization of such a technology in Ukraine [4]. This technology envisages a layer-by-layer formation of typical products by EBS under deep vacuum that allows effectively focusing the electron beam, and avoiding metal contamination by interstitial impurities in the case of its high affinity to oxygen and/or nitrogen. The substrate of the formed product is placed into the power fixture on a mobile platform, which moves relative to a stationary heat source with set speed  $V_s$  (Figure 1). The heat source is a component of a complex system of beam focusing and filler wire feeding. The electron beam is focused so that it had the form of a sharp cone that converges maximum close to the surface of the formed part. This allows realization of an effective and rather uniform melting of the filler wire without its significant overheating, as well as ensures concurrent heating of the deposition area for activation of the solid metal surface before its contact with the liquid filler material.

In order to manufacture products of guaranteed quality, it is necessary to optimize the technological parameters of the respective production processes.

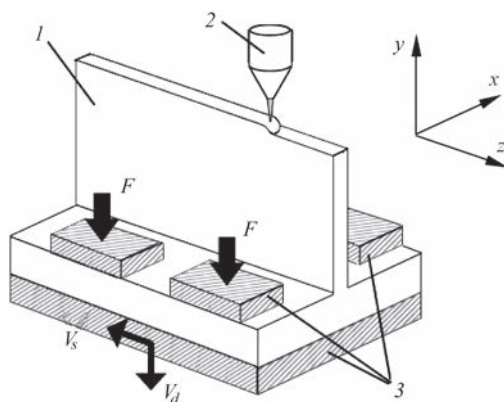


**Figure 1.** Scheme of formation of the web of a T-beam structure using xBeam 3D Metal Printer technology: 1 — product being formed; 2 — heat source; 3 — technological fixture

\*By materials of the paper presented at the International Conference «Beam Technologies in Welding and Materials Processing», September 9–13, 2019, Odessa (O.V. Makhnenko, N.S. Ananchenko, D.V. Kovalchuk also participated in the work).

In particular, it concerns ensuring fusion of the successive deposited layers, homogeneity of the metal structure, low level of residual strains and stresses. As conducting a broad range of experimental studies is associated with considerable economic expenses, it is rational to apply the mathematical and computer modeling of the processes determining the final quality of products.

As part of this study, a complex of approaches were developed for numerical prediction of the kinetics of temperature fields, phase and structural states, mechanical stresses and strains at layer-by-layer formation of typical beam structures of different size by xBeam 3D Metal Printer technology, in order to study the features of the impact of the technological parameters on the current and final state of the products.

**Development of the mathematical model of the kinetics of temperature and stress-strain state of typical structural elements at layer-by-layer formation of the sample.** Prediction of temperature field development is the first stage of numerical study of the kinetics of the product state during layer-by-layer formation. In its turn, nonuniform heating, change of the structural composition, as well as temperature dependencies of metal properties determine the spatial distribution of stresses and strains in the structure. Temperature distribution in time and space is determined by the processes of conductive propagation, for which the connection between moment of time  $t$  and temperature field  $T = T(x, y, z)$  is described by a three-dimensional equation of heat conductivity [5]:

$$\begin{aligned} c\rho(x, y, z, T) \frac{\partial T(x, y, z)}{\partial t} = \\ = \nabla [\lambda(x, y, z, T) \nabla T(x, y, z)], \end{aligned} \quad (1)$$

where  $\lambda$ ,  $c\rho$  are the heat conductivity and volumetric heat capacity of the structure material in this point as functions of spatial coordinates and temperature, respectively.

The heat source in the considered case is the electron beam of power  $q_i$ . It must be further noted that use of filler material means that part of the source energy is consumed in its melting, and heat application to the structure can proceed in two ways: directly from the source and by molten metal transfer onto the formed product. This can be taken into account by direct change of the structure profile, by adding sections, the temperature  $T_m$  of which is a little higher than liquidus temperature  $T_L$ , in order to allow for filler material overheating. Here, the value of effective heat input of the source must be reduced by the value of energy consumption for filler metal melting  $q_m$ . Thus, energy distribution in the heat spot can be

described by the normal distribution law, which has the following mathematical expression:

$$q(x, z) = \eta(q_i - q_m) \exp \left[ -\frac{(x - x_0)^2}{K_x} - \frac{(z - z_0)^2}{K_z} \right], \quad (2)$$

$$q_m = \int_{T_C}^{T_m} c\rho(T) v_m S_m dT + g_{fi} v_m S_m \rho(T_L),$$

where  $\eta$  is the efficiency of the heat source (thermal efficiency);  $x_0, z_0$  are the coordinates of the heat source center;  $K_x, K_z$  are the coefficients of concentration of energy flow in the respective directions;  $\rho$  is the density of structure metal, as a function of temperature;  $v_m$  is the filler material feed rate;  $S_m$  is the cross-sectional area of the wire;  $g_{fi}$  is the latent heat of melting of the filler material.

Boundary conditions required for solving problem (1), depend on the nature of heat removal from the product surface. So, in the area of contact with the technological fixture, the heat removal can be described by the Newton's law, whereas on the free surface it is characterized by thermal radiation (Stefan-Boltzmann law) with additional energy input from the surface of the product, being processed, when a heat source is placed there. Thus, boundary conditions for solving the heat conductivity problem in this case have the following mathematical expression:

$$\begin{aligned} -\lambda(T) \frac{\partial T}{\partial n} = \\ = \begin{cases} \alpha_{ht}(T - T_{en}), & \text{in the area of contact with the fixture} \\ \varepsilon \sigma_{SF}(T^4 - T_{en}^4) - q, & \text{on free surfaces} \end{cases}, \end{aligned} \quad (3)$$

where  $n$  is the normal to the surface;  $\alpha_{ht}$  is the heat transfer coefficient;  $T_{en}$  is the ambient temperature;  $\varepsilon$  is the degree of material blackness;  $\sigma_{SF}$  is the Stephan-Boltzmann constant;  $q$  is the energy flow of electron beam heating.

Proceeding from the results of prediction of the temperature field kinetics at layer-by-layer formation of typical products from VT6 titanium alloy, it is possible to predict the metal grain size and its certain properties in different parts of the structure, depending on the technological parameters of the process. It is known that refinement of the structural components of typical titanium-based alloys occurs with increase of the cooling rate at solidification. Figure 2 shows the dependence of grain size for VT6 alloy on the cooling rate [6], which can be approximated by the following equation:

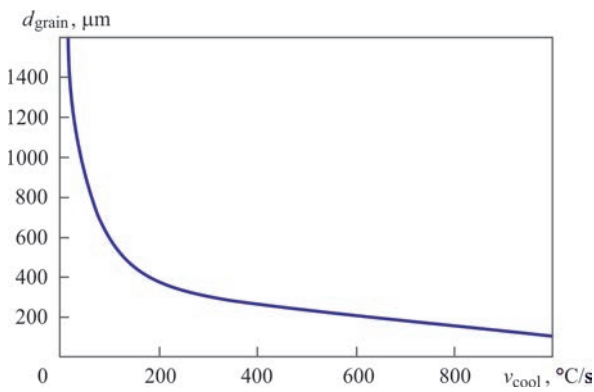


**Figure 2.** Dependence of grain size of VT6 titanium alloy on cooling rate [6]

$$d_{\text{grain}} = \begin{cases} 8220v_{\text{cool}}^{-0.58} \mu\text{m}, & \text{at } v_{\text{cool}} \geq 6 \text{ }^\circ\text{C/s} \\ 2500 \mu\text{m}, & \text{at } v_{\text{cool}} < 6 \text{ }^\circ\text{C/s} \end{cases}, \quad (4)$$

where  $d_{\text{grain}}$  is the characteristic size of the metal grain;  $v_{\text{cool}}$  is the cooling rate.

In addition, the actual mechanical characteristics of VT6 alloy depend on the cooling rate at phase transformation, that determines the residual percent ratio of  $\alpha$ -phase in  $(\alpha+\beta)$ -alloy. Figure 3 gives the diagrams of microstructural transformations of VT6 alloy at

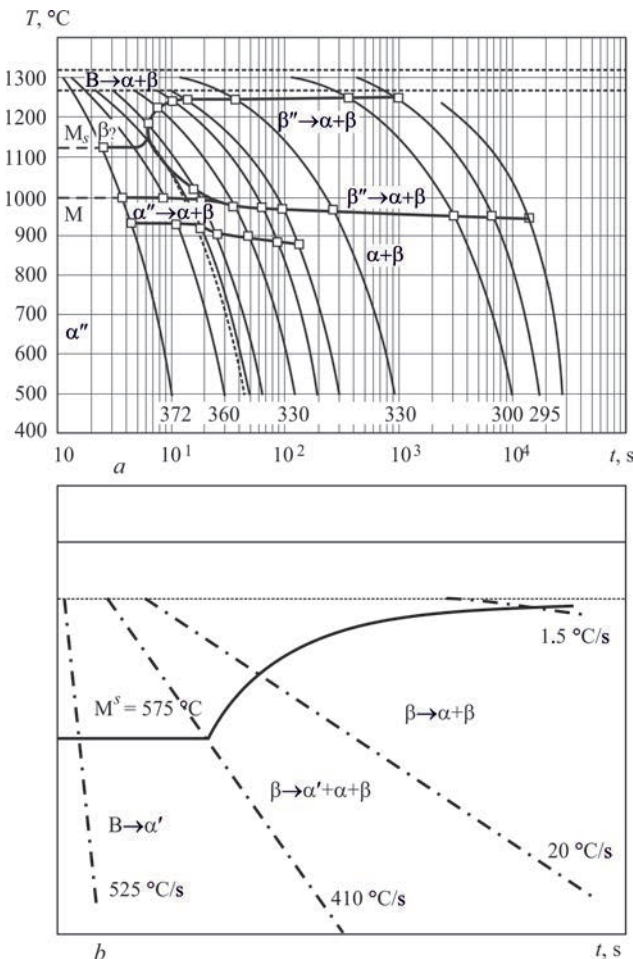


**Figure 3.** Diagrams of microstructural transformations of VT6 alloy at cooling: *a* — [7]; *b* — [8]

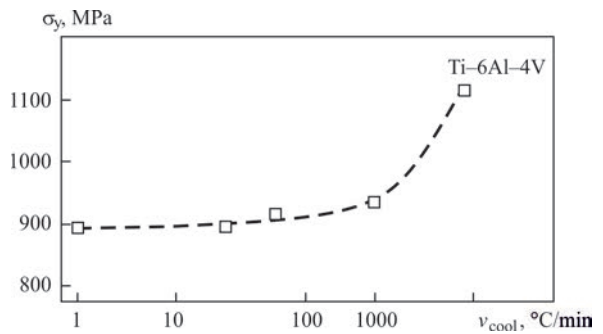


**Figure 4.** Dependence of yield limit of VT6 alloy on cooling rate [9]

cooling [7, 8], the cooling rate is determined in the range of  $\beta$  to  $(\alpha+\beta)$  microstructural transformations, which proceed in the range from 1000 to 670 °C. It should be noted that owing to low heat input and high speeds of heat source movement, layer-by-layer EBS is characterized by a rather high intensity of deposited material cooling that promotes formation of a martensitic microstructure containing  $\alpha'$ -phase. As one can see from Figure 4 [9], and at increase of the cooling rate and, accordingly, at reduction of the grain size the yield limit of VT6 alloy increases. Data in Figure 5 [8], which were derived on additive technology of layer-by-layer formation of samples by EBS method show that increase of the relative content of  $\alpha'$ -phase  $V_{\alpha'}$  causes a slight lowering of the yield limit of VT6 alloy, and relative elongation  $\delta$  here decreases fairly moderately (Figure 5, *b*). These dependencies can be approximated by the following equations:

$$\begin{aligned} \sigma_y &= 995 - 0.107v_{\text{cool}} - 18V_{\alpha'}, \text{ MPa}, \\ \delta &= -9V_{\alpha'} + 10.9, \%. \end{aligned} \quad (5)$$

Mathematical consideration of the united problem of temperature field kinetics and SSS development is based on finite element description with application of eight-node finite elements (FE). Within FE volume the distributions of temperatures, stresses and strains are taken to be uniform. Increment of strain tensor can be presented as superposition of the following components [10]:

$$d\epsilon_{ij} = d\epsilon_{ij}^e + d\epsilon_{ij}^p + \delta_{ij} d\epsilon_t, \quad (i, j = x, y, z), \quad (6)$$

where  $d\epsilon_{ij}^e$ ,  $d\epsilon_{ij}^p$ ,  $\delta_{ij}$ ,  $d\epsilon_t$  are the components of increment of the tensor of strains, due to elastic mechanism of deformation, instantaneous plasticity strains, and temperature expansion, respectively;  $\delta_{ij}$  is the Kronecker symbol.

Tensors of mechanical stresses  $\sigma_{ij}$  and elastic strains  $d\epsilon_{ij}^e$  are connected to each other by a generalized Hooke's law, i.e.

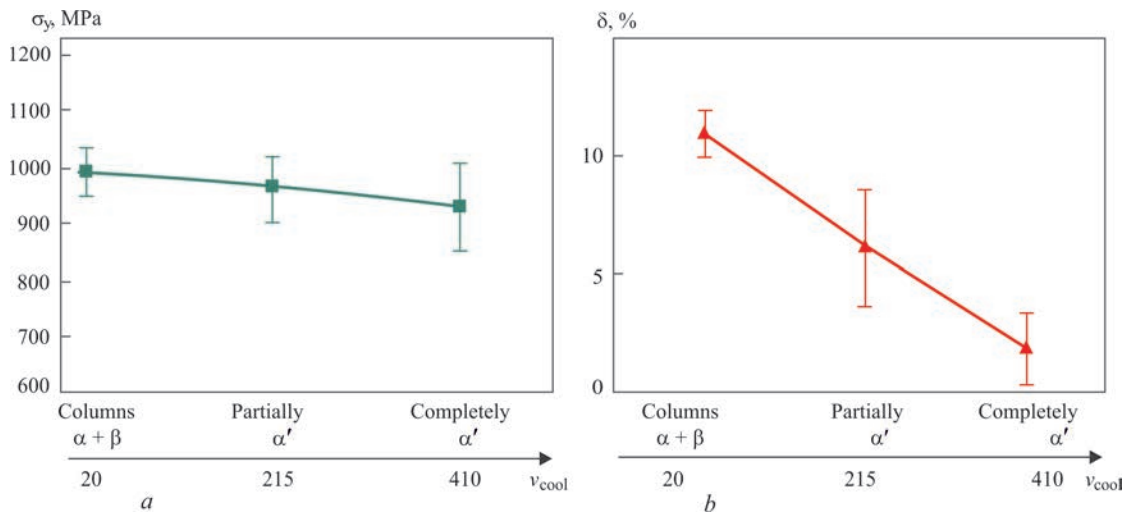


Figure 5. Dependence of yield limit (a) and relative elongation (b) of VT6 alloy on cooling rate and quantity of  $\alpha'$ -phase [8]

$$\varepsilon_{ij}^e = \frac{\sigma_{ij} - \delta_{ij} \sigma}{2G} + \delta_{ij} (K\sigma + \varphi), \quad (7)$$

where  $\sigma$  is the average value of the normal components of stress tensor  $\sigma_{ij}$ , i.e.  $\sigma = (\sigma_{xx} + \sigma_{yy} + \sigma_{zz})/3$ ;  $K = (1 - 2\nu)/E$  is the volumetric compression modulus;  $G$  is the shear modulus;  $E$  is the Young's modulus;  $\nu$  is the Poisson's ratio;  $\varphi$  are the volumetric strains.

Increment of instantaneous plasticity strain  $d\varepsilon_{ij}^p$  in a specific FE was calculated using a linear dependence of scalar function  $\Lambda$  and deviator component of the stress tensor, namely:

$$d\varepsilon_{ij}^p = d\Lambda(\sigma_{ij} - \delta_{ij} \sigma). \quad (8)$$

Specific value of function  $\Lambda$  depends on the stressed state in the considered area of the structure, as well as on the shape of the surface of material plastic flow  $\Phi$ , which is characterized by stresses  $\sigma_s$ :

$$\begin{aligned} d\Lambda &= 0, \text{ if } \sigma_i < \sigma_s, \\ d\Lambda &> 0, \text{ if } \sigma_i = \sigma_s, \\ \text{state } \sigma_i > \sigma_s &\text{ is inadmissible,} \end{aligned} \quad (9)$$

where  $\sigma_i$  is the stress intensity.

Proceeding from the above-said, the increments of strain tensor can be presented as superposition of increment of the respective components:

$$\begin{aligned} \Delta\varepsilon_{ij} &= \Psi(\sigma_{ij} - \delta_{ij} \sigma) + \delta_{ij} (K\sigma + \Delta\varepsilon_t) - \\ &- \frac{1}{2G}(\sigma_{ij} - \delta_{ij} \sigma)^* - (K\sigma)^*, \end{aligned} \quad (10)$$

where symbol «\*» refers the respective variable to the previous trace step;  $\Psi$  is the function of material state, which determines the plastic flow condition according to Mises criterion:

$$\begin{aligned} \Psi &= \frac{1}{2G}, \text{ if } \sigma_i < \sigma_s = \sigma_y, \\ \Psi &> \frac{1}{2G}, \text{ if } \sigma_i = \sigma_s, \text{ state } \sigma_i > \sigma_s \text{ is inadmissible.} \end{aligned} \quad (11)$$

Function  $\Psi$  is determined by iteration at each step of numerical tracking within the boundary problem of nonstationary thermoplasticity that allows solving the nonlinearity by plastic flow of the material. Proceeding from the specific value of function  $\Psi$  from (11), the strain filed is defined at each stage of loading, taking into account dependence  $\sigma_s(T, \varepsilon_p)$ :

$$\Delta\varepsilon_{ij} = \left( \xi - \frac{1}{2G} \right) (\sigma_{ij} - \delta_{ij} \sigma). \quad (12)$$

Here, at each stage of iteration by  $\Psi$ , stress  $\sigma_{ij}$  is calculated by the following algorithm (repeated indices are summed up):

$$\sigma_{ij} = \frac{1}{\Psi} \left( \Delta\varepsilon_{ij} + \delta_{ij} \frac{\Psi - K}{K} \Delta\varepsilon \right) + J_{ij}, \quad (13)$$

where

$$\Delta\varepsilon = \frac{\Delta\varepsilon_{ii}}{3},$$

$$J_{ij} = \frac{1}{\Psi} \left[ (b_{ij} - \delta_{ij} b) + \delta_{ij} \left( K\sigma^* - \frac{\Delta\varepsilon_t}{K} \right) \right], \quad (14)$$

$$b_{ij} = \left( \frac{\sigma_{ij}}{2G} \right)^* + \delta_{ij} \left[ \sigma_m^* \left( K - \frac{1}{2G} \right)^* - \Delta\varphi \right], b = \frac{b_{ij}}{3}.$$

Stress tensor components satisfy the statics equations for internal FE and boundary conditions for the surface ones. In their turn, the components of displacement vector  $\Delta U_i = (\Delta U, \Delta V, \Delta W)$  satisfy the respective conditions on the boundary. The solved system of equations in variables of the vector of dis-

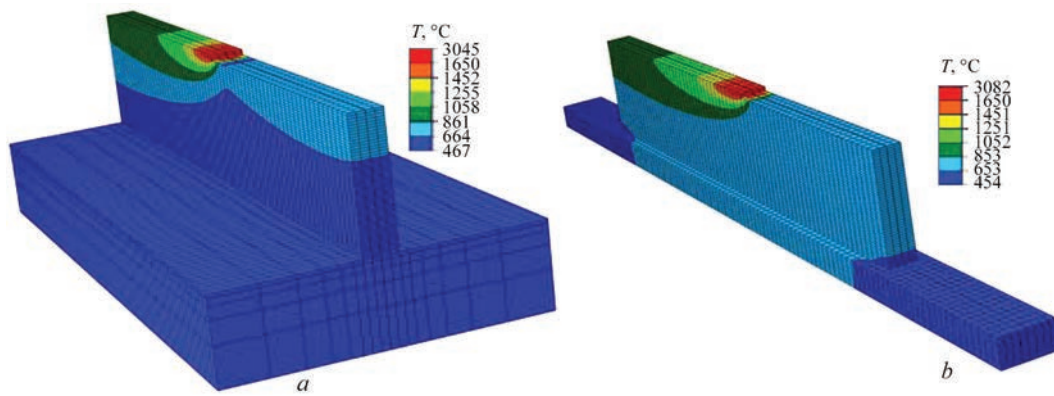


**Figure 6.** Comparative distribution of temperatures in a T-shaped sample with large (a) and small (b) substrates during layer-by-layer formation of the part

placement increments in FE nodes at each trace step and iteration by  $\psi$  is determined by minimizing the following functional (Lagrange variational principle):

$$\Theta_l = -\frac{1}{2} \sum_V (\sigma_{ij} + J_{ij}) \Delta \epsilon_{ij} V_{m,n,r} + \sum_{S_p} P_i \Delta U_i \Delta S_P^{m,n,r}, \quad (15)$$

where  $\sum_V$  is the sum operator for internal FE;  $\sum_{S_p}$  is the sum operator for surface FE, on which the components of force vector  $P_i$  are assigned, i.e. the following system of equations yields a solution in the components of the vector of displacement increments at each trace step and iterations by  $\psi$  for a specific FE:

$$\frac{\partial E_l}{\partial \Delta U_{m,n,r}} = 0, \quad \frac{\partial E_l}{\partial \Delta V_{m,n,r}} = 0, \quad \frac{\partial E_l}{\partial \Delta W_{m,n,r}} = 0. \quad (16)$$

**Results of modeling the temperature fields at layer-by layer formation of the tee sample and prediction of the material structure and mechanical properties.** Features of temperature field kinetics were studied on the typical example of layer-by-layer formation of a T-shaped beam product. The following process parameters are recommended: filler material – 1.6 mm titanium rod, electron beam power of 4.5 kW, filler wire feed rate of 14 mm/s, substrate movement speed of 14 mm/s. In order to determine the impact of geometrical features of the product, EBS on substrates of different thickness was considered, namely on massive substrate of 8×30×70 mm size; and on small one of 3×6×110 mm size. Results of solving the nonstationary heat conductivity problem showed that the kinetics of the temperature field at layer-by-layer formation of the tee sample on a massive substrate is of essentially 3D nature whereas in the case of a small substrate, sample heating by volume is more uniform (see Figure 6) that is attributable to the effect of heat accumulation.

As shown by analysis of thermal cycles (Figure 7), in the range of microstructural transformations from

1000 to 670 °C, the material is heated and cooled 3 times: first during deposition of the layer, then during deposition of the next two layers. The last cooling cycle in the above-mentioned temperature range determines the residual microstructure and grain size. Maximum heating temperature in the considered region from deposition of the next third and more distant layers is below the temperature of 1000 °C, so that no microstructural transformations or considerable change of grain size occur. Moreover, this process is characterized by rather high cooling rates (160–660 °C/s), so that in keeping with the diagrams of microstructural transformations of VT6 alloy (see Figure 2) the deposited metal of tee sample is predicted to have a martensitic microstructure, containing  $\alpha'$ -phase. By the data of calculations in the material of the first layer, where the highest cooling rate was achieved, owing to the presence of a massive cold substrate, 180  $\mu\text{m}$  grain forms, and in the points of formation of 5 and 20 layers, where material is deposited on the already heated sample, grain size is much larger and reaches 300–450  $\mu\text{m}$ .

These results comply with the available experimental data [4] on the microstructure of a sample of VT6 titanium alloy, produced by xBeam 3D Metal Printer technology of layer-by-layer formation: grain size in the upper layers of the sample is equal to approximately 300–450  $\mu\text{m}$ , and in the layers near the sample base it is 150–250  $\mu\text{m}$  (Figure 8). Thus, pre-

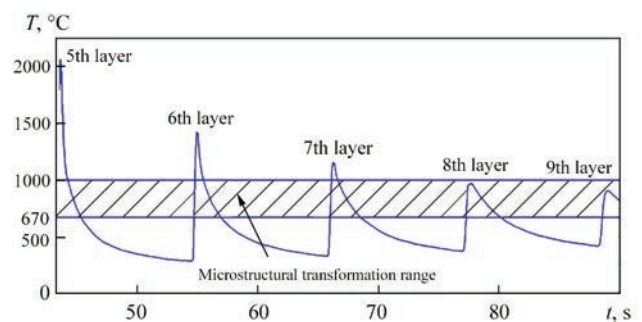


**Figure 7.** Characteristic thermocycle in T-shaped sample material (5th layer) at multilayer formation

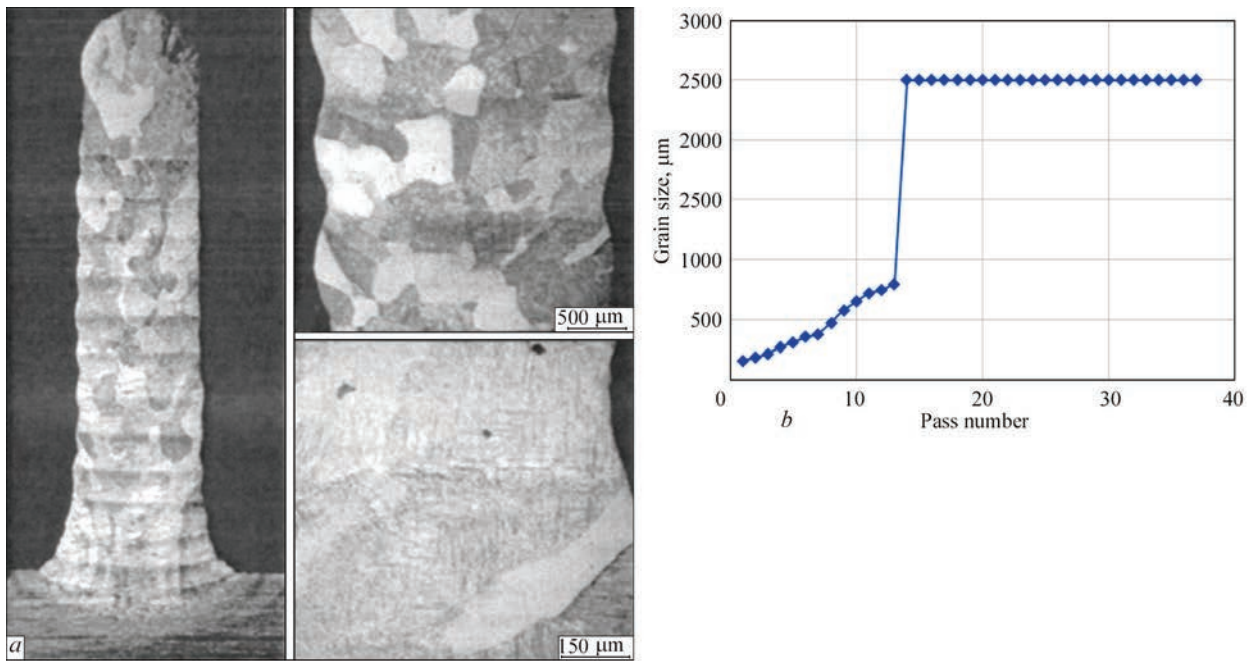


**Figure 8.** Macrostructure of a tee sample from VT6 titanium alloy: *a* — experimental study [11]; *b* — calculation results

diction results showed satisfactory accuracy, compared with the experiment that allows application of the developed mathematical model for prediction of the macrostructure and mechanical properties of the metal of structures produced by such technologies.

As was shown by the authors in previous works, one of the effective ways to optimize the temperature fields at layer-by-layer formation of typical beam structures is application of delay time  $\Delta t$  of deposition of each of the beads, variable by product height

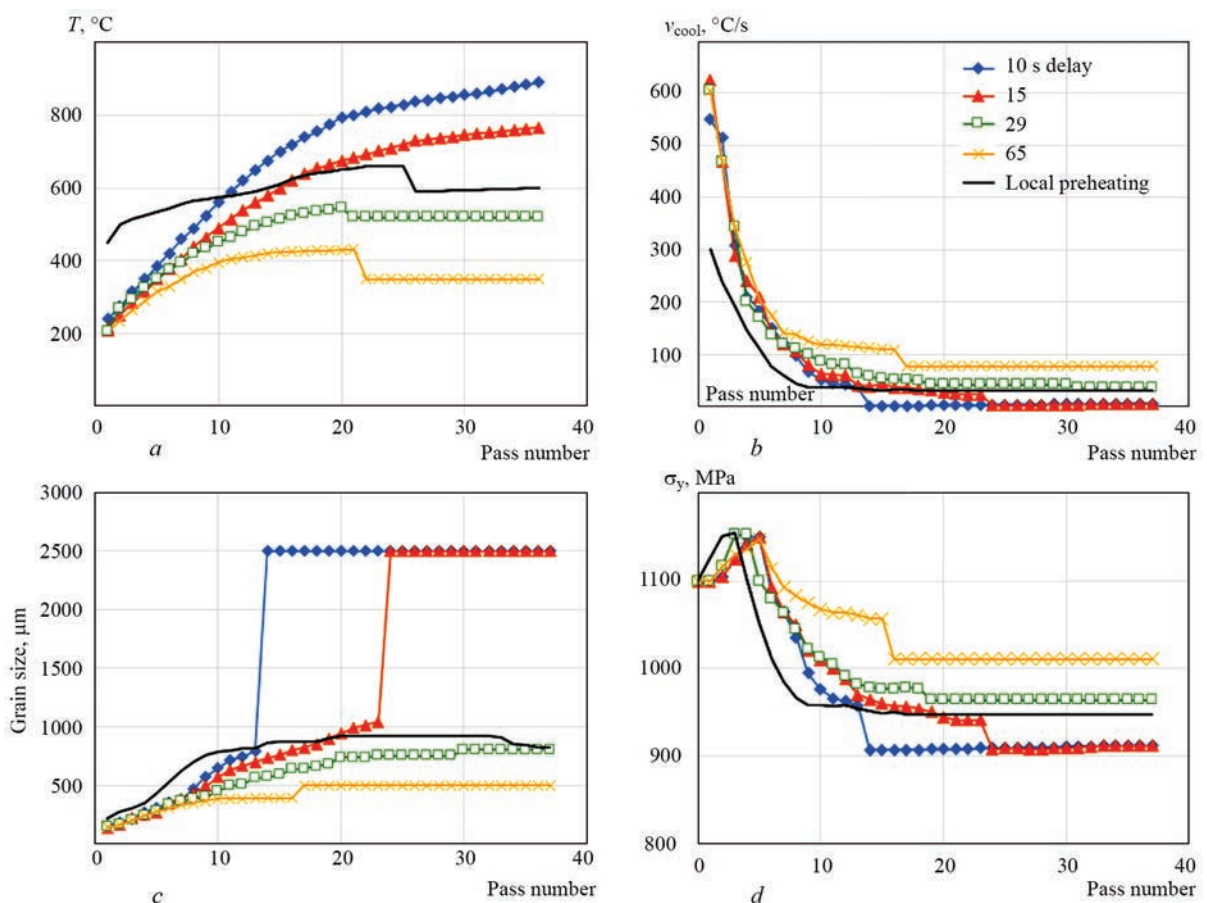


**Figure 9.** Dependence of temperature in the point before deposition of the next layer (*a*), cooling rate (*b*), grain size (*c*) and material yield limit (*d*) on pass number for different delay times between the passes

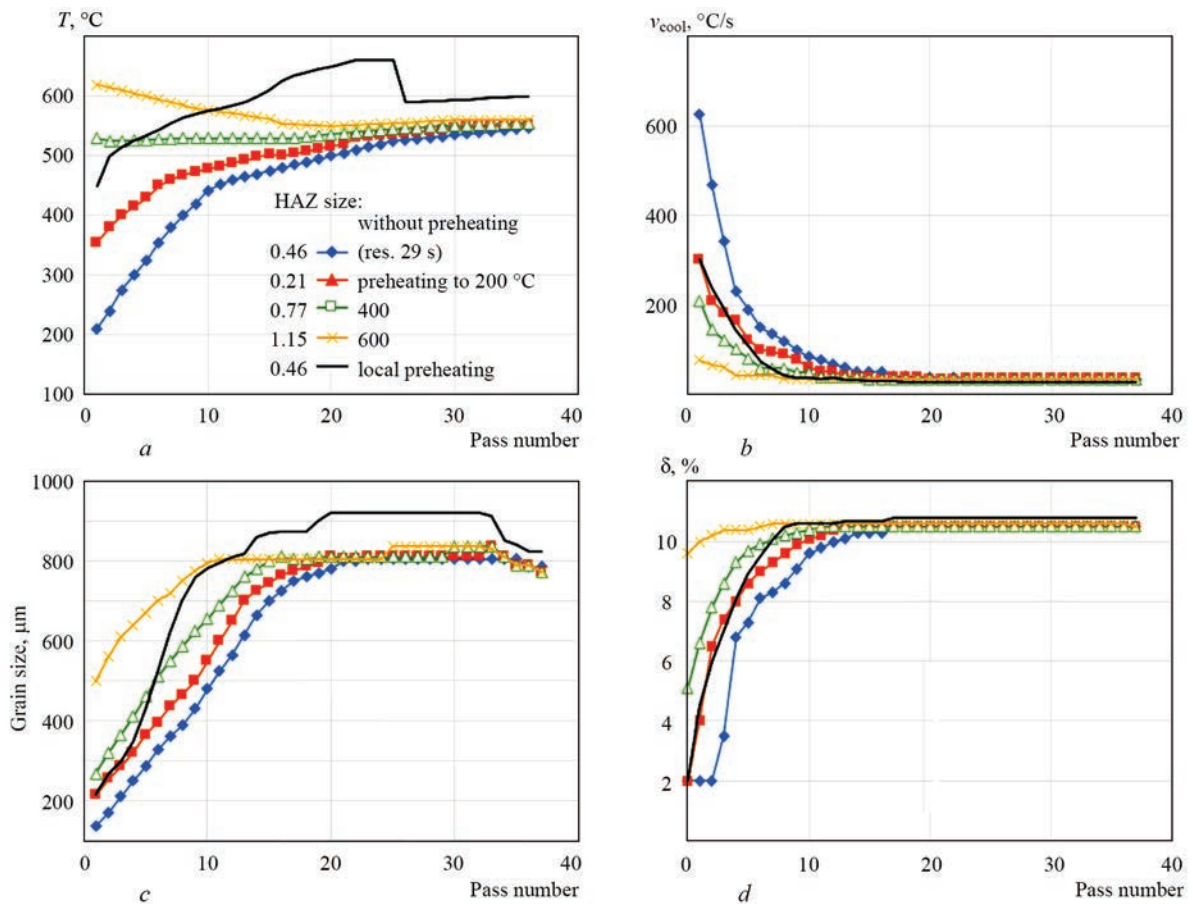


**Figure 10.** Dependence of temperature in a point before deposition of the next layer (a), cooling rate (b), grain size (c) and relative elongation (d) on pass number for different preheating of the substrate

[11]. This allows ensuring the natural dissipation of excess heat, which accumulates as the product layers are deposited, and avoid its overheating without the need for variation of the power (speed) of the heat source. This technological parameter essentially affects the cooling rate, grain size, and, consequently, the product material yield limit (Figure 9, a–c). One can see from the given data that the best strength characteristics and more uniform material structure were determined in the sample, made with longer time  $\Delta t$ ,

whereas the insufficient time between bead deposition  $\Delta t = 10$  s and 15 s results in insufficient strength characteristics of metal in the upper layers, and grain non-uniformity by height. On the other hand, too long time between the passes (65 s) leads to formation of an excess of  $\alpha'$ -phase, and reduction of material plasticity. Substrate preheating allows obtaining a more uniform structure in the lower layers, and essentially improves the material plasticity (Figure 10, a–c). For the time between bead deposition  $\Delta t = 10$  s and 15 s the grain size increases significantly, starting from the number of the bead, on which the interpass temperature exceeds  $670^\circ\text{C}$ : then the grain is finally formed after complete cooling of the sample, and the cooling rate here is low. When the time between beads deposition is  $\Delta t = 29$  s, the interpass temperature does not exceed  $670^\circ\text{C}$ , so that the produced grain is more uniform.

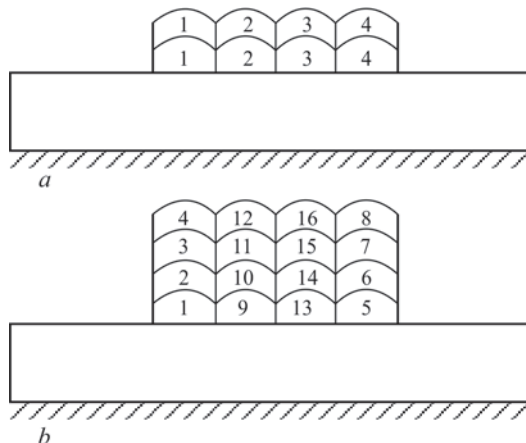


**Figure 11.** Characteristic sequences of bead deposition at formation of T-shaped beam structure: a — layer-by-layer deposition (scheme A); b — column deposition (scheme B)

**Characteristic features of residual stress-strain state at layer-by-layer formation of thick-walled T-shaped products by xBeam 3D Metal Printer technology.** In the previous works the authors studied the features of the kinetics of stress-strain state (SSS) during layer-by-layer formation of beam, cylindrical and spherical structural elements, using xBeam 3D Metal Printer technology [11]. In particular, it was em-

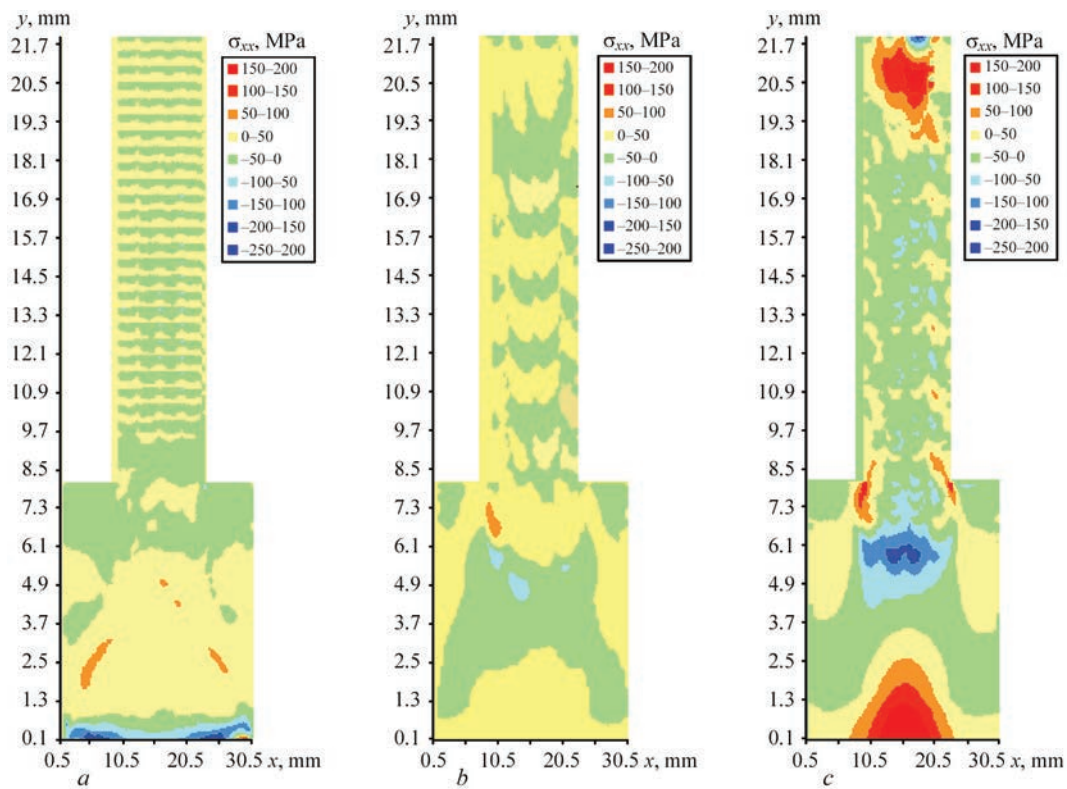


**Figure 12.** Distribution of residual stresses,  $\sigma_{xx}$  (MPa) in the cross-section of a T-shaped product: *a* — scheme A with optimization; *b* — scheme B with optimization; *c* — scheme B without optimization (see Figure 11)

phasized that one of the advantages of this technology is the possibility of deposition of rather narrow beads of liquid metal and production of thin-walled structural elements (with 2–3 mm wall thickness) with small

geometrical tolerances. However, xBeam 3D Metal Printer applicability is not limited to just thin-walled products: various sequences of forming bead deposition can be used, if it is necessary to manufacture

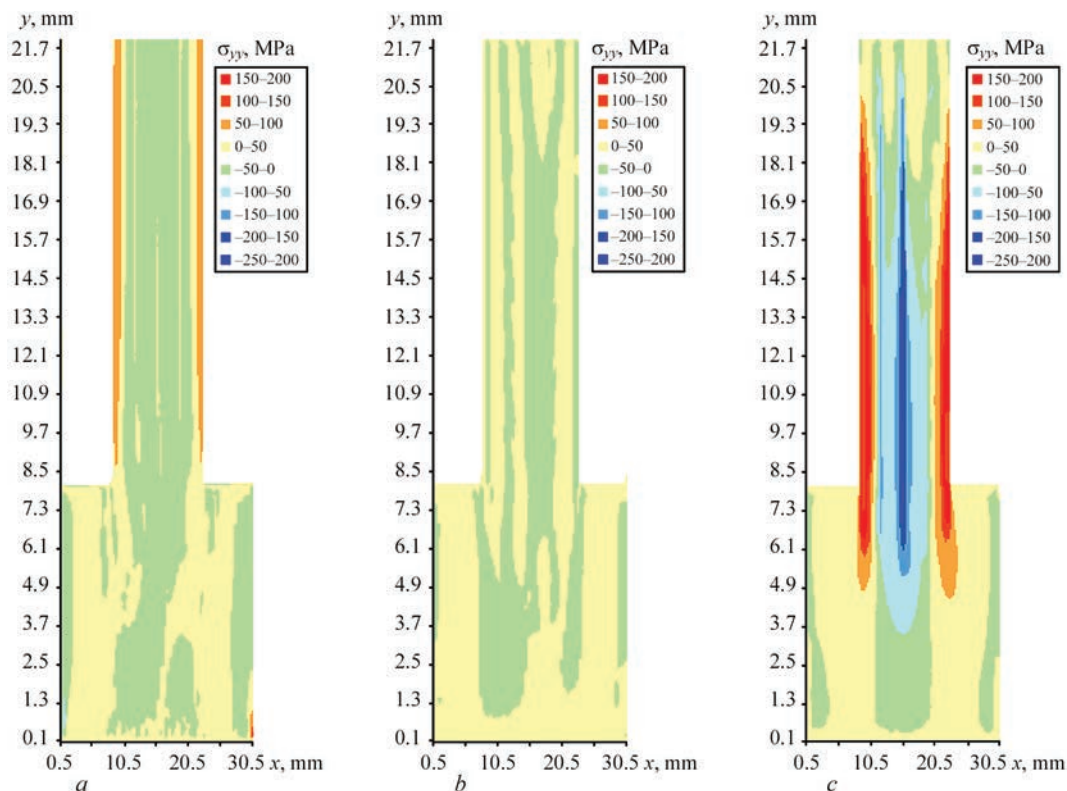


**Figure 13.** Distribution of residual stresses  $\sigma_{yy}$  (MPa) in the cross-section of a T-shaped product: *a* — scheme A with optimization; *b* — scheme B with optimization; *c* — scheme B without optimization (see Figure 11)

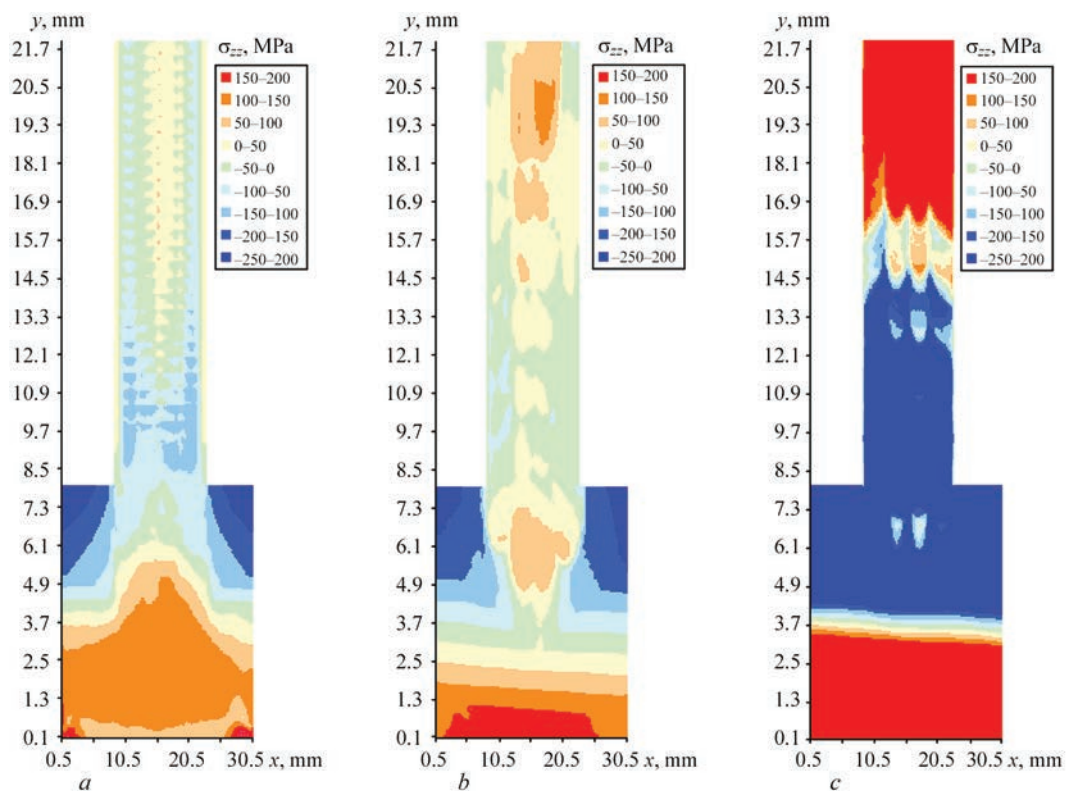


**Figure 14.** Distribution of residual stresses  $\sigma_{zz}$  (MPa) in the cross-section of a T-shaped product: *a* — scheme A with optimization; *b* — scheme B with optimization; *c* — scheme B without optimization (see Figure 11)

thick-walled parts. These sequences allow producing structures with different wall thickness without any essential change of the respective technological parameters. However, such a process certainly requires optimization, in particular, from the viewpoint of rational selection of the time of the start of each bead formation (delay time  $\Delta t$ ) and formation of favourable residual SSS.

Within the scope of this work, the features of residual SSS depending on the technological conditions of production were studied in the case of a thick-walled T-shaped beam. Considered were two typical sequences of deposition of a tee wall of 12.8 mm thickness, which consists of four parallel beads 3.2 mm thick and 0.8 mm high (Figure 11). Structure material was VT6 titanium alloy. The principal difference between these schemes consists in that for sequence A the web is formed by successive horizontal layers, whereas for sequence B vertical columns are the forming elements.

Figures 12–14 show the results of prediction of the residual stress fields in the cross-section of a thick-walled beam for sequences A and B, taking into account optimization of the temperature fields by selection of optimum delay time  $\Delta t$ , as well as deposition by sequence B without such optimization. As one can see from the given results, the temperature field optimization allows achieving structure heating sufficiently uniform by thickness, despite the different sequence

of bead deposition. Thus, the conditions for uniform cooling of the product, and, accordingly, low level of residual stresses, are in place. A natural stress raiser in such a case is the region of transition of the tee section flange into the web, where the uniform cooling conditions are not fulfilled for the reason of massiveness of the substrate (tee section flange). If the conditions of the temperature field optimization are not fulfilled, and the structure is nonuniformly heated, it leads to formation of high stresses, particularly, in the longitudinal direction (see Figure 14, *c*). Therefore, a rational selection of the delay time between the deposited beads is important not only in terms of guaranteeing the conditions, favourable for sound formation of the product, but also for lowering the residual stresses, that is required for high performance of the produced structural elements.

## Conclusions

1. A complex of mathematical models was developed for numerical prediction of the temperature field kinetics, phase and structural states, mechanical stresses and strains at layer-by-layer formation of typical beam structures from VT6 titanium alloy, using xBeam 3D Metal Printer technology. Comparison with the data of experimental studies showed the satisfactory accuracy of the obtained calculation results of prediction of the macrostructure and mechanical properties of the structure metal.

2. The impact of substrate dimensions on temperature field kinetics during layer-by-layer deposition of a web of a tee section was studied. It is shown that in case of a massive substrate 8 mm thick temperature distribution is of an essentially 3D nature, whereas for the case of a small substrate of 3 mm thickness, more uniform heating of the sample by volume is in place, that is attributable to heat accumulation effect.

3. It is shown that better strength characteristics and more uniform structure of the material of the part, produced by layer-by-layer formation, can be achieved at maximum increase of the delay time between beads deposition, whereas insufficient time results in lower strength characteristics of metal in the upper layers, and nonuniformity of the grain by height. However, increase of time between the passes may lead to formation of an excess of  $\alpha'$ -phase, and lowering of material plasticity. An effective means for producing a more uniform structure and improvement of material plasticity is preheating of the plate before the beginning of structure fabrication.

4. A characteristic example of layer-by-layer formation of T-shaped beam structure was used to study the regularities of the residual stressed state in fabrication of thin-walled structures. It is proved that optimization of delay time at deposition of each of the beads is an important factor, allowing achievement of a low level of residual stresses. Here, conditions are in place for uniform cooling of the structure (except for the region of transition of the tee flange into the web) and an essential lowering of residual stresses. Violation of the optimal thermal mode can lead to an essential increase of residual stresses (particularly, longitudinal), creating a negative effect on such a structure performance.

1. Edwards, P. et al. (2013). Electron beam additive manufacturing of titanium components: Properties and performance. *J. of Manufacturing Sci. and Eng.*, 135(6). DOI: 061016/1-061016/7.
2. Juechter, V., Franke, M.M., Merenda, T. et al. (2018) Additive manufacturing of Ti-45Al-4Nb-C by selective electron beam melting for automotive applications. *Additive Manufacturing*, 22, 118–126. DOI: 10.1016/j.addma.2018.05.008.
3. Dutta, B., Froes, F.H. (2016) *Additive manufacturing of titanium alloys: State of the art, challenges and opportunities*. Oxford, Butterworth-Heinemann. DOI: 10.1016/C2015-0-02470-4.
4. Kovalchuk, D.V., Melnik, V.I., Melnik, I.V. (2017) New possibilities of additive manufacturing with xBeam 3D Metal Printing technology. In: *Proc. of 8th Int. Conf. on Beam Technologies in Welding and Processing of Materials*. Kyiv, 45–52.
5. Makhnenko, V.I. (2006) *Safe service life of welded joints and assemblies of modern structures*. Kyiv, Naukova Dumka [in Russian].
6. Polkin, I.S. (2006) Improvement of properties of metallic materials due to application of new technological processes. In: *Advanced technologies of light and special alloys*. Moscow, Fizmatlit, 66–73 [in Russian].
7. Sieniawski, J., Ziaja, W., Kubiak, K. (2013) Microstructure and mechanical properties of high strength two-phase titanium alloys. *Titanium Alloys*, 69–79.
8. Liu, S., Shin, Y.C. (2019) Additive manufacturing of Ti6Al4V alloy: A review. *Materials and design*, 164, 1–23.
9. Patil, S., Kekade, S., Phapale, K. (2016) Effect of  $\alpha$  and  $\beta$  phase volume fraction on machining characteristics of titanium alloy Ti6Al4V. In: *Proc. of 16th Machining Innovations Conf. for Aerospace Industry*, 65.
10. Velikoivanenko, E.A., Milenin, A.S., Popov, A.V. et al. (2019) Methods of numerical forecasting of the working performance of welded structures on computers of hybrid architecture. *Cybernetics and Systems Analysis*, 55(1), 117–127. DOI: 10.1007/s10559-019-00117-8.
11. Makhnenko, O.V., Milenin, A.S., Velikoivanenko, E.A. et al. (2017) Modelling of temperature fields and stress-strain state of small 3D sample in its layer-by-layer forming. *The Paton Welding J.*, 3, 7–14. DOI: 10.15407/tpwj2017.03.02.

Received 21.11.2019

## CUTTING WORLD 2020

### THE TRADE FAIR FOR PROFESSIONAL CUTTING TECHNOLOGY



From April 28 to 30, 2020, Cutting World will be open at Messe Essen. It is the only trade fair to concentrate on the entire process chain on the subject of cutting. Numerous exhibitors have already taken the opportunity to secure booth areas in the new Hall 8 for themselves. Since recently, these have also included the following companies: Assfalg, Boschert, Cam Concept, Eckelmann, Kjellberg, MGM, ProCom and Rosenberger. Air Liquide Deutschland, BKE, IHT Automation, NUM, STM Waterjet and Yamazaki Mazak Deutschland had previously confirmed their participation. Any interested exhibitors can find the registration documents at [www.cuttingworld.de](http://www.cuttingworld.de). The registration deadline will be November 30, 2019.

# IMPACT OF SPATIAL POSITION IN LASER WELDING ON QUALITY LEVEL OF WELDED JOINTS OF AISI 321 STEEL

A.V. Bernatskii, V.D. Shelyagin, O.V. Siora, V.M. Sydorets and O.M. Berdnikova

E.O. Paton Electric Welding Institute of the NAS of Ukraine

11 Kazymyr Malevych Str., 03150, Kyiv, Ukraine. E-mail: [office@paton.kiev.ua](mailto:office@paton.kiev.ua)

The objective of the study was determination of the impact of spatial position in laser welding of corrosion- heat-resistant austenitic steel AISI 321 on the microstructure and quality level of welded joints. Penetration beads were made in plates of 3 mm thickness at different angles of inclination to the horizontal plane. «Uphill» and «downhill» laser welding was performed both in the continuous and pulsed modes of laser generation. Results of visual and radiographic testing and analysis of the data of metallographic examinations were used for evaluation of quality level of the produced specimens for compliance with the requirements of valid standards. In «uphill» and «downhill» welding in the continuous mode of laser generation no inner defects in the form of cracks, pores and inclusions were found at all the angles of inclination. A tendency to increase in both the quantity as well as in the size of pores at reduction of the angle of inclination from 90 to 0° was found in «downhill» and «uphill» welding in the pulsed mode of laser generation. By the data of metallographic examinations, no significant differences were observed in the structure of welded joints made in different spatial positions on steel AISI 321 of 3 mm thickness. At different values of the angle of inclination, the microhardness and dimensions of the crystallites differ by approximately 10 %. Contrarily, the shape of welds in the produced penetration beads differs quite significantly. Dependencies of quality characteristics of welded joints of AISI 321 steel in laser welding were derived for the first time for different spatial positions. The derived dependencies provide determination of tendencies of changing the shape and quality of welded joints at the change of position or technological parameters of laser welding process. 13 Ref., 2 Tables, 6 Figures.

*Key words:* laser welding; corrosion-resistant steel; heat-resistant steel; austenitic steel; technological parameters; spatial position; quality; structure; porosity

## Analysis of recent investigations and publications and problem statement.

The assortment of products for the power engineering, aerospace, chemical, food and other industries includes parts of both small and large sizes of corrosion- heat-resistant steels [1–3]. Their design often has a complex spatial shape with curvilinear surface profiles. Therefore, a need arises to produce different types of welded joints of such structures in different spatial positions [4–6]. In such circumstances, it is necessary not only to take into account the physical effects, accompanying welding, but also to try to use them for the benefit. For example, considering the forces of gravity and surface tension, it is possible to influence the degree of opening of the penetration channel when moving the weld pool in different directions [7]. The global trends demonstrate the ever increasing use of laser welding technologies for the manufacture of such structures [8–10]. By means of scanning, regulation of speed of movement and pulse control of laser radiation power, it is possible to impact the heat input into the treatment zone and the stability of formation of the penetration channel and the degree of absorption of radiation in

the near-surface plasma [7, 11–13]. Thus, the problem arises of taking into account the abovementioned features, which should allow obtaining a set of necessary indicators of the process of laser welding in different spatial positions.

The lack of knowledge about the dependence of weld shape and the characteristics of welded joints on spatial position does not allow determining the technological parameters of laser welding, which are the most rational in terms of achieving a high quality and compliance with the requirements of valid standards.

The objective of the study was determination of the impact of spatial position in laser welding of corrosion- heat-resistant austenitic steel AISI 321 on the quality level and structure of welded joints.

**Methods, object and subject of investigations.** The object of investigations was the process of laser welding of AISI 321 steel in different spatial positions.

The subject of investigations is the impact of spatial position in laser welding of AISI 321 steel on the quality and structure of welded joints.

The quality level of welded joints was determined by DSTU EN ISO 13919-1:2015 «Welding. Elec-

tron and laser beam welded joints — Requirements and recommendations on quality levels for imperfections — Part 1: Steel», according to which three levels of quality were established, which correspond to a certain range of maximum permissible sizes of defects and relate to welded joints.

The material of investigations were plates with the size of 300×100×3 mm made of corrosion-heat-resistant austenitic steel AISI 321 (analogue of 12Kh18N10T) with a tensile strength  $\sigma_t = 520\text{--}560$  MPa and the following chemical composition, wt. %: up to 0.12 % C; up to 0.8 % Si; 1–2 % Mn; 10–11 % Ni; up to 0.2 % S; up to 0.035 % P; 17–19 % Cr; up to 0.6 % Ti; Fe is the remnant).

According to the experimental procedure, investigations of laser welding in different spatial positions were performed by using the laboratory bench (Figure 1), which was assembled on the base of ND: YAG-laser DY044 of the ROFIN-SINAR Company (Germany).

According to the scheme, shown in Figure 2, in the plates of AISI 321 steel the penetrations were made at different angles of inclination  $\alpha$  to the horizontal plane of the mechanism of moving the laser head and the clamp with a specimen, namely: in the flat position; in the vertical position; at angles of 60; 45 and 30°. In all the variants (except of flat position), welding was carried out in «uphill» (Figure 2, *a*) and «downhill» (Figure 2, *b*) directions. Welding was performed in continuous and pulsed modes of laser generation at preliminary selected welding modes. The angle of incidence of laser radiation  $l$  on the plate 2 (Figure 2) remained unchanged at different spatial positions and amounted to 90°.

According to the results of visual, radiographic testing and metallographic examinations of the produced specimens, their quality level was evaluated for compliance with the requirements of the standard DSTU EN ISO 13919-1:2015.

**Technological experiment and its results.** In the continuous mode of laser generation, the technological parameters of welding process were as follows: power of laser radiation was 4.4 kW; welding speed was 100 mm/s, deepening of position of the focal plane of the lens relative to the surface of welded specimens was 1 mm; flow rate of shielding gas (argon) was 500 cm<sup>3</sup>/s.

In the pulsed mode of laser generation, the technological parameters of welding process were as follows: maximum power of laser radiation was 4.4 kW, ratio of pulse duration and a pause (duty cycle) was 1.67; pulse repetition rate was 120 Hz; other parameters were similar to welding modes at the continuous laser generation.



**Figure 1.** Laboratory bench for laser welding in different spatial positions

According to the results of visual inspection of the made penetrations in the specimens of AISI 321 steel, the following was established:

- depending on the direction of movement, significant differences in appearance of the weld surface are observed, namely, in «downhill» welding during weld formation the annealing colours were not recorded, and during «uphill» welding the annealing colours were observed on the joint surface;
- splashes were fixed during the use of continuous and pulsed mode in all spatial positions, their number was minimal during penetration in the flat position, it increased slightly at an angle of inclination of 60° and in the vertical position, and the highest number of splashes was observed in laser welding at the angles of inclination of 30 and 45°;
- during «uphill» welding in a continuous mode of laser generation at all the angles of inclination, the upper bead of welded joint is formed with a slight depression and with the formation of a «comb», the height of the «comb» and the value of depression grows with the increase in the angle of inclination to the horizontal plane;
- during «downhill» welding in a continuous mode of laser generation, the upper bead of welded joint is

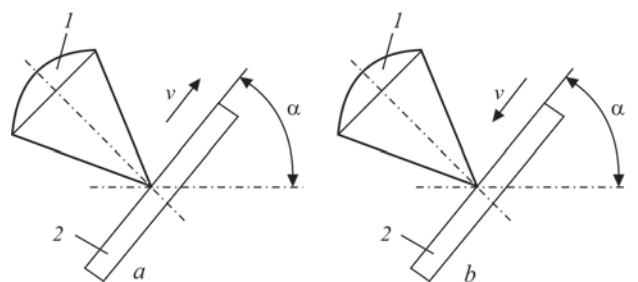


**Figure 2.** Schemes of making penetrations in plates during laser welding in «uphill» (*a*) and «downhill» (*b*) directions:  $l$  — laser radiation focused by the lens; 2 — plate;  $\alpha$  — angle of inclination of plate to the horizontal plane

**Table 1.** Inner defects in the form of single pores or chain pores found during «uphill» and «downhill» welding in the pulsed mode of laser radiation

| Welding direction | Angle of inclination $\alpha, ^\circ$ | Quantity of single pores | Chain pores/ their total length, mm | Maximum size of pores, mm |
|-------------------|---------------------------------------|--------------------------|-------------------------------------|---------------------------|
| Downhill          | 30                                    | –                        | *                                   | 0.4                       |
|                   | 45                                    | 1                        | –                                   | 0.3                       |
|                   | 60                                    | 7                        | –                                   | 0.5                       |
|                   | 90                                    | –                        | 2/25                                | 0.5                       |
| Uphill            | 30                                    | –                        | *                                   | 0.3                       |
|                   | 45                                    | –                        | –                                   | –                         |
|                   | 60                                    | –                        | 2/8                                 | 0.3                       |
|                   | 90                                    | 3                        | –                                   | 0.3                       |
| Flat position     | 0                                     | –                        | *                                   | 0.5                       |

\*Along the whole length of the weld.

formed with a slight depression and with a «comb» formation only at an angle of inclination of 30°.

According to the results of radiographic testing of the made penetrations, it was found that during «uphill» and «downhill» welding in a continuous mode of laser generation, at all the angles of inclination, no inner defects in the form of cracks, pores and nonmetallic inclusions were found.

Radiographic testing of penetrations, made during «uphill» and «downhill» welding in the mode of a pulsed laser generation showed the presence of inner defects in the form of single pores or chain pores at all the angles of inclination (Table 1).

In Figure 3 the macrostructure of welded joint produced in the flat spatial position during continuous laser generation is given, the microstructure of metal in the centre and on the fusion line.

The structure of weld metal in the welded joint, produced in the flat position, is dispersed and cast. In Figure 3 two zones are clearly seen: in the central part of the weld, throughout the entire height the structure is cellular-dendritic, in the middle part of the weld closer to the fusion line, a region of thin columnar crystallites is observed growing in the direction of heat removal. The zones are separated by a strip of more refined crystallites. The microstructure in the central part of the weld represents an austenitic matrix

with a small amount of  $\delta$ -ferrite (1.5–1.7 %). The size of cells is generally 12–13  $\mu\text{m}$ . The hardness of weld metal of the welded joint in the central part is  $HV1$ –2950–3090 MPa, there are areas where the hardness increases to  $HV1$ –3200–3380 MPa. In the lower part of the weld, the hardness increases to  $HV1$ –3320–3650 MPa. On the fusion line of the welded joint, the microstructure also contains austenite and  $\delta$ -ferrite, it is more refined than in the center of the weld. The width of crystallites is 2–9  $\mu\text{m}$ . The hardness of the metal on the fusion line of the welded joint is  $HV1$ –2990–3030 MPa. There are separate areas where the hardness increases to  $HV1$ –3160 MPa. In the weld metal nitrides (in a small quantity) and single slag inclusions are observed. The heat-affected-zone (HAZ) is not distinct, its structure contains austenite, the grain size number in the HAZ of welded joint is No.6. The hardness of the HAZ of welded joint is  $HV1$ –2650–2840 MPa.

As metallographic examinations showed, there are no significant differences in the structure of welded joints produced at different spatial positions in AISI 321 steel of 3 mm thickness. At different angle of inclination, the values of microhardness in the respective zones, sizes of crystallites, grain size number in the HAZ of welded joint differ by about 10 %. Contrarily, the shape of the resulting penetrations changes quite substantially, as is seen from Table 2.

**Discussion of the obtained results.** The analysis of X-ray patterns (Figure 4) shows a tendency to increase both the quantity as well as the size of pores in the specimens of AISI 321 steel at the reduction of angle of inclination from 90 to 0° during «downhill» and «uphill» welding in the pulsed mode of laser generation. The small values of a total pores projection during welding with the use of a continuous laser radiation and at the angles of 0 and 90° in the pulsed mode of welding should be noted. At the same time, it is worth noting the tendency of reducing the quantity and size of single pores (or the length of pore chains) during «uphill» welding as compared to «downhill» welding mode at the same angle during the pulsed mode of laser generation.

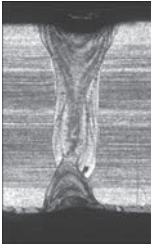


**Figure 3.** Structure of welded joint metal, made in the flat position: *a* — cross-section of the weld,  $\times 30$ ; *b* — center of the weld,  $\times 400$ ; *c* — fusion line,  $\times 400$

**Table 2.** Shapes of penetrations in the plates of AISI 321 steel with angles of inclination to the horizontal plane from 90° to 0° in laser «downhill» and «uphill» welding with different modes of laser radiation

| Welding direction | Angle of inclination, ° | Pulsed mode   | Continuous mode   |
|-------------------|-------------------------|---|---|
|                   |                         | Shape of penetration, magnification   |   |
| Downhill          | 30                      |  ×40   |  ×50   |
|                   | 45                      |  ×40   |  ×25   |
|                   | 60                      |  ×30  |  ×25  |
|                   | 90                      |  ×50 |  ×40 |
| Uphill            | 30                      |  ×50 |  ×30 |
|                   | 45                      |  ×40 |  ×30 |

Table 2. Cont.

| Welding direction | Angle of inclination, ° | Pulsed mode  | Continuous mode  |
|-------------------|-------------------------|--|--|
|                   |                         | Shape of penetration, magnification  |  |
| Uphill            | 60                      |  ×25  |  ×25  |
|                   | 90                      |  ×50  |  ×30  |
| Flat position     | 0                       |  ×50 |  ×30 |

According to the requirements of DSTU EN ISO 13919-1:2015, in order to obtain the highest level of quality «B», the value of the total projection of pores for welded joints of AISI 321 steel of 3 mm thickness, produced by laser welding in different spatial

positions, should not exceed the value of 0.7 %. The analysis of the obtained data allows confirming, that according to this index all the produced welds meet the specified requirements.

It was established that dependence of the penetration area on the angle of inclination at its increase from 0 to 90° has a nonmonotonic nature both during «downhill» as well as in «uphill» welding regardless of the mode of laser radiation (Figure 5). It was established that the maximum values of penetration area in all the modes are observed at an angle of inclination of 45°. This phenomenon can be explained by a change in the character of flows in the melt pool, as well as by a change in the degree of impact of gas protection in the welding zone. However, to formulate the final conclusions, this phenomenon requires an additional comprehensive study.

It should be noted that for the dependences of cross-sectional area in the welds of welded joints of AISI 321 steel of 3 mm thickness, produced by laser welding in different spatial positions (Figure 5), it was characteristic that in a continuous «uphill» mode, the value of cross-sectional area of welded joints at different angles of welding differs by not more than 1.31 times. Whereas during «downhill» welding in a continuous mode of laser radiation, the maximum and

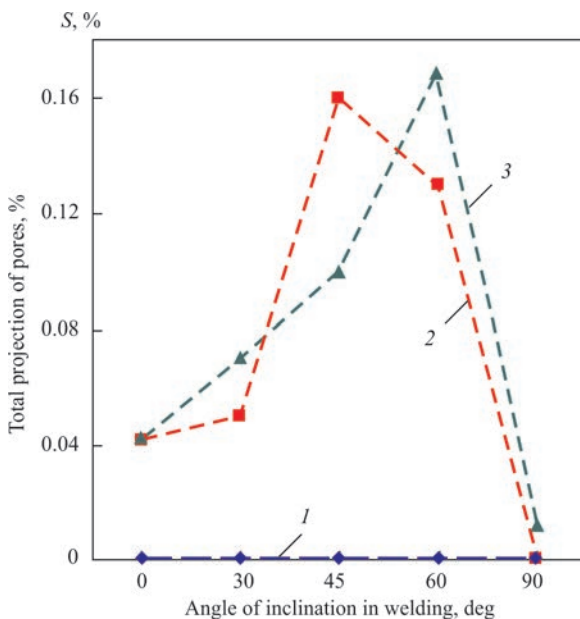


Figure 4. Dependence of total area of projections of pores on parameters of modes of laser welding of AISI 321 steel 3 mm thick, produced in different spatial positions: 1 — continuous mode; 2 — pulsed «uphill» mode; 3 — pulsed «downhill» mode

minimum values of dependences differ by almost 2.1 times (Figure 6). In this case, the maximum cross-sectional areas of the welds produced during «downhill» and «uphill» welding at an angle of inclination of 45° in the continuous mode of laser generation differ by almost 1.5 times. Obviously, this occurs due to a longer stay of welded joint metal at the temperatures higher than the melting point. This leads to an increase in the volume of molten metal pool and, as a result, the welded joint area. It was established that when the mode of laser generation is changed from a continuous to a pulsed one at an angle of inclination of welding of 45°, the tendency of significant increase in the penetration area is absent.

During welding in different spatial positions using the pulsed laser generation mode, the indicated data on the cross-sectional area of welds differ significantly (see Figure 5). Thus, in both pulsed «uphill» and «downhill» welding, the maximum and minimum values of cross-sectional area of welds differ by about 2.5 times for the angles of 0 and 45° (Figure 5). In this case, the cross-sectional areas of welded joints produced during «downhill» and «uphill» welding at the same welding angles in the pulsed mode of laser generation differ by less than 5 %.

Figure 6 shows the dependence of the weld height in different spatial positions on the angle of inclination. The same as for the penetration area, the nature of dependencies is nonmonotonic. However, the difference in the values obtained for «uphill» and «downhill» welding for the vast majority of reference points does not exceed 15 % at one and the same laser generation mode. An interesting fact is that the highest values are observed during welding at an angle of inclination of 45° in the pulsed «downhill» and continuous «uphill» modes (Figure 6). Whereas during welding in a continuous «downhill» and «uphill» pulsed modes, the maximum values are obtained at an angle of inclination of 60°. The values, exceeding the thickness of 3.0 mm in the plates to be welded, are explained by the formation of upper and lower beads of a welded joint at a full penetration of specimens. It is worth noting, that the change in the weld height in the joints of AISI 321 steel with a thickness of 3 mm when changing the angle of inclination during laser welding at a continuous «uphill» mode does not exceed 22 %. Whereas during «downhill» welding in the continuous mode of laser generation, this value amounts to 27 %, and when changing the generation mode into a pulsed one, it approaches to 100 %.

The analysis of the results of investigations performed on the plates and described above made it possible to make a scientifically grounded choice of spatial positions and to select the technological pa-

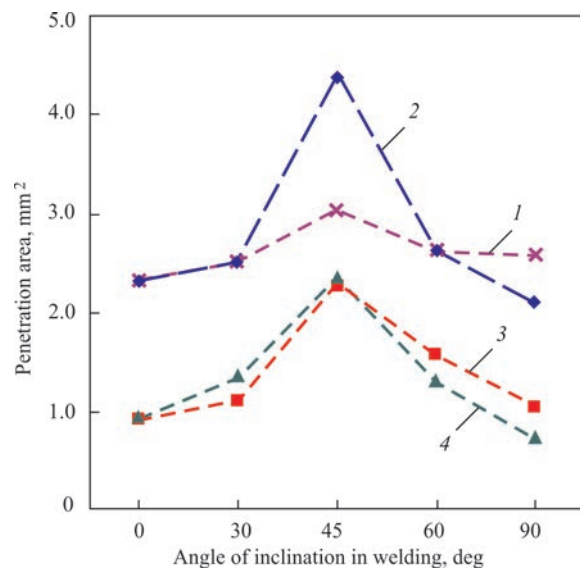


**Figure 5.** Dependence of cross-sectional area of welds in joints of AISI 321 steel 3 mm thick, produced by laser welding in different spatial positions, from the angle of inclination: 1 — continuous «uphill» mode; 2 — continuous «downhill» mode; 3 — pulsed «uphill» mode; 4 — pulsed «downhill» mode

rameters on which it is planned to produce reference butt joints of AISI 321 steel of 3.0 mm thickness. During the choice of spatial positions, the following indices were taken into account: achievement of the maximum penetration depth; quality welded joint formation; absence (or minimum number of splashes); absence (or minimum value) of weld depression; absence (or minimum height) of the «comb» of the upper bead. Based on the mentioned provisions, the flat and vertical spatial positions were selected as the most promising for producing butt welded joints that meet the requirements to the highest quality level «B» according to DSTU EN ISO 13919-1:2015.

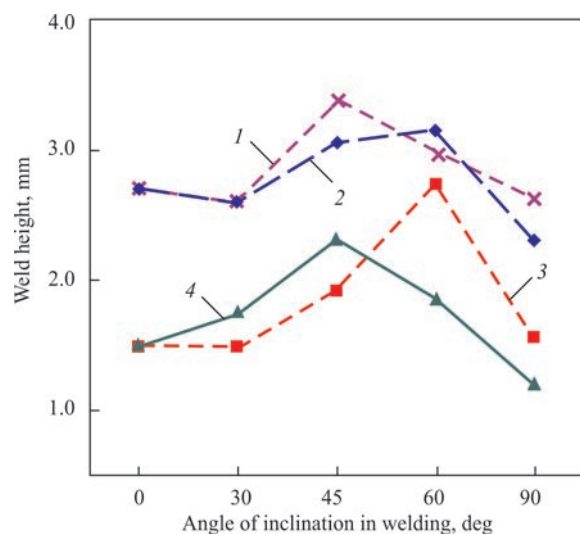


**Figure 6.** Dependence of height of weld in joints of AISI 321 steel 3 mm thick, produced by laser welding in different spatial positions, from the angle of inclination: 1 — continuous «uphill» mode; 2 — continuous «downhill» mode; 3 — pulsed «uphill» mode; 4 — pulsed «downhill» mode

## Conclusions

The spatial position of corrosion- heat-resistant austenitic steel AISI 321in laser welding has a radical impact on the quality level and structure of welded joints.

Reducing the angle of inclination from 90 to 0° during «downhill» and «uphill» welding in the pulsed mode of laser generation leads to increase in both the quantity of pores as well as in their size, whereas in the continuous mode of laser generation, defects in the form of pores are not observed.

In laser welding of butt joints of AISI 321 steel, the most promising are flat and vertical spatial positions, such as those that provide the highest level of quality.

1. Serdar, M., Meral, C., Kunz, M. et al. (2015) Spatial distribution of crystalline corrosion products formed during corrosion of stainless steel in concrete. *Cement and Concrete Research*, **71**, 93–105.
2. Vasantharaja, P., Vasudevan, M., Palanichamy, P. (2015) Effect of welding processes on the residual stress and distortion in type 316LN stainless steel weld joints. *J. of Manufacturing Processes*, **19**, 187–193.
3. Chater, J. (2016) What prospects for stainless steel in 2016. *Stainl. Steel World*, **1(2)**, 1–5.
4. Kumar, A., DebRoy, T. (2007) Heat transfer and fluid flow during gas-metal-arc fillet welding for various joint configurations and welding positions. *Metallurg. and Mater. Transact. A*, **38(3)**, 506–519.
5. Tsai, M. J., Lee, H. W., Ann, N. J. (2011) Machine vision based path planning for a robotic golf club head welding system. *Robotics and Computer-Integrated Manufacturing*, **27(4)**, 843–849.
6. Leskov, G.I., Zhivaga, L.I. (1980) Formation of joints in electron beam welding of thick steels in different spatial positions. *Avtomatch. Svarka*, **10**, 1–5 [in Russian].
7. Sohail, M., Han, S.W., Na, S.J. et al. (2015) Numerical investigation of energy input characteristics for high-power fiber laser welding at different positions. *The Int. J. Adv. Manuf. Technol.*, **80(5–8)**, 931–946.
8. Shelyagin, V., Khaskin, V., Bernatskiy, A. et al. (2018) Multipass laser and hybrid laser-arc narrow-gap welding of steel butt joints. *Mater. Sci. Forum*, **927**, 64–71.
9. Kah, P., Lu J., Martikainen, J., Suoranta, R. (2013) Remote laser welding with high power fiber lasers. *Engineering*, **5(09)**, 700.
10. Seyffarth, P., Krivtsun, I. (2014) *Laser-arc processes and their applications in welding and material treatment*. CRC Press.
11. Artinov, A., Bakir, N., Bachmann, M. et al. (2018) Weld pool shape observation in high power laser beam welding. *Procedia CIRP*, **74**, 683–686.
12. Krivtsun, I., Reisinger, U., Semenov, O., Zabirov, A. (2016) Modeling of weld pool phenomena in tungsten inert gas, CO<sub>2</sub>-laser and hybrid (TIG+ CO<sub>2</sub>-laser) welding. *J. of Laser Applications*, **28(2)**, 022406.
13. Khaskin, V., Korzhyk, V., Sidorets, V. et al. (2016) The influence of the absorption coefficient of laser radiation on the process of laser-arc welding. *American Sci. J.*, **4**, 81–87.

Received 25.10.2019

# XIX INTERNATIONAL INDUSTRIAL FORUM - 2020

INTERNATIONAL TRADE FAIRS

November  
24-27

METAL-WORKING
UKRWELD
HYDRAULIC PNEUMATICS
BEARINGS
UKROBES
UKROUNDRY
UKROBOM AUTOMATIZATION
PATTERNS, STANDARDS AND INSTRUMENTS
HOISTING AND TRANSPORTING STOREHOUSE EQUIPMENT
INDUSTRIAL SAFETY



ORGANIZER:

*International Exhibition Centre*

General Information Partner:

Exclusive Media Partner:

Technical Partner:

International Exhibition Centre

15 Brovarskyi Ave., Kyiv, Ukraine  
“Livoberezhna” underground station

☎ +38 044 201 11 65, 201 11 56, 201 11 58  
e-mail: alexk@iec-expo.com.ua  
www.iec-expo.com.ua  
www.tech-expo.com.ua

# REGULARITIES OF INFLUENCE OF SLM PROCESS PARAMETERS ON THE FORMATION OF SINGLE LAYER FROM THE HIGH-TEMPERATURE NICKEL ALLOY Inconel 718\*

**S.V. Adzhamsky<sup>1,2</sup> and G.A. Kononenko<sup>2,3</sup>**

<sup>1</sup>Oles Honchar Dnipro National University

72 Gagarin Prosp., 49000, Dnipro, Ukraine. E-mail: pk\_dnu@i.ua

<sup>2</sup>LLC «Additive Laser Technology of Ukraine»

144 Rybinska Str., 49000, Dnipro, Ukraine. E-mail: info@alt-print.com

<sup>3</sup>Z.I. Nekrasov Institute of Ferrous Metallurgy of the NAS of Ukraine

1 Starodubov Sq., 49000, Dnipro, Ukraine. E-mail: office.isi@nas.ua

In the work the varieties of additive technologies, their advantages and disadvantages were analyzed. The experiments on selective laser melting (SLM) are described in more detail in order to provide the required microstructure of the synthesized material. The modes that provide stable printing of a single layer were experimentally established. The optimal values of scanning speed and laser power for the alloy Inconel 718 were determined. 12 Ref., 6 Figures.

*Keywords:* SLM process, alloy Inconel 718, laser power, single track, specific volume power, maximum layer density

Additive technologies is a generic name for a group of technologies involving manufacture of products according to digital models using the method of layer-by-layer addition of material. At the same time, a product is manufactured step by step by forming a layer of material, its solidifying or fixing in accordance with the data of 3D-model and joining with the previous layer. The power source may be an electron or laser beam.

There are various additive manufacturing processes, such as selective laser melting, direct laser deposition, electron beam melting, wire feed, shaped metal deposition, ultrasonic compaction, vortex interweaving and free shape friction for the manufacture of metal components.

First of all, an interest to additive technologies and direct printing or growing of metal parts as an alternative to traditional technologies arose in aviation, space industry, medicine and power engineering. In this case, the main driving factor was economic feasibility. This applies especially single complex products, the manufacturing of which by traditional methods is much more expensive than with the use of additive technologies.

Advantages of additive technologies are the following:

- improved properties of finished products. Due to the layered building, the products have a unique set of properties. For example, the parts created in a metal

3D printer by their mechanical properties, density, residual stresses and other properties surpass their analogues produced by casting or mechanical treatment;

- big economy in raw materials. Additive technologies use that amount of material in practice, which is needed to manufacture a product, whereas during traditional methods of manufacturing, the losses of raw materials can amount up to 80–85 %. The building takes place with the help of layer-by-layer addition of the required amount of material to the «body» of a product. 97–99 % of the powder, not involved in the building is recyclable after sieving. 3–9 % of the material involved in the building of supports is utilized together with a rejected non-fused powder that did not undergo a sieving operation;

- possibility of manufacturing products with a complex geometry. Equipment for additive technologies allows manufacturing objects that cannot be made by other means. For example, a part inside a part or very complex cooling systems based on array structures (this cannot be made neither by casting nor by stamping);

- mobility of production and acceleration of data exchange. Additive technologies are based on a computer model of a future product, which can be transferred in a very few minutes to the other end of the world — and immediately start the production;

- high accuracy and repeatability;

\*Based on the materials of the report presented at the international conference «Beam Technologies in Welding and Materials Processing», September 9–13, 2019, Odessa.

- shortens the cycle of R&D works, providing the creation of complex-shaped parts without the use of equipment;

- allows reducing the weight by creating objects with inner cavities;

- the technology allows working with a wide range of metal powder compositions: stainless and tool steels, aluminum, titanium, nickel, cobalt-chromium, copper alloys and many other.

Additive technologies also have some disadvantages, in particular:

- surface quality of the products, their dimensional accuracy and minimum thickness of the elements are largely depend on the specific method and process parameters;

- need to manufacture supporting structures together with a part with their subsequent removal;

- dependence of structure and properties on the direction of growing, specific technology and equipment;

- limited product dimensions (limited by the working chamber or equipment area).

However, despite these drawbacks, the ease of using additive technologies is confirmed by numerous investigations and applications in real industries.

The method of selective laser melting (SLM) is an innovative technology for the manufacture of complex products by laser melting of metal powder according to mathematical 3D-models. This process successfully replaces traditional production methods, since the physical and mechanical properties of products built using SLM technology are often superior to the properties of products manufactured with the use of traditional technologies, so this technology with the use of powder is one of the most popular and successful.

In selective laser melting, metal powder bonding is achieved by melting and solidifying of a small volume of material in a track using one or more powerful lasers. In other words, the laser beam scans the powder layer and melts the powder particles under the beam, creating a small pool of molten metal and a thin track of solidified metal behind. By repeating single tracks with a clearly distinct overlapping (distance between the tracks), a

layer of cross-section is created. By repeating this layer-by-layer deposition, the entire part is built. The installation and the whole process are controlled by a computer, on which the loaded mathematical model goes through several stages of preparation with the creation of supporting structures, trajectories, and procedures of beam scanning for each generated model layer, adjustment of a technological process for operation with a one or another selected material, etc. The process of products building occurs in the chamber of SLM machine, filled with an inert gas — argon or nitrogen, depending on the type of powder from which the building occurs, with its laminar flow. An admissible oxygen content is less than 0.15 %. The almost complete absence of oxygen avoids oxidation of a consumable, which enables printing with such materials as aluminum and titanium.

Depending on the geometry, the layers are divided into zones, where each one is assigned a separate identifier, according to which the movement trajectories are built and the laser beam parameters are set. These identifiers can be divided into three main groups: down-skin, in-skin and up-skin (Figure 1, *a*). At the same time, in each group its own subgroups are created: hatches, border and fill border as is shown in Figure 1, *b*.

The laser beam is moved using a system of mirrors on a quick-response drive. However, one of the problems in the technical aspect of the process is providing the stability of the laser beam spot diameter. The spot diameter is defined as a diameter in the beam waist, which is 86.5 % of the total power and corresponds to a beam diameter of  $1/e^2$  in the working plane for Gaussian beams. It depends on the light source (laser wavelength and the quality of the conjugated laser beam), as well as on the aperture and focal length of the scanning system. As a result, a curvilinear focal surface is formed, the radius of which corresponds to the focal length of the system. There are basically two different approaches to solving this problem: the use of corrective F-Theta lenses and the control of laser movement along the *z* axis.

From the point of view of materials science, the problem of SLM technology is providing the required microstructure of a synthesized material and reducing

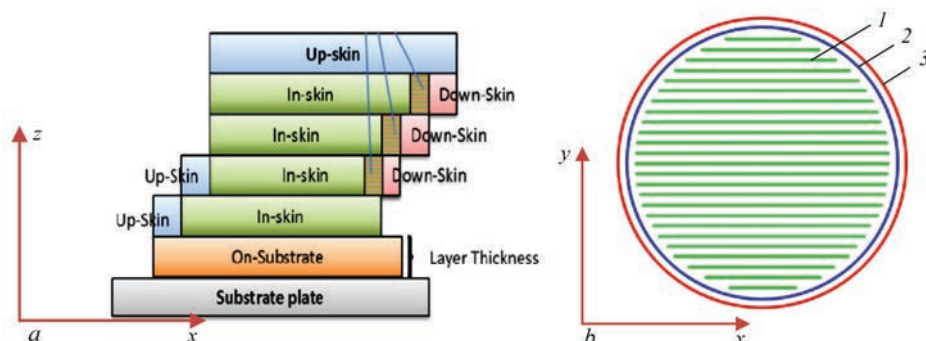


**Figure 1.** Formation of layers in the direction of growing a part (*a*), subgroups of tracks (*b*): 1 — hatches; 2 — border; 3 — fill border

the porosity of the produced material, which is typical for this technology. The values of porosity depend on the material used, parameters of the fusion mode, quality of the source powder, etc. The values of porosity for aluminum alloys can reach 4–5 %, for titanium alloys — up to 2 %, for steels and nickel alloys — less than 0.2 %. The products manufactured by selective laser melting, may contain defects. These are mainly pores and microcracks.

There are two types of pores: pores of a round shape and pores of irregular shape (lack of fusion) [1]. Round pores are formed for the following main causes: atmospheric gases absorbed by the molten pool, and gas mixed with the powder, which fails to be released from the molten pool before solidification. Bubbles of gas in a liquid have a spherical shape, which is maintained after solidification of the metal [2, 3]. Another cause is the capture of gas inside the powder particles during gas spraying [4]. However, the main defect is an irregular pore, which is formed because of the unstable shape of the molten pool or as a result of insufficient penetration of the powder layer. As a result, in places where the particles did not melt completely, or the fusion of the molten powder particles with the previously treated layer did not occur, flat pores are formed that are located perpendicular to the growing direction [2, 5–7]. The pores of the second type have a significantly greater effect on mechanical properties of the material due to their larger size, as well as their flat shape [3, 5]. To reduce the porosity in critical final products, hot isostatic pressing is used, which in many cases, provides a significant improvement in the quality of products after SLM [8].

A high power and localization of the heating source and a high speed of its movement contribute to the formation of large thermal gradients in the metal after building using the SLM method. Although these thermal gradients directly affect the formed microstructure of the metal, they also contribute to the formation of high thermal stresses, which can be sufficiently high and lead to buckling of products, as well as a change in their mechanical properties. Residual stresses, as a rule, are not directly taken into account, but considered as a hidden parameter, and sometimes they are not taken into account at all.

These defects have a significant effect on mechanical properties, such as ductility during tensile tests, fracture toughness and fatigue strength. To manufacture high-quality products, it is necessary to select manufacturing parameters in such a way as to minimize the resulting discontinuities in the metal. The structure and properties of a final product manufactured by selective laser melting depend on a large number of technological parameters. At present, up to 120 different factors are

identified, affecting the quality and operational characteristics of the produced objects [9, 10]. A variety of influencing factors shows the complexity of physical processes occurring during SLM and the need in a scientifically-grounded choice of optimal values of the main technological parameters. Among the most important of them, laser radiation power, speed of scanning laser beam along the powder surface, thickness of a poured powder layer, distance between the melted tracks, diameter of the laser focal spot, melting strategy, i.e., the trajectory of the laser beam movement and also the chemical composition, structure and dispersion of the initial powder can be mentioned.

Porosity is considered as one of the main problems of objects manufactured by the SLM method. However, providing the constancy of geometric characteristics of each separate track, such as width, height, diameter and its good adhesion with the previous layer, which is determined by the penetration depth, it is possible to manufacture objects with the porosity of less than 1 %.

A track with a constant geometric shape, without breaks along the entire length and with penetration into the substrate is called stable. To manufacture objects with minimal porosity, crystallization of stable tracks is required.

At the first stage, the influence of the following parameters was studied: laser power and its movement speed on the size and shape of single tracks. This set of variable parameters was selected because of their direct contribution to the volume energy density and due to the possibility of their simultaneous variation in the manufacture of a set of specimens. In this case, the intervals of varying the parameters were the following for the laser power — 50–400 W at an increment of 30 W, for laser speed 450–1000 mm/s at an increment of 50 mm/s. The thickness of the applied powder layer was 50  $\mu\text{m}$ .

The appearance and geometric parameters of single tracks obtained during the experiment were analyzed. At a low power, the powder did not fuse with the substrate. At a high speed of scanning, the effect of the formation of balls or lumps was observed. At a high power, the melt boils and the pressure of its vapor causes distortion of sintered tracks. The microstructure of the cross-section of single tracks was investigated. According to the results of the experiment, the modes were established that provide the formation of a molten pool of optimal geometry: the depth of the melting zone should exceed the layer thickness by about one and a half to two times, the ratio of the depth to the width of the track should be at a level from 1 to 1.5:

$$P = 110 \text{ W}, V = 450\text{--}500 \text{ mm/s};$$

$$P = 140 \text{ W}, V = 600\text{--}700 \text{ mm/s};$$

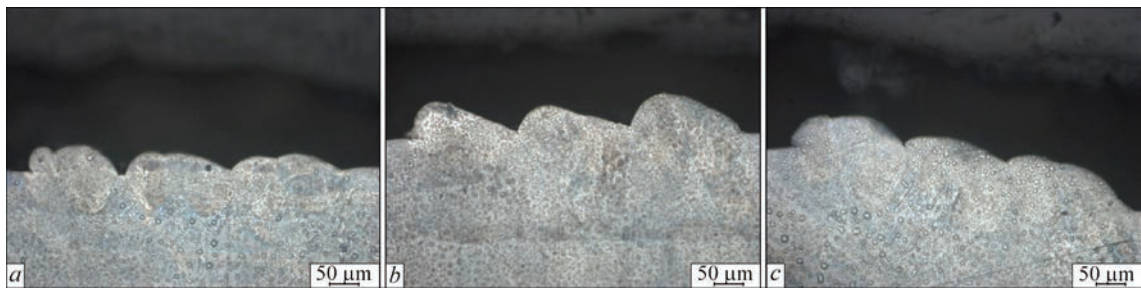


**Figure 2.** Microstructure of single layer at a laser power of 140 W and scanning speed: *a* — 1000 mm/s ( $E = 28 \text{ J/mm}^3$ ); *b* — 950 mm/s ( $E = 31 \text{ J/mm}^3$ ); *c* — 850 mm/s ( $E = 33 \text{ J/mm}^3$ )



**Figure 3.** Microstructure of single layer at a laser power of 200 W and scanning speed: *a* — 800 mm/s ( $E = 50 \text{ J/mm}^3$ ); *b* — 750 mm/s ( $E = 53 \text{ J/mm}^3$ ); *c* — 700 mm/s ( $E = 57 \text{ J/mm}^3$ )

- $P = 170 \text{ W}, V = 600\text{--}700 \text{ mm/s};$
- $P = 200 \text{ W}, V = 650\text{--}800 \text{ mm/s};$
- $P = 230 \text{ W}, V = 800\text{--}950 \text{ mm/s}.$

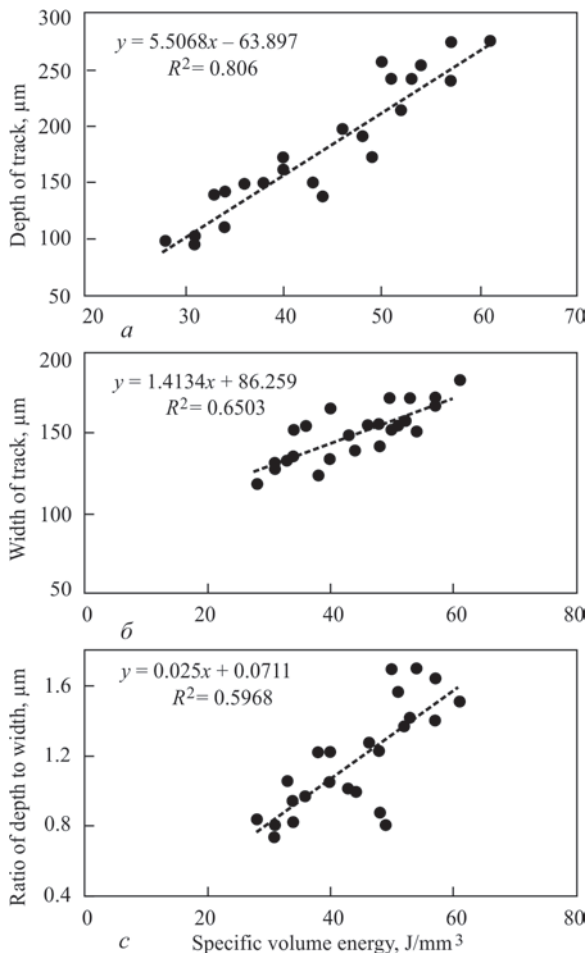


**Figure 4.** Geometrical parameters of the track in a single layer at different levels of specific volume energy

In the literature, to evaluate the energy input of the heating source, the volume energy density is used since it allows taking into account the contribution of the basic technological parameters of selective laser melting and their effect on the fused material [11, 12]. To calculate the volume energy density, the following equation was used:

$$E = P/(Vdt), \quad (1)$$

where  $E$  is the energy density,  $\text{J/mm}^3$ ;  $P$  is the laser power,  $\text{W}$ ;  $V$  is the laser scanning speed,  $\text{mm/s}$ ;  $d$  is the layer thickness,  $\text{mm}$ ;  $t$  is the distance between laser passes,  $\text{mm}$ .

The energy density should be such as to provide a complete remelting of the powder and its fusion with the substrate. However, as is seen from the presented data, the specific volume energy of the mentioned modes during calculation for the interval between the tracks of 0.1 mm and a layer thickness of 50  $\mu\text{m}$  varies in a wide range: from 44 to 61  $\text{J/mm}^3$ . In addition, when creating a single layer, overlapping of neighboring tracks occurs, as a result of which the molten pool of the created track receives additional thermal influence from the cooling metal of the previous track, which will affect its geometry, properties and structure formation. In the experiment, the modes with a specific volume energy were calculated, which is by 30 % less than the optimal for single tracks.

The aim of the experiment is to specify the modes that provide a stable high-quality printing of a single layer and volume specimens to observe the optimality of the geometry of the pools of tracks in single layers and the minimum porosity in volume specimens.

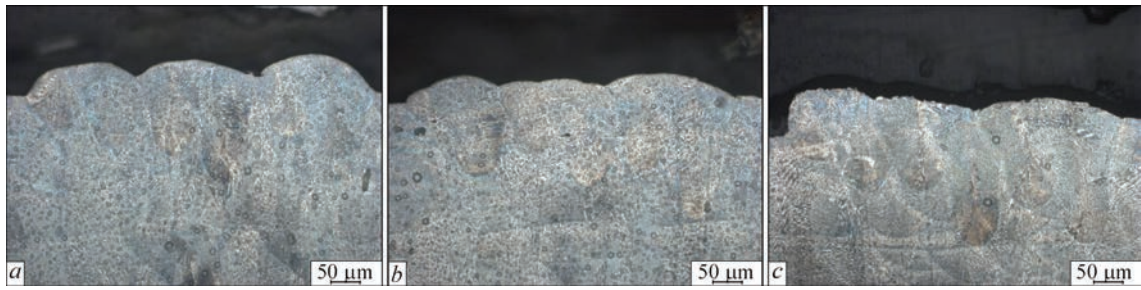


**Figure 5.** Microstructure of single layer at a laser power of 170 W and scanning speed: *a* — 900 mm/s ( $E = 38 \text{ J/mm}^3$ ); *b* — 850 mm/s ( $E = 40 \text{ J/mm}^3$ ); *c* — 700 mm/s ( $E = 48 \text{ J/mm}^3$ )



**Figure 6.** Microstructure of volume specimens manufactured at different levels of volume laser power

In the experiment, single layers were created from six single tracks printed with an interval of 0.1 along the zig-zag trajectory. Single layers, manufactured from calculated modes with a energy reduced relative to optimal ones for single tracks had an unstable shape. This was especially clear for the first track. With an increase in the specific volume energy, the outer tracks had a stable shape. In the cross-section of the specimens microstructural examinations were carried out. In Figures it can be seen that, at the level of energy being 28–33 J/mm<sup>3</sup>, the amount of power turned out to be insufficient for a high-quality overlapping of neighboring tracks (Figure 2), and at the level of specific energy being higher than 48–50 J/mm<sup>3</sup>, the penetration depth of neighboring tracks became nonuniform (Figure 3).

After crystallization of the track, there are areas depleted of powder next to it. Therefore, when melting the neighboring track, a smaller amount of powder was used which led to a decrease in its height. In addition, the absorption and reflection coefficients of laser radiation in the powder and remelted material are significantly different, which had an additional effect on physics of the process.

In this work, the average depth and width of the track in a single layer were determined. Figure 4 shows the results of the investigation. The functional dependence of the track depth on the specific volume energy with a sufficient level of the approximation validity coefficient was established. An equation was obtained, with the help of which the optimal level of energy required to provide penetration to the value of not more than two layers was determined. It amounted to 39 J/mm<sup>3</sup>.

For this energy level, the average ratio of depth to width of the tracks is at the optimum level. Figure 5 shows the microstructure of single layers with an optimal energy level, the overlap of adjacent tracks and their penetration depth are uniform.

When analyzing volume specimens, manufactured according to the same modes as single layers, the conclusion about the optimal level of specific volume energy of 38–40 J/mm<sup>3</sup> is confirmed. It was shown that at a higher energy level, deep penetration conditions are realized, and at a lower volume energy, guaranteed overlapping of adjacent tracks is not provided (Figure 6).

However, our previous investigations for single tracks found that the intensity of the scanning speed effect on their geometric parameters is significantly higher than the laser power. And the same level of volume energy can be achieved by a different combination of laser power and scanning speed. Further investigations will be devoted to establishing a preferred method of achieving an optimal level of energy input.

## Conclusions

- As a result of investigations, the optimal values of scanning speed and laser power for the alloy Inconel 718 were determined from the point of view of producing a stable single track under the condition of forming a melt pool with a depth of up to two layers.

- The optimal process conditions for the Inconel 718 alloy were specified to produce single layers with the geometry of the tracks corresponding to the set conditions: the average depth of the tracks to two layers, the average ratio of depth to the width of the track is up to 1.5.

- The dependence of the average depth of the track of a single layer on the specific volume energy and the optimal level of this characteristic were established.

- The results on the optimal level of specific volume energy obtained during the investigation of single layers on volume specimens were confirmed: with the implementation of optimal conditions, specimens of maximum density were produced.

1. Thijs, L., Verhaeghe, F., Craeghs, T. et al. (2010) A study of the micro-structural evolution during selective laser melting of Ti–6Al–4V. *Acta Mater.*, **58**(9), 3303–3312.
2. Simonelli, M., Tse, Y.Y., Tuck, C. (2014) Effect of the build orientation on the mechanical properties and fracture modes of SLM Ti–6Al–4V. *Materials Sci. and Eng. A*, **616**, 1–11.
3. Frazier, W.E. (2014) Metal additive manufacturing: A review. *J. of Materials Eng. and Performance*, **23**(6), 1917–1928.
4. Parimi, L.L., Clark, R.G.A.D., Attallah, M.M. (2014) Micro-structural and texture development in direct laser fabricated IN718. *Mater. Charact.*, **89**, 102–111.
5. Wu, M.W., Lai, P.H., Chen, J.K. (2016) Anisotropy in the impact toughness of selective laser melted Ti–6Al–4V alloy. *Materials Sci. and Eng. A*, **650**, 295–299.
6. Chlebus, E. et al. (2011) Microstructure and mechanical behaviour of Ti–6Al–7Nb alloy produced by selective laser melting. *Materials Characterization*, **62**(5), 488–495.
7. Vilaro, T., Colin, C., Bartout, J.D. As-fabricated and heat-treated microstructures of the Ti–6Al–4V alloy processed by selective laser melting. *Metallurgical and Materials Transact. A*, **42**(10), 3190–3199.
8. Qiu, C., Adkins, N.J.E., Attallah, M.M. (2013) Microstructure and tensile properties of selectively laser-melted and of HIPed laser-melted Ti–6Al–4V. *Materials Sci. and Eng. A*, **578**, 230–239.
9. Santos, E.C. et al. (2006) Rapid manufacturing of metal components by laser forming. *Int. J. of Machine Tools & Manufacture*, **46**, 1459–1468.
10. Zakiev, S. et al. (2006) Modelling of the thermal processes that occur during laser sintering of reacting powder compositions. *Appl. Phys. A*, **84**, 123–129.
11. Meier, H., Haberland, C. (2008) Experimental studies on selective laser melting of metallic parts. *Materialwissenschaft und Werkstofftechnik*, **39**(9), 665–670. DOI: 10.1002/mawe.200800327.
12. Islam, M., Purtonen, T., Piili, H. (2013) Temperature profile and imaging analysis of laser additive. *Physics Procedia*, **41**, 828–835.

Received 29.10.2019

# IMPACT OF HIGH-FREQUENCY PEENING AND MODERATE CLIMATE ATMOSPHERE ON CYCLIC FATIGUE LIFE OF TEE WELDED JOINTS WITH SURFACE FATIGUE CRACKS

V.V. Knysh, S.O. Solovei, L.L. Nyrkova, A.O. Gryshanov and V.P. Kuzmenko

E.O. Paton Electric Welding Institute of the NAS of Ukraine

11 Kazymyr Malevych Str., 03150, Kyiv, Ukraine. E-mail: [office@paton.kiev.ua](mailto:office@paton.kiev.ua)

The paper presents the results of investigations of the effectiveness of application of the technology of high-frequency mechanical peening to improve the residual fatigue life of tee welded joints of 15KhSND steel with surface fatigue cracks and corrosion damages characteristic for structures after long-term service under the conditions of moderate climate of the central regions of Ukraine. Corrosion damages on the surface of joints were obtained by exposure in G4 hydrostat at higher temperature and relative humidity of air for 1200 h. It was experimentally established that strengthening of tee welded joints with surface fatigue cracks of up to 10 mm length and characteristic fatigue damages by the technology of high-frequency mechanical peening increases their cyclic fatigue life by up to 10 times. It is shown that application of the technology of high-frequency mechanical peening of welded joints, which contain fatigue cracks of 20 mm and greater length, does not lead to improvement of cyclic fatigue life and is not effective. 10 Ref., 2 Tables, 5 Figures.

*Keywords:* tee welded joint, corrosive environment, fatigue, accelerated corrosion testing, high-frequency mechanical peening, improvement of cyclic fatigue life

To improve the characteristics of welded joints of metal structures of long-term service (bridges, cross-overs, off-shore platforms, etc.) to fatigue resistance both in the initial state as well as during repair and restoration works, the methods of surface plastic deformation (SPD) of metal are widely used, including the technology of high frequency mechanical peening (HMP) [1–4]. The experimental investigations established a high efficiency of applying HMP technology for welded joints not only with accumulated fatigue damages, but also with corrosion damage caused by the long-term influence of climatic factors of the environment [5]. From the analysis of the literature data [6–10] it is known that the use of SPD methods contributes to increase in the cyclic life of structural elements even with fatigue cracks. It is shown that the efficiency of SPD methods depends on type of strengthening treatment and depth of the crack. For example, after applying a pneumatic hammer treatment, the residual cyclic life of tee welded joints with surface fatigue cracks of 1.0–1.5 mm depth is increased by 10 times, with surface fatigue cracks of about 3.0 mm depth — by 1.1–1.25 times, and with surface fatigue cracks of a depth of more than 5.0 mm — the cyclic life is not increased [8]. During strength-

ening tee welded joints with surface fatigue cracks of up to 1.0 mm depth applying HMP, the residual life is increased by 10 times, with surface fatigue cracks of 2.0 mm depth — by 5 times, and with upper fatigue cracks of about 4.5 mm depth — the cyclic life is not increased [10]. However, at present there is no data on the effectiveness of HMP technology on welded joints of metal structures, which are operated under the influence of climatic factors of the environment and contain surface fatigue cracks of negligible depth.

The aim of this work is to investigate the residual cyclic life of tee welded joints with surface fatigue cracks and corrosion damage, which are characteristic to welded metal structures after a long-term service under the conditions of moderate climate of the central regions of Ukraine, after their strengthening applying HMP technology.

**Material and procedure of investigations.** The experimental investigations were carried out on the specimens of tee welded joints of low-alloy 15KhSND steel ( $\sigma_y = 400$  MPa,  $\sigma_t = 565$  MPa), which is widely used for manufacture of metal structural elements of a long-term service (for example, in the track structures of railway and automobile bridges), has a high strength, a good weldability, stable in atmospheric

V.V. Knysh — <http://orcid.org/0000-0003-1289-4462>, S.O. Solovei — <http://orcid.org/0000-0002-1126-5536>,

L.L. Nyrkova — <http://orcid.org/0000-0003-3917-9063>, A.O. Gryshanov — <http://orcid.org/0000-0003-1044-2374>,

V.P. Kuzmenko — <http://orcid.org/0000-0002-9395-7455>

© V.V. Knysh, S.O. Solovei, L.L. Nyrkova, A.O. Gryshanov and V.P. Kuzmenko, 2020

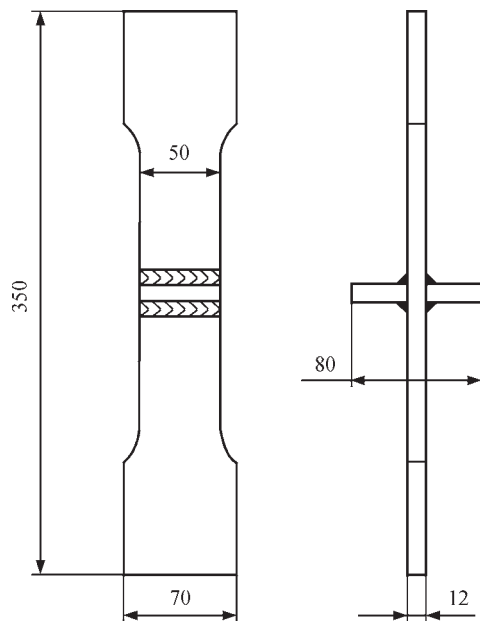


**Figure 1.** Shape and geometric dimensions of specimens of tee welded joint

conditions and is serviceable in the temperature range from  $-70$  to  $45$  °C.

Workpieces for specimens of welded joints were cut out from a hot-rolled sheet metal with a thickness of 12 mm of the 12<sup>th</sup> category in the direction of rolling. Tee welded joints were produced by welding-on transverse stiffeners using manual arc welding with the electrodes of grade UONI 13/55 (also of 15KhSND steel) to the workpieces of 350×70 mm in size on both sides by fillet welds. The root (first weld) was produced by the electrodes with a diameter of 3 mm, the second weld was formed by the electrodes with a diameter of 4 mm. The shape and geometric dimensions of specimens of tee welded joints are shown in Figure 1. The thickness of the specimen is predetermined by a widespread use of rolled metal with a thickness of 12 mm in engineering welded metal structures, and the width of the working part of 50 mm was chosen based on the power of the test equipment.

All the fatigue tests were performed in the URS-20 servo-hydraulic testing machine at an alternating zero-to-tension loading with a cycle asymmetry  $R_{\sigma} = 0$  and a frequency of 5 Hz at a regular load. At the first stage, fatigue tests were carried out at the maximum values of the applied stresses of 180 MPa cycle in order to initiate and propagate small-sized fatigue cracks on the surface of specimens. This level of applied maximum stresses is close to the boundary of the limited endurance of these joints on the basis of  $2 \cdot 10^6$  cycles of stress changes. In order to avoid the difficulties associated with a reliable determination of depth of a fatigue crack during investigations, as a criterion for completing the fatigue tests, the achievement of a set size from 5 to 30 mm by a crack on the

specimen surface was chosen. During these tests, in the weld area the specimens were lubricated with an indicator fluid consisting of kerosene and toner. After the formation of a crack of a set length (all cracks were formed along the line of transition of the weld metal to the base metal) on the surface of the specimen the remnants of the indicator fluid were removed by blowing-down with a compressed air. Indicator fluid was no longer used in the further tests of specimens, which enabled the determination of a clear front of the initial crack on the fractures of welded joints. After the propagation of a crack on the surface of the specimens to the specified size, accelerated corrosion tests were carried out under the conditions simulating the effect of the moderate climate of the central regions of Ukraine, according to the procedure [5]. Therefore, the specimens of welded joints were exposed in the G4 hydrostat at a temperature of 40 °C and at a relative humidity of 100 % for 1200 h. Thus, as a result of previous fatigue and accelerated corrosion tests, the test specimens had damages characteristic to damages of welded joints of metal structures after a long-term service at the variable loading under the conditions of a moderate climate.

During preparation of specimens with surface fatigue cracks and corrosion damages for fatigue testing, their gripping parts were cleaned again from corrosion damages. The weld zone was not cleaned from corrosion products to metallic luster. One part of the specimens was left in the nonstrengthened condition and the other was strengthened by HMP technology. Strengthening of welded joints by HMP technology was performed in the USTREAT-1.0 equipment, where a hand-held compact impact tool with a piezoceramic converter was connected to an ultrasonic generator with a output power of 500 W. In the treatment of welded joints by HMP technology, not only the fusion line containing a fatigue crack was subjected to surface plastic deformation, but all four lines of transition of the weld metal to the base metal of a tee joint. As a device for strengthening a single-row four-striker head with a diameter of 3 mm was used. The strengthening was performed without a preliminary cleaning of surface from the corrosion products.

Thus, fatigue tests were performed on two series of specimens:

- specimens of tee welded joints with surface fatigue cracks of 5–30 mm length and corrosion damages (first series);
- specimens of tee welded joints with surface fatigue cracks of 5–30 mm length and corrosion damages that were strengthened by HMP technology (second series).

**Table 1.** Cyclic life of tee welded joints with corrosion damages and surface fatigue cracks

| Number of specimen | $l_{cr}$ , mm | $N_{cr}$ , cycles | $\sigma_{max}^{unstrength}$ , MPa | $N_{cr}^{unstrength}$ , cycles | Result                         |
|--------------------|---------------|-------------------|-----------------------------------|--------------------------------|--------------------------------|
| 2272               | 7             | 1531300           | 150                               | 2000000                        | Not fractured                  |
| 2277               | 10            | 1164000           | 180                               | 1327500                        | Fracture along the fusion line |
| 2279               | 10            | 826700            | 190                               | 647600                         | Same                           |
| 2278               | 12            | 811800            | 200                               | 177800                         | ->-                            |
| 2275               | 15            | 1137800           | 220                               | 35900                          | ->-                            |
| 2273               | 7             | 1735700           | 200                               | 656300                         | ->-                            |
| 2274               | 25            | 853100            | 220                               | 29500                          | ->-                            |
| 2276               | 20            | 1626800           | 200                               | 48400                          | ->-                            |

Note.  $l_{cr}$  is the crack length before corrosion tests, established by the method of kerosene test;  $N_{cr}$  is the cyclic life before initiation of a crack of a set length at the maximum applied stresses of 180 MPa;  $\sigma_{max}^{unstrength}$  is the maximum cycle stresses applied to the specimen with a crack after corrosion tests in the G4 chamber for 1200 h;  $N_{cr}^{unstrength}$  is the residual cyclic life of the specimen with a fatigue crack of a set length and corrosion damages.

Experimental investigations of residual life of the mentioned welded joints were carried out before a complete fracture of the specimens or exceeding the tests base of  $2 \cdot 10^6$  cycles of stress changes.

**Test results.** The results of fatigue tests of tee welded joints of 15KhSND steel with fatigue cracks without HMP strengthening (first series) are given in Table 1 and in Figure 2. Figure 2 also shows the data of tee welded joints after  $2 \cdot 10^6$  cycles at applied maximum stresses of 150 MPa (without fatigue cracking), corrosion tests in G4 hydrostat for 1200 h without and with subsequent strengthening by HMP technology obtained in [5].

The residual cyclic life of tee welded joints of 15KhSND steel with the surface cracks of up to 10 mm length after corrosion tests at elevated temperatures and a relative humidity stay for 1200 h at the level of residual life of welded joints, which were subjected to cyclic loading of  $2 \cdot 10^6$  cycles at maximum stresses of 150 MPa (without cracking) and corrosion testing. As the length of the initial crack increases, the residual life of the joints decreases (see Table 1, Figure 2). As far as the specimen 2272 was not fractured before  $2 \cdot 10^6$  cycles of stress changes, then in order to determine the dimensions (depth and length) of the initial crack of the specimen, it was destroyed at cyclic loading at the levels of the maximum applied stresses increased to 280 MPa. The fractures of specimens of tee joints with surface cracks and corrosion damages are shown in Figure 3. As is seen, the proposed method allows a clear determination of the geometric dimensions of the initial crack on the fractures after the of the specimens destruction. However, the established length of the initial fatigue cracks on the surface was found to be 2–3 mm longer than when determined directly during cyclic loading. Despite the fact that all fatigue cracks were initiated along the fusion zone in the center of the specimen, the compress-

sion ratio of the surface crack (the ratio of crack depth to half-length) in them is different. We believe that this is caused by propagation of cracks in different fields of residual welding stresses, predetermined by the order of producing fillet welds.

The results of fatigue tests of tee welded joints of 15KhSND steel after the formation of surface fatigue cracks, corrosion tests in the G4 hydrostat for 1200 h and with a subsequent strengthening by HMP technology (second series) are given in Table 2 and Figure 2. The obtained experimental data indicate that the effectiveness of applying HMP technology for the specimens of the second series is actually determined by geometric dimensions of the fatigue crack formed before treatment. Thus, strengthening of tee welded joints with surface fatigue cracks of up to 10 mm length by using HMP technology increases their cyclic life by up to 10 times. Scattering in the experi-

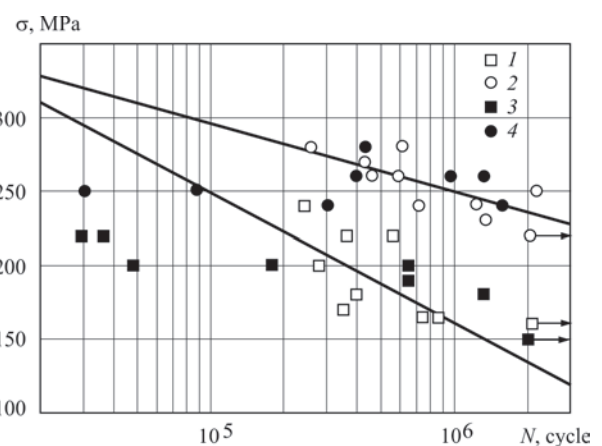


**Figure 2.** Fatigue curves of tee welded joints of 15KhSND steel: 1 — after 2 mln cycles and exposure in the G4 chamber for 1200 h [5]; 2 — after 2 mln cycles, exposure in the G4 chamber for 1200 h and a subsequent strengthening by HMP technology [5]; 3 — after testing before the formation of surface fatigue cracks and exposure in the G4 chamber for 1200 hours; 4 — after testing before the formation of fatigue surface cracks, exposure in the G4 chamber for 1200 h and a subsequent strengthening by HMP technology

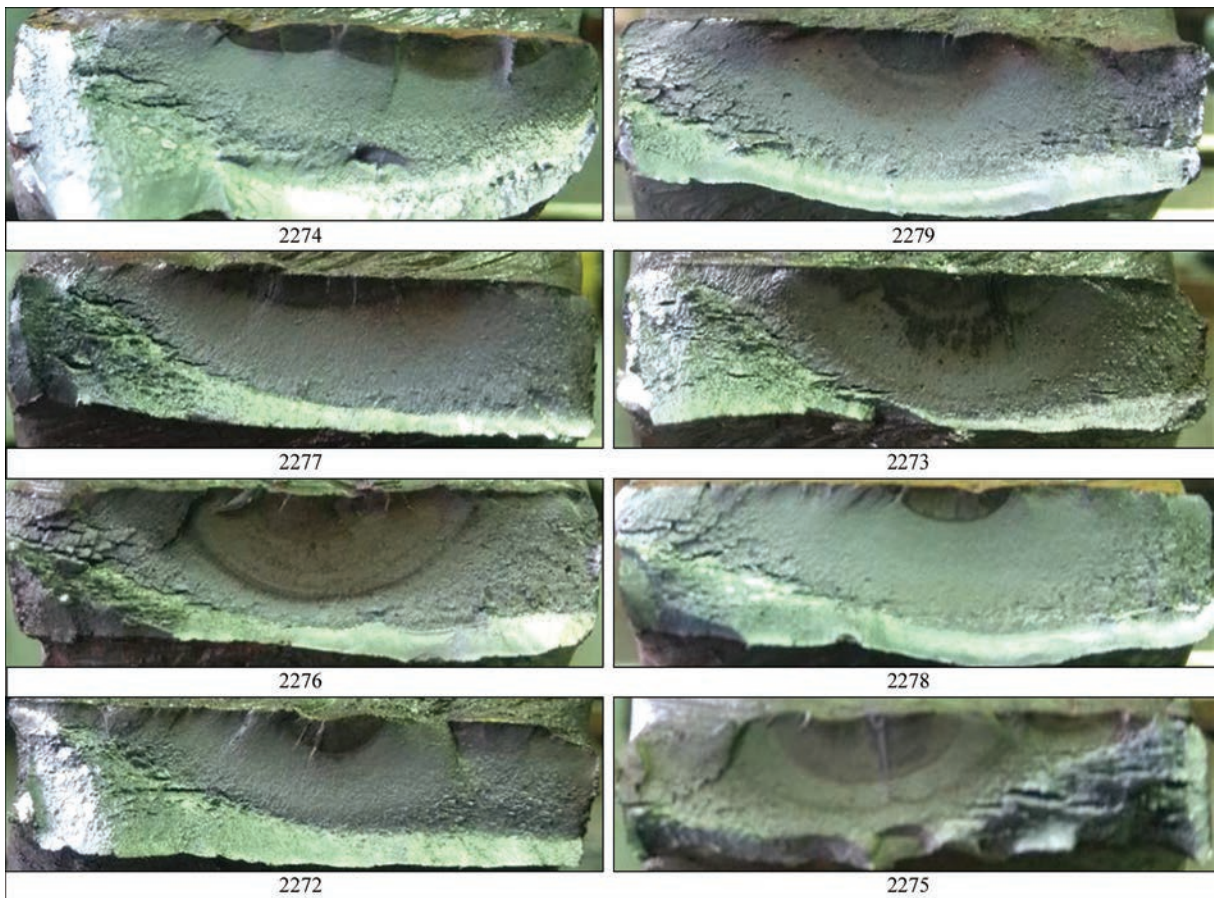


**Figure 3.** Fatigue fractures of specimens of tee welded joints of 15KhSND steel with fatigue surface cracks which were not strengthened by HMP after exposure in the G4 chamber for 1200 h (see Table 1)

mental data of such joints is within the range of the fatigue-free cracks strengthened by HMP at a set level of fatigue-corrosion damages (life of  $2 \cdot 10^6$  cycles of stress changes + G4 chamber for 1200 h). The use of HMP technology for welded joints containing fatigue cracks of 20 mm length or more does not lead to increase in the cyclic life and is ineffective (Table 2). Three specimens (2155, 2156, and 2178), which con-

tained fatigue cracks of 5 mm length, fractured far from the weld along the base metal (Figure 4) after strengthening by HMP. The cracks in the specimens 2155 and 2156 initiated from caverns in the surface hot-rolled metal layer, and in the specimen 2178 from a notch on the gripping part of the specimen, formed during its clamping in the test machine (Figure 5). Other specimens were fractured from fatigue cracks

**Table 2.** Cyclic life of tee welded joints with corrosion damages and surface fatigue cracks after their strengthening by HMP technology

| Number of specimen | $l_{cr}$ , mm | $N_{cr}$ , cycles | $\sigma_{max}^{strength}$ , MPa | $N_{cr}^{strength}$ , cycles | Result  |
|--------------------|---------------|-------------------|---------------------------------|------------------------------|---|
| 2155               | 5             | 432200            | 260                             | 1335200                      | Fracture of base metal at a distance of 25 mm from the weld |
| 2156               | 5             | 292900            | 260                             | 972700                       | Fracture of base metal at a distance of 40 mm from the weld |
| 2175               | 10 + 10*      | 960700            | 280                             | 434200                       | Fracture along the fusion line                              |
| 2180               | 10 + 8 + 6*   | 401800            | 260                             | 396000                       | Same  |
| 2177               | 20            | 1138000           | 250                             | 30700                        | —>—   |
| 2178               | 5             | 261100            | 240                             | 1588100                      | Fracture of base metal in the gripping part of the specimen |
| 2179               | 10            | 643500            | 240                             | 306400                       | Fracture along the fusion line                              |
| 2176               | 30            | 463900            | 250                             | 88000                        | —>—   |

Note.  $l_{cr}$  is the crack length before corrosion testing, established by the kerosene test method;  $N_{cr}$  is the cyclic life before the origin of a crack of a set length;  $\sigma_{max}^{strength}$  is the maximum cycle stresses applied to the specimen with a crack after corrosion testing in G4 chamber for 1200 h and strengthening by HMP technology;  $N_{cr}^{strength}$  is the residual cyclic life of the specimen at a specified length crack and corrosion damages after strengthening with HMP technology; \* are the specimens that had several separate surface cracks along one fusion line.



**Figure 4.** Specimens of tee welded joints of 15KhSND steel after fatigue tests with surface fatigue cracks, strengthened by HMP after exposure in the G4 chamber for 1200 h

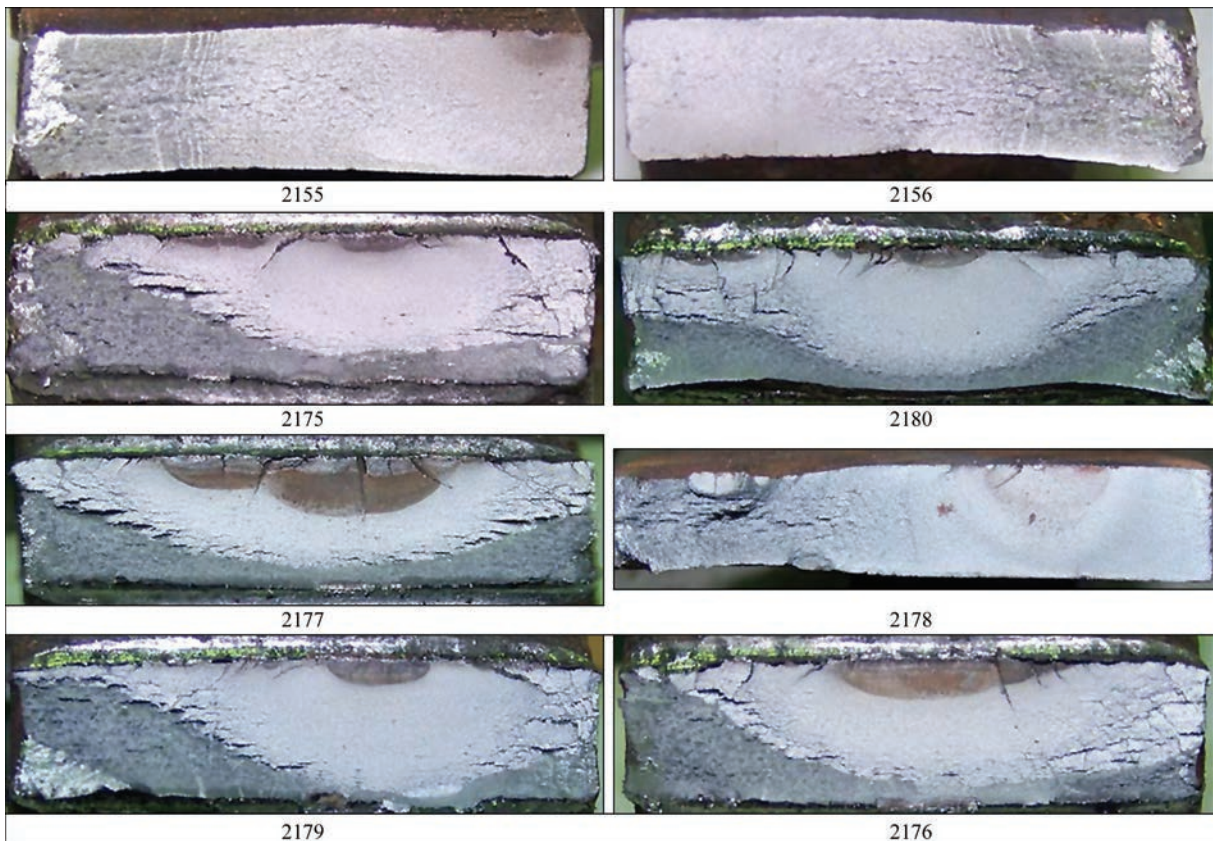


**Figure 5.** Fatigue fractures of specimens of tee welded joints of 15KhSND steel with surface fatigue cracks, strengthened by HMP after exposure in the G4 chamber for 1200 h (see Table 2)

subjected to strengthening along the fusion line (see Figures 4 and 5).

Thus, a high efficiency of applying HMP technology was established to increase the cyclic life of tee welded joints of metal structures, which, as a result of a long service under the conditions of moderate climate of the central regions of Ukraine, contain fatigue

surface cracks of up to 10 mm length and characteristic corrosion damages.

### Conclusions

1. The residual life of tee welded joints of 15KhSND steel with surface fatigue cracks and corrosion damages characteristic to metal structures after a long-

term service under the conditions of moderate climate of the central regions of Ukraine was experimentally investigated. The long-term effect of the moderate climate was modeled by exposing the joints in the G4 hydrostat at a temperature of 40 °C and at a relative air humidity of 100 % for 1200 h. It was confirmed that the residual life of the joints decreases with increasing the length of initial crack.

2. It was established that applying strengthening by HMP technology for tee welded joints with the surface fatigue cracks of up to 10 mm and corrosion damages characteristic to metal structures after a long-term service under the conditions of moderate climate of the central regions of Ukraine, increases their residual cyclic life up to 10 times. The values of residual life are within the range of experimental values scattering of joints without fatigue cracks, strengthened by HMP technology at a set level of accumulated fatigue and corrosion damages (life of  $2 \cdot 10^6$  cycles of stress changes at maximum stresses of 150 MPa and exposure in G4 hydrostat for 1200 h). It was shown that application of HMP technology to welded joints containing fatigue cracks of 20 mm length or more does not lead to increase in cyclic life and is ineffective.

1. Kudryavtsev, Y., Kleiman, J., Lugovskoy, A. et al. (2007) Rehabilitation and repair of welded elements and structures by ultrasonic peening. *Welding in the World*, 51(7–8), 47–53.

2. Vilhauer, B., Bennett, C.R., Matamoros, A.B., Rolfe, S.T. (2012) Fatigue behavior of welded coverplates treated with ultrasonic impact treatment and bolting. *Engineering Structures*, 34(1), 163–172.
3. Abston, S. (2010) The technology and applications of ultrasonic impact technology. *Australasian Welding J.*, 55, 20–21.
4. Kuhlmann, U., Dürr, A., Günther, P. et al. (2005) Verlängerung der lebensdauer von schweißkonstruktion aus höher festen baustählen durch Anwendung der UIT-technologie. *Schweißen und Schneiden*, 57(8), 384–391.
5. Knysh, V.V., Osadchuk, S.O., Solovej, S.O. et al. (2019) Procedure of accelerated corrosion testing for modeling the long-term effect of moderate climate atmosphere on welded joints. *The Paton Welding J.*, 11, 44–48.
6. Turnbull, A., Rios, E.R., Tait, R.B. et al. (1998) Improving the fatigue crack resistance of waspalyo by shot peening. *Fatigue & Fracture of Engineering Materials & Structures*, 21, 1513–1524.
7. Song, P.S., Wen, C.C. (1999) Crack closure and crack growth behavior in shot peened fatigue specimen. *Engineering Fracture Mechanics*, 63, 295–304.
8. Branko, C.M., Infante, V., Bartista, R. (2004) Fatigue behavior of the welded joints with cracks, repaired by hammer peening. *Fatigue Fract. Engng. Mater. Struct.*, 27, 785–798.
9. Farahi, G.H., Majzoobi, G.H., Hosseinzadeh, F., Harati, S.M. (2006) Experimental evaluation of the effect of residual stress field on crack growth behaviour in C(T) specimen. *Eng. Fract. Mech.*, 73, 1772–1782.
10. Knysh, V.V., Kuzmenko, A.Z., Solovej, A.S. (2009) Increase of cyclic fatigue life of tee welded joints with surface cracks. *The Paton Welding J.*, 1, 29–33.

Received 06.11.2019



**iiw**  
ASSOCIATED EVENT

## YOUNG PROFESSIONALS INTERNATIONAL CONFERENCE

### ON WELDING AND RELATED TECHNOLOGIES

# YPIC and WRTYS 2020

19-22 MAY 2020

Kyiv, UKRAINE



ypic2020.com

# PRESS MAGNETICALLY-IMPELLED ARC WELDING OF HIGH-STRENGTH STEEL TUBULAR PARTS OF HYDRAULIC CYLINDERS

V.S. Kachynskiy, S.I. Kuchuk-Yatsenko and M.P. Koval

E.O. Paton Electric Welding Institute of the NAS of Ukraine

11 Kazymyr Malevych Str., 03150, Kyiv, Ukraine. E-mail: [office@paton.kiev.ua](mailto:office@paton.kiev.ua)

Materials for carrying out works in the framework of investigating weldability of parts of hydraulic cylinders with diameters from 40 to 200 mm and a wall thickness of up to 10 mm, the results of performed metallographic examinations and mechanical properties of welded joints are presented. The basic conditions for forming welded joints of tubular parts of hydraulic cylinders were determined. The process of press magnetically-impelled arc welding of pipes of hydraulic cylinders with a diameter of up to 200 mm and a wall thickness of up to 10 mm was developed. 8 Ref., 4 Tables, 16 Figures.

*Keywords:* press magnetically-impelled arc welding, pipes for hydraulic cylinders, joint formation, welding technology

In different industries a large amount of works is performed on welding of circumferential welds of pipes and tubular parts of hydraulic cylinders with a diameter of 40–220 mm and a wall thickness from 4 to 10 mm, operating under high pressure. In this case, mainly arc welding is used.

The development of technologies and equipment for press welding in the stationary conditions would significantly improve the labour efficiency in the industry and improve the stability of joints quality. The experience gained at the E.O. Paton Electric Welding Institute of the NAS of Ukraine (PWI) in the recent decades in the field of pressure pipe welding has shown the prospect of such developments using the press magnetically impelled arc welding (PMIAB) method.

In recent decades, PMIAB technologies have been developed and successfully implemented in the manufacture of different tubular assemblies at automobile factories in Ukraine and other countries, welding pipes in the construction of greenhouse complexes and welding pipelines in the conditions of permafrost [1–6].

The purpose of recent investigations carried out at the PWI was the development of technology and equipment for PMIAB welding of pipes with a bottom

of different assortment and chemical composition of steel, with the diameter of up to 200 mm and a wall thickness of up to 10 mm, covering the most demanded assortment of tubular parts for the manufacture of cylinders (Figure 1).

The chemical composition of the investigated pipe steels is given in Table 1, the values of mechanical properties of base metal and metal of welded joint are shown in Table 2. The standard dimensions of parts to be welded included: diameter — 40–188 mm, wall thickness — 4–10 mm (32 standard dimensions).



Figure 1. Design of bottom of hydraulic cylinder (height is 35 mm)

Table 1. Chemical composition of steels, wt. %

| Steel grade     | C     | Si    | Mn   | P     | S     | Cu   | Ni   | Cr   | Mo   | Ti    | Nb    | B     | Al   |
|-----------------|-------|-------|------|-------|-------|------|------|------|------|-------|-------|-------|------|
| St52-3          | 0.18  | 0.52  | 1.35 | 0.02  | 0.03  | 0.28 | 0.24 | 0.23 | –    | –     | –     | –     | –    |
| 01Star520 (X80) | 0.159 | 0.172 | 1.19 | 0.012 | 0.006 | 0.13 | 0.04 | 0.04 | 0.03 | 0.002 | 0.002 | 0.001 | 0.03 |

V.S. Kachynskiy — <http://orcid.org/0000-0001-9695-6434>, S.I. Kuchuk-Yatsenko — <http://orcid.org/0000-0002-1166-0253>,  
M.P. Koval — <http://orcid.org/0000-0003-2066-3365>

© V.S. Kachynskiy, S.I. Kuchuk-Yatsenko and M.P. Koval, 2020

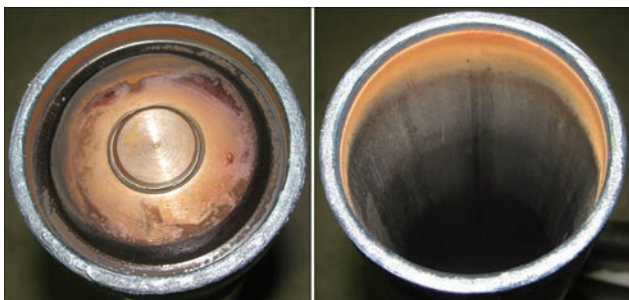
**Table 2.** Basic technological parameters of welding

| Steel grade     | Pipe diameter × wall thickness, mm | Welding time, s | Upsetting force, kN | Shortening of pipes, mm |
|-----------------|------------------------------------|-----------------|---------------------|-------------------------|
| St52-3          | 40×4                               | 6               | 40                  | 4.1                     |
| St52-3          | 60×5                               | 14              | 57                  | 5.4                     |
| St52-3          | 120×7.5                            | 37              | 257                 | 8.2                     |
| 01Star520 (X80) | 121×7                              | 35              | 250                 | 8                       |
| 01Star520 (X80) | 121×10                             | 43              | 278                 | 10                      |

All welded joints were tested in accordance with the international API standard [7], and additional bending tests were performed in accordance with the departmental procedures and standards.

Metallographic examinations were performed after etching in a 4 % HNO<sub>3</sub> solution in alcohol. The measurements of microhardness were carried out in the LECO M-400 hardness tester at a load of 10; 100 and 1000 g. Taking pictures of the structure of the welded joints was performed in the Neophot-32 optical microscope.

The PMIAB process is characterized by the fact that under the action of an external control magnetic field, the arc moves in the gap between the ends of the tubular parts to be welded. A relatively high speed of the arc movement, up to 170 m/s, allows redistributing thermal energy of the welding arc over the entire surface of the ends of parts. A relatively uniform heating of pipe ends to be welded is achieved. A welded joint is formed during compression and joint plastic deformation of ends of the parts [8]. The process of

**Figure 2.** Traces left by welding arc during heating of the outer edges of pipe**Figure 3.** Surfaces of pipe and bottom ends covered with a layer of melt metal

welding parts of hydraulic cylinders is performed in air, without the use of shielding gases.

Taking into account different conditions of heat removal from the parts, the aim of the investigations was to find the ways for control of the heating process, providing a steady movement of the welding arc across the entire cross-sectional area of the ends of pipe and bottom, achieving their uniform heating.

As a result of investigations carried out at the PWI, a method was developed, which provides a control of the movement of the arc over the entire cross-sectional area of tubular parts. The process of heating the ends is performed during movement of the welding arc along the outer edges, in the area with a higher value of a radial component of the controlled magnetic field (CMF) induction (Figure 2).

After achieving a uniform heating, which provides the necessary conditions for plastic deformation of the ends, a program change in the technological parameters of welding occurs, which leads to scanning of the welding arc on the surface of the pipe ends (Figure 3). The quality formation of welded joint of the pipe with bottom can be provided without any gas shielding under the condition that the frequency of the arc rotation at the moment before upsetting is selected so that the layer of melt metal at any point on the surface of the ends does not have a time to solidify at the time intervals when the arc passes through these regions. Then upsetting is performed.

On the basis of these investigations the system of automatic control of the process of PMIAB welding of pipe with bottom, the optimal programs for changing the basic parameters in the process of welding, and also the algorithms of their control with the use of feedbacks were developed [5]. Technologies of PMIAB welding of parts of hydraulic cylinder and welding equipment were developed. The main parameters characterizing welding modes are given in Table 2.

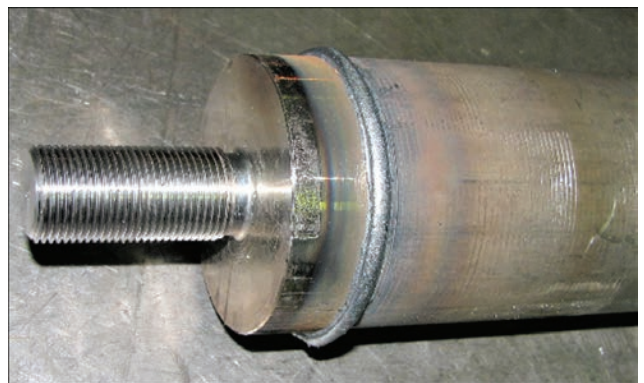
**Figure 4.** Welded joint of the pipe with bottom of 120×7.5 mm diameter



Figure 5. Results of bending tests of welded joint

High-strength steel tubular parts, operating under high-pressure are used in the manufacture of hydraulic cylinders. A photo of appearance of such welded joints is shown in Figure 4.

Mechanical tests such as tensile, bending (Figure 5) and rupture, hardness measurements and metallographic examinations were performed in accordance with the standard API 1104 [7].

Mechanical properties of welded joints of pipes are given in Table 3.

Comprehensive mechanical tests show a practical equal strength of welded joints and base metal and meet the standard requirements.

Metallographic examinations were performed on the fused end of the product of 90 mm diameter (Figure 3) at the moment before upsetting and in the welded joint of 120×7.5 mm diameter (Figure 4) of St52-3 steel. The specimens for investigations were manufactured on high speed discs using diamond pastes of different dispersion. Revealing of the structure was performed by chemical etching in a 4 %  $\text{HNO}_3$  solution in ethyl alcohol. Examinations were performed in the microscopes Neophot-32 and Poluvar at different magnifications. The hardness of the melt layer was measured in the LECO M-400 hardness tester.

Table 3. Mechanical properties of welded joints of pipes

| Steel grade | Pipe diameter x wall thickness, mm | $\sigma_r$ , MPa      |                       | $KCV_{20}$ , J/cm <sup>2</sup> |                      |
|-------------|------------------------------------|-----------------------|-----------------------|--------------------------------|----------------------|
|             |                                    | Base metal            | Welded joint          | Base metal                     | Welded joint         |
| St52-3      | 90×5                               | <u>492–513</u><br>498 | <u>480–492</u><br>486 | –                              | –                    |
| 01Star520   | 121×10                             | <u>685–708</u><br>696 | <u>630–645</u><br>638 | <u>125–168</u><br>147          | <u>60–168</u><br>114 |
| 01Star520   | 191×7                              | <u>638–665</u><br>651 | <u>618–674</u><br>656 | <u>116–154</u><br>135          | <u>87–152</u><br>119 |
| St52-3      | 120×7.5                            | <u>491–512</u><br>497 | <u>478–489</u><br>483 | –                              | –                    |

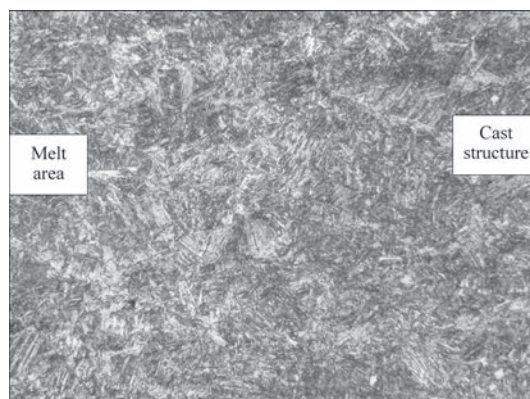
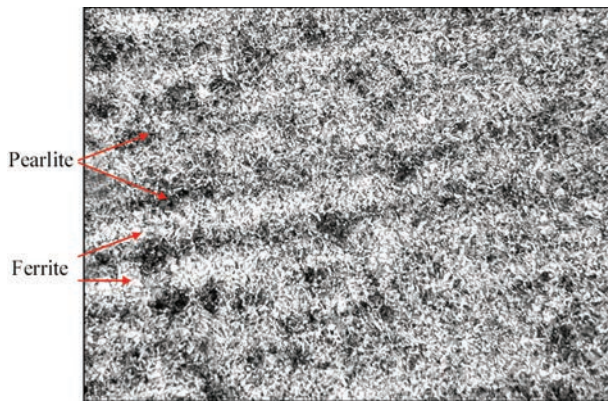


Figure 6. Microstructure ( $\times 200$ ) of cast metal and melt area

Specimen after heating without upsetting (see Figure 3). At the fused end of the specimen there is an area with a cast structure (Figure 6). The width of the area is 300–400  $\mu\text{m}$ . The structure of metal is ferrite-pearlite, ferrite is released along the crystallite boundaries. At this area, polygonal and Widmanstätten types of ferrites were found and along the crystallite boundaries polyhedral one (in a small amount) was detected. The hardness at this area is  $HV1-2240$  MPa;  $HV1-1850$  MPa;  $HV1-2280$  MPa;  $HV1-2060$  MPa. At the overheating area, the structure consists of upper and lower bainites with a hardness of  $HV1-2830$  MPa;  $HV1-3090$  MPa;  $HV1-3360$  MPa and  $HV1-3480$  MPa. The width of this area is 2000  $\mu\text{m}$ , then in the structure pearlite appears, the amount of bainite is reduced, the hardness decreases to  $HV1-2490$  MPa;  $HV1-2450$  MPa.

At the area of complete recrystallization, the structure is fine, consisting of ferrite, pearlite and a small amount of bainite. In the structure, the traces with bands appear (Figure 7), which are absent in the overheating area (Figure 8). The hardness is  $HV1-2060-2240$  MPa.

The area of incomplete recrystallization after upsetting has a fine-grained ferrite-pearlite structure (grain number 9 according to GOST 5639–82), where the bands of ferrite and pearlite are alternated (Figure 7). The hardness of metal at the area is  $HV1-$



**Figure 7.** Microstructure ( $\times 200$ ) of the area of full and partial recrystallization on the bottom side

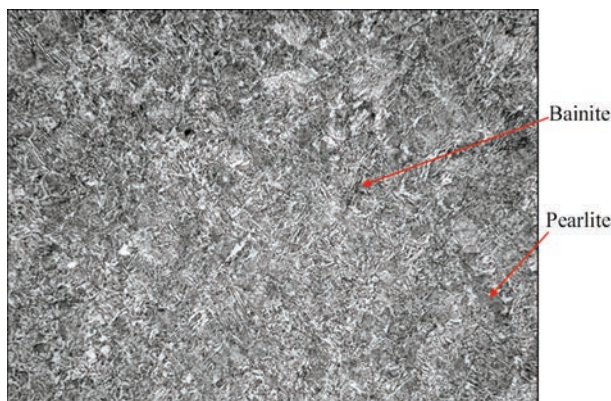


**Figure 8.** Microstructure ( $\times 200$ ) of the overheating area on the bottom side

1880–1960 MPa (ferrite) and  $HV1$ –2060–2240 MPa (pearlite).

The base metal has a ferrite-pearlite structure in the form of bands with a ferrite grain number Nos 7–8 according to GOST 5639–82 and a hardness of  $HV1$ –1870–1760 MPa. The width of the heat-affected-zone is 4000  $\mu\text{m}$ .

Macrosection of welded joint with a diameter of 120 $\times$ 7.5 mm is shown in Figure 9. The joint line represents a discontinuous white band of up to 40  $\mu\text{m}$  thickness in the central area of the welded joint and extends up to 80  $\mu\text{m}$  to the edges of the specimen. The structure of the joint line is ferrite with the hardness of

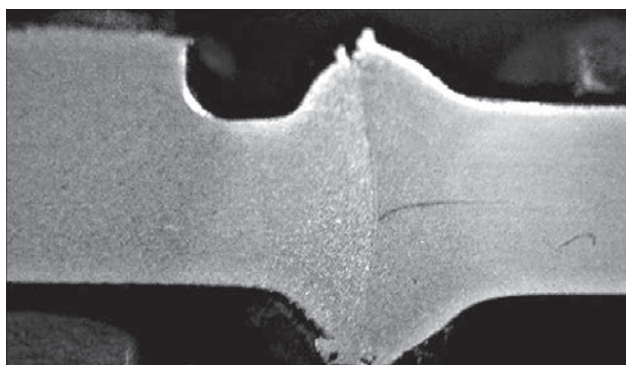


**Figure 9.** Macrosection of welded joint of the pipe and bottom of 120 $\times$ 7.5 mm diameter



**Figure 10.** Microstructure ( $\times 200$ ) of welded joint

$HV1$ –1650–1810 MPa. From the distribution of hardness it is seen that the joint has a slight increase in the hardness of ferrite band to  $HV1$ –1800 MPa, which is higher than the hardness of base metal of tubular parts. The distribution of hardness in the butt indicates the absence of significant changes in strength at the main areas of the weld. The values of hardness on the joint line are also close to the similar values of base metal. During PMIAB, the structure of metal in the HAZ is more homogeneous. No defects on the joint line were detected (Figure 10).

The structure of the overheating area on the side of the lid has small regions of pearlite and ferrite of different modifications, mainly ferrite with an ordered second phase. In addition, it has polyhedral ferrite, Widmanstätten ferrite and polygonal ferrite in the form of fragments of ferrite bands along the borders of former austenitic grains.

The hardness of the metal in this area is  $HV1$ –1830–2160 MPa (Figure 10).

With distance from the joint line, the structure is refined, the number of polygonal and polyhedral ferrite increases.

At the area of complete recrystallization, the structure is fine-grained (grain number 10–11 according to GOST 5639–82) ferrite-pearlite.

The base metal has a ferrite-pearlite structure with a grain number No.8 and the hardness of  $HV1$ –1560–1760 MPa. The HAZ width is approximately 6000  $\mu\text{m}$ .

The overheating area on the side of the pipe has almost the same structure as the area on the side of the lid (Figures 11, 12). The difference is that a predominant amount of ferrite with a disordered second phase and structure on the overheating area is finer. The hardness of metal in the overheating area is  $HV1$ –1780–2060 MPa. With distance from the joint line, the structure is refined. The width of the overheating area is 2700  $\mu\text{m}$ . The width of the overheating area is

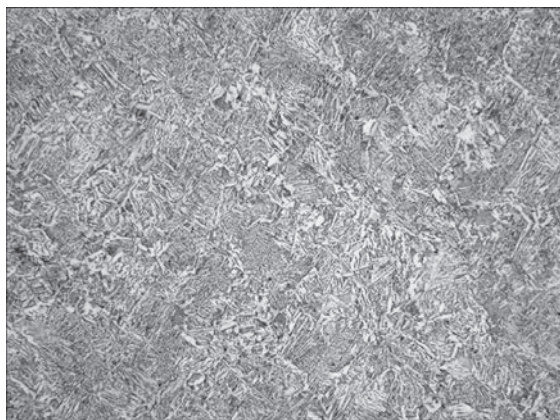


**Figure 11.** Microstructure ( $\times 200$ ) of the overheating area on the bottom side



**Figure 14.** Microstructure ( $\times 200$ ) of base metal of the pipe



**Figure 12.** Microstructure ( $\times 200$ ) of the overheating area on the pipe side



**Figure 15.** Hydraulic cylinders ready for operation



**Figure 13.** Microstructure ( $\times 200$ ) of the area of complete and partial recrystallization on the pipe side

smaller after upsetting and is  $2700\ \mu\text{m}$  as compared to  $3500\ \mu\text{m}$  after heating without upsetting.

The structure of the area of complete recrystallization of ferrite is pearlite fine-grained with the predominance of a ferrite component (Figure 12). Traces of bands are visible at the area of incomplete recrystallization. The bands appear in the area of partial recrystallization. The structure at this area is ferrite-pearlite, consisting of alternating bands of ferrite and pearlite. The HAZ width is approximately  $5000\ \mu\text{m}$ .



**Figure 16.** Welding machine MD-205

The base metal represents a fine-grained (grain number 10–11) ferrite-pearlite structure (Figure 13) with a hardness of  $HV1-1660-1990\ \text{MPa}$ .

Defects in the HAZ are not observed. The hardness of the pearlite band is  $HV1-2050\ \text{MPa}$ ,  $HV1-1990\ \text{MPa}$ ,  $HV1-2050\ \text{MPa}$ . The hardness near the pearlite ferrite mixture is  $HV1-1560-1600\ \text{MPa}$ .

**Table 4.** Technical specifications of the machine for PMIAB welding of hydraulic cylinders

| Machine index | Diameter of welded pipes, mm | Wall thickness, mm | Efficiency, butts/h | Power consumption, kW | Weight, kg |
|---------------|------------------------------|--------------------|---------------------|-----------------------|------------|
| MD-205        | 30–200                       | 3–10               | 80                  | 40                    | 1500       |

For PMIAB welding of tubular parts of hydraulic cylinders, the MD-205 machine was designed, which provides an industrial welding in stationary conditions (Table 4). Using this technology, more than 17,000 parts of hydraulic cylinders with diameters from 42 to 178 mm were welded (Figure 16).

The MD-205 machine (Figure 15) is designed for press welding of tubular parts of different purpose and consists of:

- welding head;
- hydraulic pumping station;
- control cabinet with portable control panel;
- source for power of welding arc.

MD-205 is a tong-type welding machine, which is characterized by a separate clamping of pipes to be welded. In terms of design, the machine is capable of loading and unloading welded pipes on the side.

## Conclusions

1. The optimal conditions were determined which allow a steady movement of the arc in a narrow gap to achieve a relatively uniform heating of welded ends of the pipes.

2. A control method was developed that allows moving the arc over the entire welding cross-sectional area of pipes and forming a uniformly distributed melt on it.

3. The basic conditions for forming welded joint of tubular parts of hydraulic cylinders were determined.

4. PMIAB process was developed that allows welding pipes with a wall thickness, exceeding the sizes of active spots of the arc column.

5. Technologies of PMIAB welding of tubular parts of high-strength steels were developed in the production of hydraulic cylinders with a diameter of up to 200 mm and a wall thickness of up to 10 mm.

1. Ganovski, F.J. (1974) The magnetarc welding process. *Welding and Metal Fabrication*, June, 206–213.
2. Edson, D.A. (1982) Magnetically impelled arc faying surface welding of thick wall tubes. *IW, IM-726–82*.
3. Takagi, K., Aracida, F. (1982) Magnetically impelled arc butt welding of gas pipeline. *Metal Construction*, **20**, 542–548.
4. Hiller, F., Schmidt, M., Breiksch, J. (2003) Use of the magnetarc welding process in the production of truck cab suspension systems. *Thyssen Krupp Techforum*, 40–43.
5. Kuchuk-Yatsenko, S.I., Kachinskiy, V.S., Ignatenko, Yu.V. (2010) Magnetically-impelled arc butt welding of automobile parts. *Australasian Welding J.*, **55**, Second Quarter.
6. Kachinskiy, V.S., Kuchuk-Yatsenko, S.I., Ignatenko, Yu.V., Koval, M.P. (2010) Magnetically-impelled arc butt welding of pipes of steel X70. *Ibid*.
7. API STANDARD 1104 (2013) *Welding of pipelines and related facilities*. American Petroleum Institute.
8. Kachinskiy, V.S., Krivenko, V.G., Ignatenko, Yu.V. (2002) Magnetically impelled arc butt welding of hollow and solid parts. Doc. IW III-1208–02. *Welding in the World*, 46(7/8), 49–56.

Received 06.11.2019

## XII International Trade Fair

# KYIV TECHNICAL FAIRS





**INTERNATIONAL  
EXHIBITION CENTRE**  
15 Brovarskyi Ave., Kyiv, Ukraine  
Tel.: +38 044 201 11 58, 201 11 65, 201 11 56  
e-mail: alexk@iec-expo.com.ua,  
plast@iec-expo.com.ua  
www.iec-expo.com.ua, www.tech-expo.com.ua

## March 31 – April 3, 2020

General Information Partner:



Exclusive Media Partner:



Technical partner:



# ELECTRON BEAM WELDING WITH PROGRAMMING OF BEAM POWER DENSITY DISTRIBUTION

V.V. Skryabinskyi, V.M. Nesterenkov and M.O. Rusynyk

E.O. Paton Electric Welding Institute of the NAS of Ukraine

11 Kazymyr Malevych Str., 03150, Kyiv, Ukraine. E-mail: office@paton.kiev.ua

In the existing models of electron beam welding process, the shape and size of penetration zone are determined both by energy parameters and shape of the heat source. Effective control of electron beam power density distribution and, therefore, of the heat source shape is possible by using discrete scans. A procedure and computer program were developed to calculate the power density distribution at discrete scanning of the electron beam, taking into account the coordinates of scan points, relative time of its dwelling in the points and scanning frequency. Joint application of the computer program for calculation of beam power density distribution together with the mathematical model of electron beam welding allows obtaining the set shape and dimensions of the penetration zone. The results of calculation of welding modes and cross-sections of welds with parallel side walls and a large radius of the root rounding at partial penetration of stainless steel samples are presented. The method of calculation of electron beam welding parameters and cross-section of the joint of dissimilar alloys are also given. 11 Ref., 7 Figures.

*Keywords:* electron beam welding, beam power density, computer-aided design of scans, shape of penetration zone, welding of dissimilar alloys

In electron beam welding (EBW) accelerating voltage, beam current, welding speed and beam focal spot position relative to the surface of the item being welded are the main parameters of the mode. In case of application of beam oscillations, the pattern, amplitude and frequency of scanning are added to them. Simultaneous accounting for EBW parameters, in order to produce high quality joints is a complicated but urgent task.

The objective of this work is demonstration of the possibility of controlling the vapour-gas channel shape, and, accordingly, shape of penetration zone, using computer design of beam scan patterns with simultaneous application of EBW mathematical model.

Intensity of electron beam impact in any point of the treated surface is proportional to its power density. Many researchers call the ability to change the electron beam power density distribution the main effect of scanning (here and furtheron, we mean not the instantaneous, but averaged over the scanning period beam power density). Here, the shape of vapour-gas channel, its resistance to external disturbances, penetration zone shape and, accordingly, the probability of root defect formation are changed [1–4].

The distribution of electron beam power density and, hence, the heat source shape in EBW, can be efficiently controlled using digital scanning systems [5, 6]. In such systems, the electron beam moves discretely by a given matrix of points that make up the scanning pattern. The coordinates of the pattern points and

relative time of beam dwelling in these points over one period of scanning are saved in a read only memory (ROM). The control system converts the digital scan code into electric signals and feeds them to the electron beam gun deflection coils.

Assessment of electron beam power density distribution is a rather complex task, even when using the simplest scan patterns (circle, semicircle, etc.). Here, alongside the pattern, it is also necessary to take into account the degree of beam focusing and scan amplitude along axes  $X$  and  $Y$ . When using discrete scans, the calculation formula also includes the coordinates of beam dwelling points and relative duration of its dwelling. In connection with the fact that beam transition from one point to another one is performed at a final speed (that is determined by the total inertia of the deflection system), beam power distribution density will be determined also by scan frequency [7].

Assuming the density distribution in a static beam close to a Gaussian one, the relative density of the scanning electron beam power in  $i$ -th point  $q(x_i, y_i)$  can be determined as the sum of impact  $N$  of normal point and  $N$  linear sources:

$$q(x_i, y_i) = \sum_{j=1}^N \exp\left(-\frac{r_{ij}^2}{2r_e^2}\right) t_j + A(f) = \sum_{j=1}^N \exp\left(-\frac{r_{ik}^2}{2r_e^2}\right) t_{j(j-1)}, \quad (1)$$

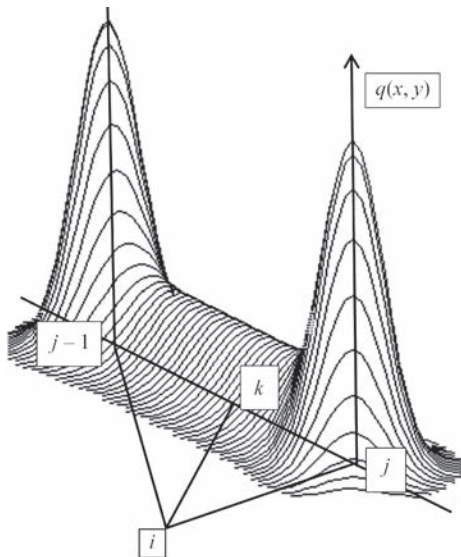


**Figure 1.** Scheme for calculation of electron beam power density distribution taking into account the scanning frequency

where  $A(f)$  is the ratio of the intensity of the point and linear sources, dependent on scan frequency ( $f$ );  $N$  is the number of scan points;  $r_e$  is the effective beam radius;  $r_{ij}$  is the distance from calculated point  $i$  to  $j$ -th point of the scan;  $r_{ik}$  is the distance from calculated point  $i$  to the linear source;  $t_j$  is the relative time of the beam dwelling in the  $j$ -th point of the scan;  $t_{j(j-1)}$  is the time of the beam transition from  $j-1$  point into point  $j$ .

The calculation schematic is shown in Figure 1. Function  $A(f)$  is calculated by numerical methods, taking into account the total inertia of beam deflection system. In our case system inertia depends on the parameters of deflection coils, scan generator and deflecting current amplifiers.

Computer programs for scan design and operative control of beam power density distribution at EBW allow performing highly accurate calculations

and displaying and/or saving the obtained results in the ROM [7, 8]. When designing the scans, the user assigns coordinates  $N$  of discrete beam positions, as well as the time of its dwelling in each of the selected positions (Figure 2).

At the same time, the computer screen displays the shape of the heat source (horizontal projection and 3D image). There is a capability of freely dragging the scan points over the screen or loading from ROM and editing the already existing patterns. It is important to note that during the design stage the user not only places the scan pattern points and assigns the relative time of beam dwelling, but he can also check the impact of the change of focusing, amplitude and frequency of scanning on the resultant distribution of beam power.

Each of these parameters has its specific impact on the result of calculation by formula (1) and, therefore, on EBW process. In order to clarify this impact, a computer program was used to conduct calculations of the given distributions of beam power at alternate change of scan amplitude ( $D$ ), degree of focusing (beam effective radius  $r_e$ ) and beam dwell time ( $T$ ) in the scan points (Figure 3).

Calculations were conducted for a circular scan pattern. Increase of scan amplitude leads to proportional increase of the width of beam impact zone at an abrupt lowering of its intensity and formation of a depression in the central part of the graph. Beam defocusing ( $r_e$  increase) also increases the width of the impact zone, leveling the central depression in the graph. Change of the time of beam dwelling in the scan pattern points allows controlling in a broad range the distribution of power density, practically not affecting its width. So, the heat input in the weld central part can be changed two times, by shifting the points with doubled beam dwell time from the central to side parts of the weld pool as shown in Figure 4.

Where and how can the computer control of electron beam power density distribution be used? Information on the heat source shape may be needed for further calculations, related to mathematical modeling of EBW process. For instance, control of the penetration zone shape and dimensions has always been an urgent task, in terms of both EBW theory and practice. A number of existing models of EBW process not only allow assessing the weld depth and width, but also calculate the penetration zone shape. In them the capability of regulation of energy distribution in the heat source during calculations is not envisaged, and the main conclusions usually concern the degree of conformity of the calculated and experimental data [9–11].

Programming of the distribution of beam power density allows changing the heat source shape in a broad range, and, thus, it is a convenient tool for con-

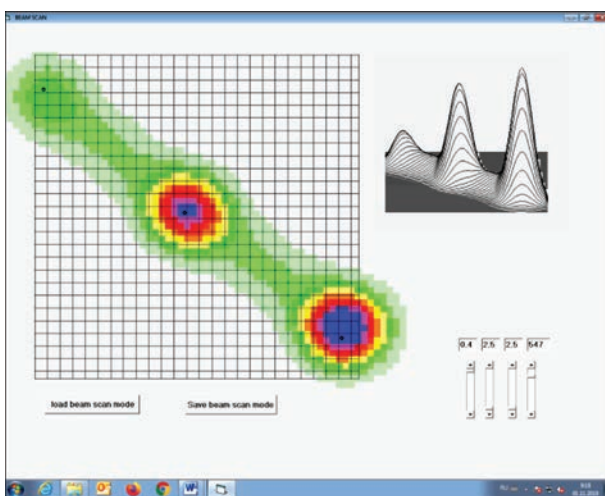


**Figure 2.** Heat source shape (horizontal projection and 3D image) when designing the scan pattern on the computer screen. Scan parameters; point number — 3; relative time of beam dwelling in points 1, 2, 3; frequency — 550 Hz

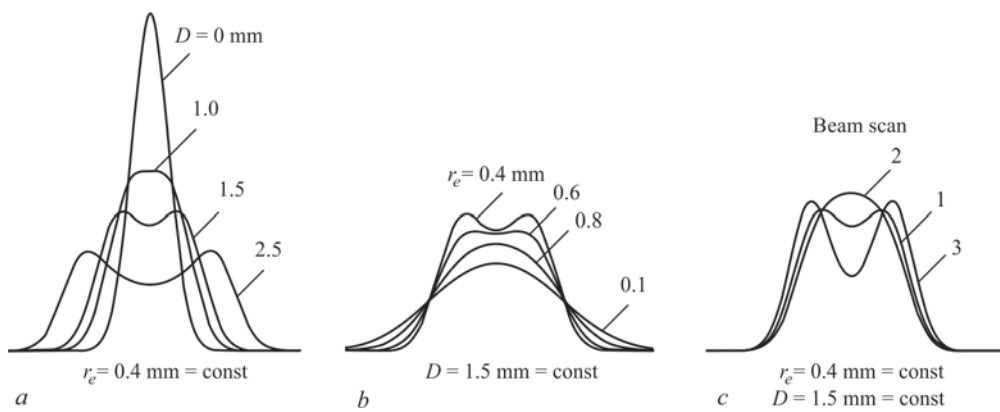


**Figure 3.** Distribution of electron beam power density for a circular scan at the change of: circular scan amplitude (a); beam focusing (b); relative time of beam dwelling in scan pattern points (c). Beam scans for calculation of the curves in Figure 3 are shown in Figure 4

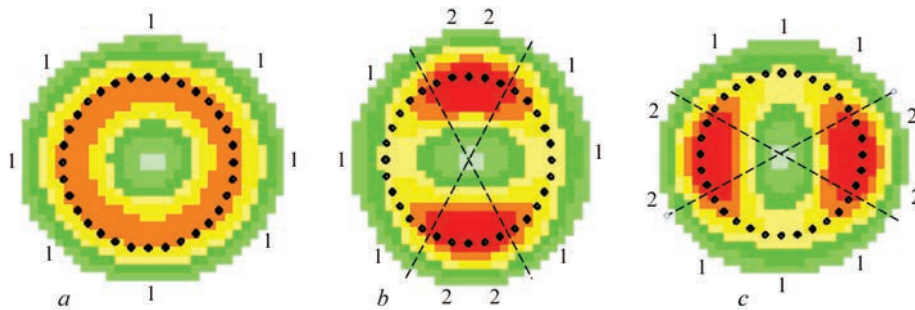


**Figure 4.** Circular patterns of the electron beam (32 points) with different relative time of beam dwelling in the scan pattern points. Numbers in the figure indicate the relative time of beam dwelling in the points: a — beam scan 1; b — 2; c — 3

trolling the penetration zone shape. Of practical interest was introduction of a variable (in our case beam power density distribution) into the mathematical model, changing which allows controlling the penetration zone shape.

In this work the mathematical model presented in [3] was selected for prediction of the penetration zone shape. In it the law of energy conservation is used as a base for deriving an equation for an element of the penetration channel surface, which describes the shape of the channel front wall in a cylindrical system of coordinates for any distribution of electron beam power density:

$$\frac{dr}{dz} = \frac{\rho V_w G \cos \varphi - q_{h,r}}{\eta}, \quad (2)$$

where  $\rho$  is the specific weight of metal;  $V_w$  is the welding speed;  $G$  is the heat content in a unit of metal mass;  $q_{h,r}$  — heat removal power density;  $\eta$  is the effective efficiency of the process;  $q(r, \varphi)$  is the beam power density distribution.

Practical verification of the method to control the penetration zone formation was performed as follows. The computer program for calculation of the distribution of electron beam power density by formula (1) was complemented by the equation of penetration channel (2) and the image of the channel front wall was displayed. The penetration zone shape was calculated for EBW of stainless steel with partial pene-

tration in the following mode: accelerating voltage of 60 V; beam current of 170 A; welding speed of 10 m/s; discrete circular scan of the beam (point number  $N = 32$ ) with 1.5 mm amplitude, 500 Hz frequency and uniform heat input along the beam path. Considering the relatively low heat conductivity of the material, it was decided to ignore the losses for heat removal from the front wall of the penetration channel. Scan patterns, distribution of beam power density, calculated and experimental shapes of the penetration zone are shown in Figures 5, 6.

The above-given mode was used for welding a test sample from stainless steel and macrosection 1 was prepared (Figure 6, b). Calculated and experimental geometrical characteristics of the penetration zone differed only slightly. The weld width was about 2.0 mm at 24 mm penetration depth. The weld root was sharp. It is known that with such a shape of the penetration zone, weld formation is often accompanied by root defects in the form of voids unfilled by metal.

Energy distribution in the heated spot was changed, increasing the relative time of the beam dwelling in the points of the circular scan pattern, in the side parts of the weld pool. The number of points, their coordinates and other parameters of EBW mode remained unchanged. At each change of the dwell time (as of any other parameter) the computer program reflected the respective changes of beam power density distribution and penetration zone shape. After a certain

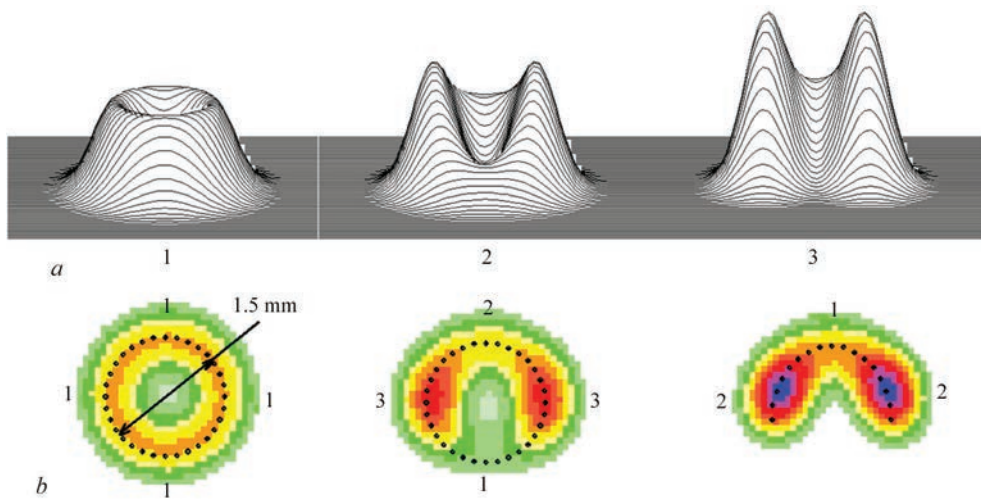


**Figure 5.** Distribution of electron beam power (*a*) and scan pattern (*b*) at EBW of stainless steel (for description of 1–3 see the text)

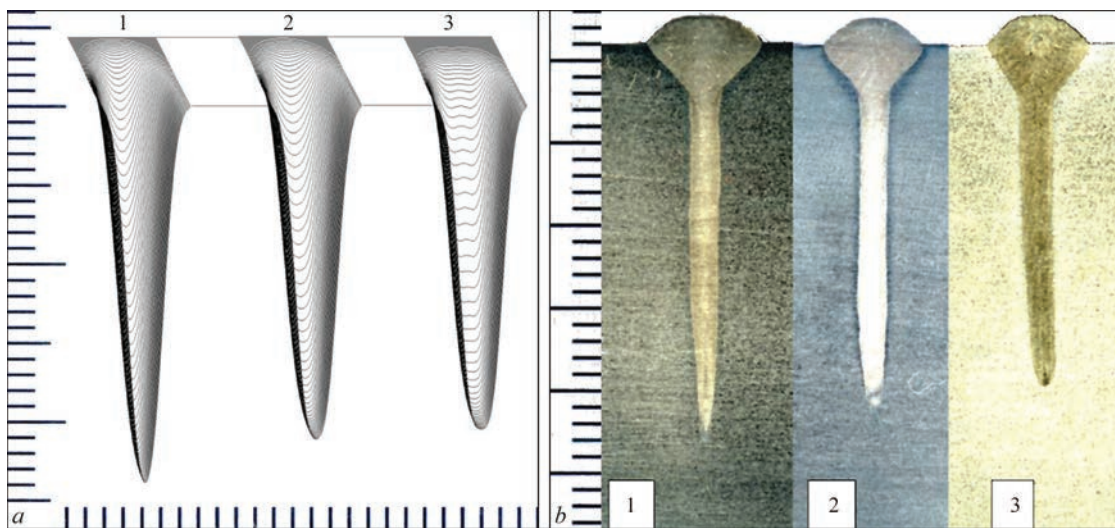


**Figure 6.** Calculated shape of penetration channel front wall (*a*) and transverse sections (*b*) at EBW of stainless steel (for description of 1–3 see the text)

shifting of heating from weld axis to weld pool side parts, we increased the rounding radius of the weld root approximately two times. The penetration depth here decreased from 24 to 22 mm (see Figure 6, *a* — 2). Beam scan parameters were stored in the ROM.

Similarly, a computer program was used to design the electron beam scan pattern in the form of a semi-circle. That is, first the beam dwell points were placed at equal distance from each other in the selected scan pattern (in our case, along an arc of a circle with beam reciprocal movement) on the screen. Then, EBW mode parameters, characteristics of the material being welded were entered into the program, and a computer image of the penetration zone shape was shown on the screen. Similar to the previous case, gradually increasing the relative time of beam dwelling in the side parts of the scan pattern, we tried to achieve a maximum increase of the rounding radius in the weld root (see Figure 6, *a*, — 3). EBW mode, including the designed beam scans, was used in EBW of stainless

steel vacuum chambers. Ultrasonic testing of welded joints showed absence of lacks-of-fusion or root defects along the entire weld length.

Computer design of electron beam scans can be useful at EBW of dissimilar metals. A usual technique in welding dissimilar metals and alloys is shifting the axially symmetrical heated spot towards the more refractory metal. The value of this displacement is either calculated, or determined experimentally. Thus, the probability of formation of lacks-of-fusion in the weld root part is reduced.

In EBW with programming of beam power density, it is necessary to increase the heat input into the refractory metal, while controlling the scan parameters. Thermo-physical calculations are based on the fact that the ratio of powers of the beam which falls on the edges should be proportional to the ratio of the quantity of heat, required for melting a unit of volume of each metal. Part of electron beam power consumed in heating metal 1, can be calculated by the following formula:

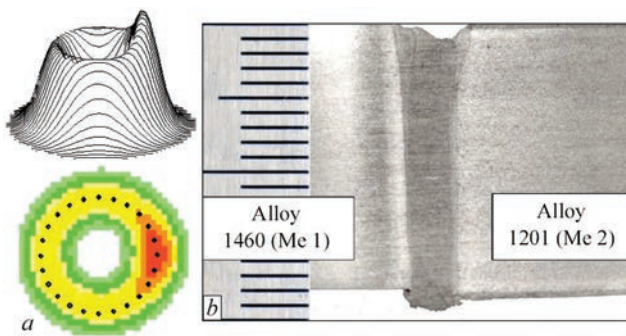


**Figure 7.** Scan pattern with electron beam power density distribution (a) and weld cross-section (b) at EBW of alloys 1460 and 1201

$$Q_{Me1} = 0.24\eta I_b U_{acc} \iint_{Me1} q(x, y) dx dy, \quad (3)$$

where  $\eta$  is the effective efficiency of the process;  $I_b$  is the beam current;  $U_{acc}$  is the accelerating voltage;  $Me1$  is the area of beam impact, which falls on metal 1;  $q(x, y)$  is the distribution of beam power density.

Beam power for metal 2 is calculated similarly. Thus, controlling the power density distribution between the different areas of beam impact, we can create the conditions for formation of a symmetrical shape of the penetration zone.

The method of EBW of dissimilar alloys with regulation of the heat input was realized in welding samples from aluminium alloys 1201 (Al–Cu alloying system) and 1460 (Al–Cu–Li alloying system) 18 mm thick. Thermophysical calculation showed that for simultaneous melting of equal amounts of metal of these alloys it is necessary to direct approximately 55 % of electron beam power to the edge of alloy 1201 and approximately 45 % of power to alloy 1460. Welding was performed with circular scanning of the beam with 2.5 mm amplitude. Selection of beam scan parameters to provide the required shifting of beam power towards alloy 1201 was conducted using a computer program. Calculations by formula (3) were easy to perform, so that the information on electron beam power density  $q(x, y)$  is written in the form of a two-dimensional file in the program, which is not difficult to integrate (sum up) for any area.

Welding was performed using accelerating voltage of 30 kV and beam current of 350 mA at the speed of 11 mm/s. Beam power density distribution and penetration zone cross-section are shown in Figure 7.

The weld side walls are practically parallel, and X-ray spectral analysis of different areas of the welded joint showed that the alloying element content in

the weld metal fluctuates around the arithmetic mean of their content in the alloys being welded. This is indicative of the fact that at surface melting both the butt edges were equally involved in weld formation.

## Conclusions

1. Computer design of beam scans with simultaneous application of EBW mathematical model enables controlling the shape of the vapour-gas channel, and, hence, the penetration zone shape.
2. Controlling the distribution of beam power density allows welding dissimilar metals and alloys with formation of a symmetrical penetration zone.

1. Ryzhkov, F.N., Suvorin, V.Ya. (1971) Technological features of vacuum welding by electron beam oscillating across the weld. *Avtomatich. Svarka*, **1**, 16–21 [in Russian].
2. Nesterenkov, V.M., Kravchuk, L.A. (1981) Selection of parameters of beam rotation around the circumference and their influence on weld geometry in electron beam welding. *Ibid.*, **10**, 25–28 [in Russian].
3. Nazarenko, O.K., Kaydalov, A.A., Kovbasenko, S.M. (1987) *Electron beam welding*. Ed. by B.E. Paton. Kiev, Naukova Dumka [in Russian].
4. Varushkin, S.V., Belenky, V.Ya., Zyryanov, N.A., Kylosov, A.A. (2017) Oscillation of electron beam as a means of improvement of weld root formation and facilitation of through penetration in electron beam welding. *Mashinostroenie, Materialovedenie*, **19(2)**, 151–159 [in Russian].
5. Lankin, Yu.N., Bondarev, A.A., Bajshtruk, E.N., Skryabinsky, V.V. (1985) Control of density distribution of electron beam power over its section. *Avtomatich. Svarka*, **6**, 12–15 [in Russian].
6. Lankin, Yu.N., Bondarev, A.A., Dovgodko, E.I., Diachenko, V.A. (2009) Control system for beam scanning in electron beam welding. *The Paton Welding J.*, **9**, 13–16.
7. Skryabinsky, V.V. (1994) *Development of technology of electron beam welding of high-strength aluminium alloys 1570 and 1460 with control of density distribution of beam power*: Syn. of Thesis for Cand. of Techn. Sci. Degree. Kyiv, PWI [in Ukrainian].
8. Lankin, Yu.N., Soloviov, V.G., Semikhin, V.F. et al. (2017) Computer system of graphic design of scanning and modeling of final distribution of electron beam current density. In: *Proc. of 8th Int. Conf. on Beam Technologies in Welding and Materials Processing (11–15 September, 2017, Odessa, Ukraine)*, 59–60.
9. Zhang Hong, Men Zhengxing, Li Jiukai et al. (2018) Numerical simulation of the electron beam welding and post welding heat treatment coupling process. *High Temp. Mater. Proc.*, **37(9–10)**, 793–800.
10. Cerveraa, M., Dialamia, N., Wub, B. et al. (2016) Numerical modeling of the electron beam welding and its experimental validation. *Finite Elements in Analysis and Design*, **121(11)**, 118–133.
11. Lastovirya, V.N. (2008) Principles of control of penetration shape in technological process of electron beam welding. *Mashinostroenie i Inzhenernoe Obrazovanie*, **3**, 12–17 [in Russian].

Received 07.11.2019

# IMPROVEMENT OF THE EFFECTIVENESS OF LASER WELDING PROCESSES BY RECIPROCATING MOVEMENT OF THE FOCUS\*

V.Yu. Khaskin<sup>2</sup>, V.M. Korzhyk<sup>1,2</sup>, Ch. Dong<sup>2</sup> and E.V. Illyashenko<sup>1</sup>

<sup>1</sup>E.O. Paton Electric Welding Institute of the NAS of Ukraine

11 Kazymyr Malevych Str., 03150, Kyiv, Ukraine. E-mail: office@paton.kiev.ua

<sup>2</sup>Guangdong Institute of Welding (China-Ukraine E.O. Paton Institute of Welding)

363 Chiansin Str., 510650, Guangzhou, Tianhe. E-mail: wuby@gwi.gd.cn

The work is devoted to evaluation of the impact of lens focus scanning along the laser radiation axis in laser and laser-arc welding on welding-technological properties of the processes and physicomachanical characteristics of weld metal in joints of low-alloyed and high-alloyed steels. It is noted that the effectiveness of welding processes here can be increased by optimization of frequency and amplitude of focus scanning. 12 Ref., 2 Tables, 9 Figures.

*Key words:* laser welding, hybrid laser-MIG welding, carbon steel, stainless steel, technological experiments, energy input

One of the main disadvantages of technological processes using laser radiation is their low efficiency (as a rule, not more than 60 %) [1]. This is associated both with a relatively low absorption coefficient of radiation by metals (about 10–40 %), as well as with a small length of its caustic neck (about 0.2–2.0 mm) [2]. Therefore, in order to increase the efficiency of such processes as welding and cutting using laser radiation, it is reasonable to increase the absorption coefficient by heating the treated surface and elongation of the radiation caustic neck. These effects can be achieved by applying a vertical reciprocating focus scanning with specific amplitudes and frequencies. Such an approach can be the basis for innovative industrial developments that can significantly save laser power.

In the manufacture of modern lightweight structures used in different fields of engineering, steels and alloys are often used, characterized by increased strength. Thus, for example, in the manufacture of fragments of hulls of large passenger liners and cargo ships, high-strength and corrosion-resistant steels are used; in the manufacture of similar hull structures of small-displacement ships, high-strength aluminum alloys can be used. At the same time, a great popularity was gained by lightweight honeycomb structures welded in slot welds using laser radiation [3].

As far as for the formation of high-quality welded joints it is necessary to achieve the formation of upper and lower reinforcements of the weld, the use of appropriate filler material is required, most often in the form of a solid wire. As investigations showed, to reduce the consumption of laser energy, it is advisable that such wire was fed with its simultaneous melting by an electric arc [4]. Moreover, the effect between the arc and consumable electrode is not limited to input of additional heat to the weld pool from the molten electrode wire. When interacting with laser radiation (primarily with ionized vapor arising above the vapor-gas channel under the effect of radiation), the electric arc is constricted, falls into the formed vapor-gas channel and complements the laser energy in a hybrid laser-arc process [5]. The so-called binding of the arc to the focus of laser radiation occurs, which provides the well-known advantages of hybrid welding.

However, while using laser and laser-arc (laser-MIG) welding to produce butt, fillet and tee joints, a number of characteristic defects may occur:

- defects associated with the formation of welds, which mainly consist in the formation of shrinkage cavities and undercuts on the both sides of the reinforcement bead (Figure 1);
- formation of inner pores (Figure 2);

\*Based on the materials of the report presented at the International Conference «Beam Technologies in Welding and Materials Processing», September 9–13, 2019, Odessa.

V.M. Korzhyk — <http://orcid.org/0000-0001-9106-8593>

© V.Yu. Khaskin, V.M. Korzhyk, Ch. Dong and E.V. Illyashenko, 2020

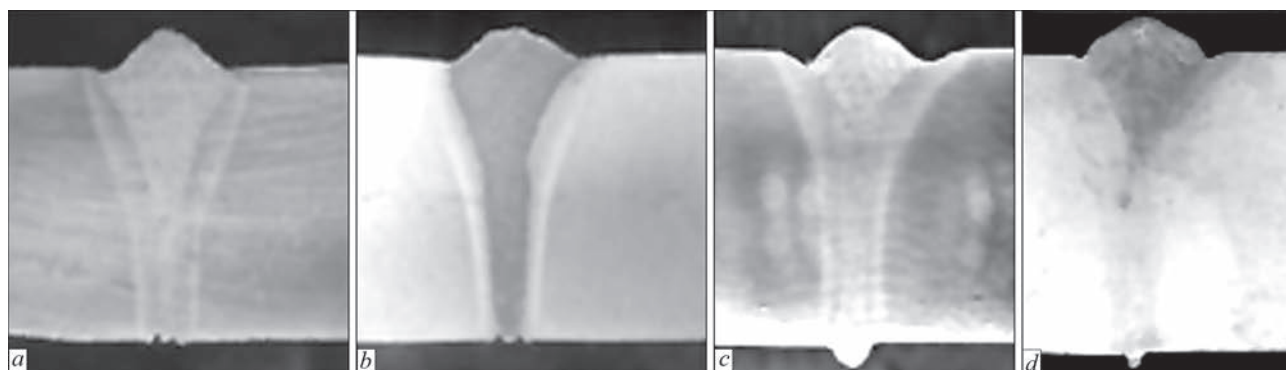


**Figure 1.** Typical defects in the formation of butt joints of high-strength steel DOMEX 390 XP ( $\delta = 10$  mm) during hybrid laser-MIG welding [6]: concavity of the weld root (*a, b*), undercuts in the upper part (*a-d*)

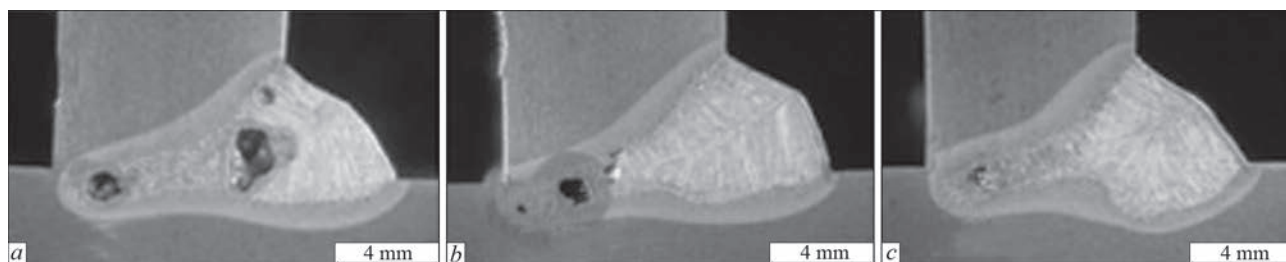


**Figure 2.** Formation of inner pores in tee joints during hybrid laser-MIG welding of high-strength AN36 steel with OK Aristorod 12.50 electrode wire (1.2 mm in diameter) using fiber laser radiation: *a, b* — power 8.0; *c* — 10.0 kW [7]

- heterogeneity of alloying the weld metal with electrode or filler wire over the depth of the weld pool (Figure 3);

- formation of cracks both during laser or laser-arc welding (Figure 4), and during the further operation of welded joints, low values of cyclic fatigue tests (alternating cyclic loads) (Figure 5).



**Figure 3.** Absence of a uniform distribution of the electrode wire metal along the weld depth during laser-MIG welding of steels of large (over 8 mm) thicknesses on the example of welding SSAB Domex 420MS steel (standard EN 10149-2) [8]

Therefore, the aim of this work is to create a fundamentally new universal approach to eliminating the characteristic defects of laser and laser-arc welding, which at the same time allows increasing the process efficiency, reducing its energy input and achieving saving of laser energy.

In the framework of the existing approach to laser and laser-arc welding, the abovementioned defects can be eliminated by different methods, the simplest of which is the selection of mode parameters. However, in most cases, when using the currently existing commercially available equipment for laser and laser-arc welding (for example, laser-MIG heads manufactured by Fronius and Cloos Companies [10]), solving the problem of producing high-quality welded joints of steels and alloys is difficult. The disadvantages of the technological scheme of the process realized by such equipment include the inability to control the

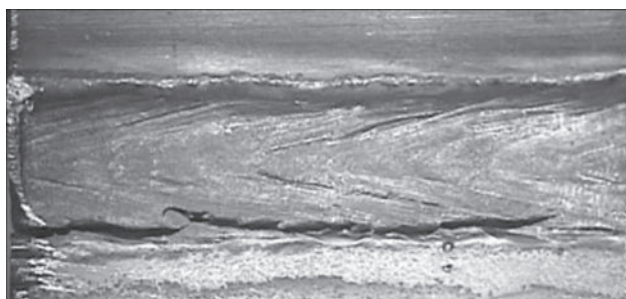


**Figure 4.** Typical geometry of a longitudinal crack on the surface of a butt joint of SS2333 stainless steel ( $\delta = 10$  mm), produced by laser-arc welding with Avesta 253MA electrode wire (1.2 mm in diameter) [9]

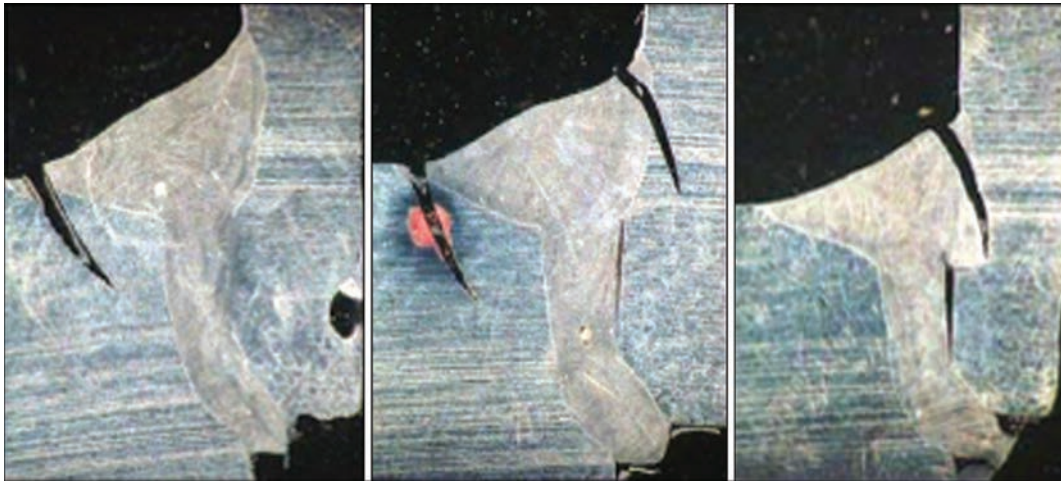


**Figure 5.** Propagation of longitudinal cracks and fracture of the joint during cyclic fatigue tests. Cross-section of fillet joints of steel SS2333, welded using laser-arc method [9]

hydrodynamics of weld pool, which would contribute to increasing the uniformity of chemical composition in the weld throughout its height even at significant (over 8 mm) thicknesses of welded edges, eliminating pore formation, and increasing quality of the fusion zone, improvement of resistance to cyclic alternating stresses. Such a control of hydrodynamics of the melt pool would become possible in case when an additional factor is introduced into the technological scheme of the process, which increases the intensity of the melt flows in a vertical direction [11]. In addition, this would provide additional possibilities for controlling the thermal cycle of the hybrid laser-arc welding process.

Our proposed approach to obtaining an effective method for controlling the hydrodynamics of a weld pool and, therefore, to improving the quality of laser-arc welding, consists in modernization of the existing technological scheme of laser-MIG welding and creating a new welding tool based on the principle of reciprocating movements (oscillations) of the laser radiation focus along the axis of the beam in the certain intervals of frequency and amplitude. The focus oscillations of, realized by reciprocating movements of the focusing lens, can be also additionally coordinated with a set pulsed mode of modulation of laser radiation and/or burning of the MIG arc during hybrid laser-MIG welding process.

To realize the proposed approach to changing the technological scheme of the laser-MIG welding process, an appropriate laboratory bench with welding head was created, which allows realizing a reciprocating movement (scanning) of the focus along the radiation axis with a frequency of up to 100 Hz and an amplitude of 0–10 mm. The principle of operation of such welding head is shown in Figure 6.

Laser radiation 1 is focused using lens 2 on the butt line of parts to be welded. Lens 2 is installed in

case 3 of focusing lens, which, in turn, is located in mandrel 4, having a possibility of reciprocating movement using the system 5. The system 5 provides a controlled scanning along the axis of radiation with a frequency  $f = 0\text{--}100$  Hz and an amplitude  $A = \pm(0\text{--}5)$  mm. This allows changing the location of focal plane of lens 2 relative to the surface of parts to be welded by the value  $\pm\Delta F$ , regulated by a change in the amplitude  $A$ . The composition of the system 5 for scanning laser radiation includes solenoids 6 and 7, with whose anchors 8 and 9 mandrel 4 is rigidly connected. The system 5 also includes rubber pads 10–13 for braking anchors of solenoids and control device 14, which includes a master pulse generator and an electric signal amplifier. For realization of the arc component of the laser-MIG welding process, the electrode wire feed is provided using the nozzle 15, which has the ability to adjust the position relative to the radiation focus and feed angle within the range of  $30\text{--}80^\circ$  relative to the radiation axis ( $10\text{--}60^\circ$  relative to welded butt surface).

We should note that the design of scanning lens (focus of radiation) shown in Figure 6 is considered as an example as one of the possible variants. Other variants of the design for such scanner are also possible. For example, the reciprocating movement of the lens along the axis of radiation can be carried out using piezoelectric motors or eccentric cams, driven into rotation by DC motors.

The action of the proposed device is as follows (see Figure 6). Laser radiation 1 by means of lens 2 is focused on the butt line of the parts to be welded with the desired deepening  $\Delta F$  of focal plane of the lens relative to the surface of parts to be welded. After applying an electric signal to solenoids 6 and 7 using control device 14, anchors 8 and 9 provide vertical reciprocating movements of mandrel 4 with casing 3 of focusing lens 2 with a frequency  $f = 0\text{--}100$  Hz and

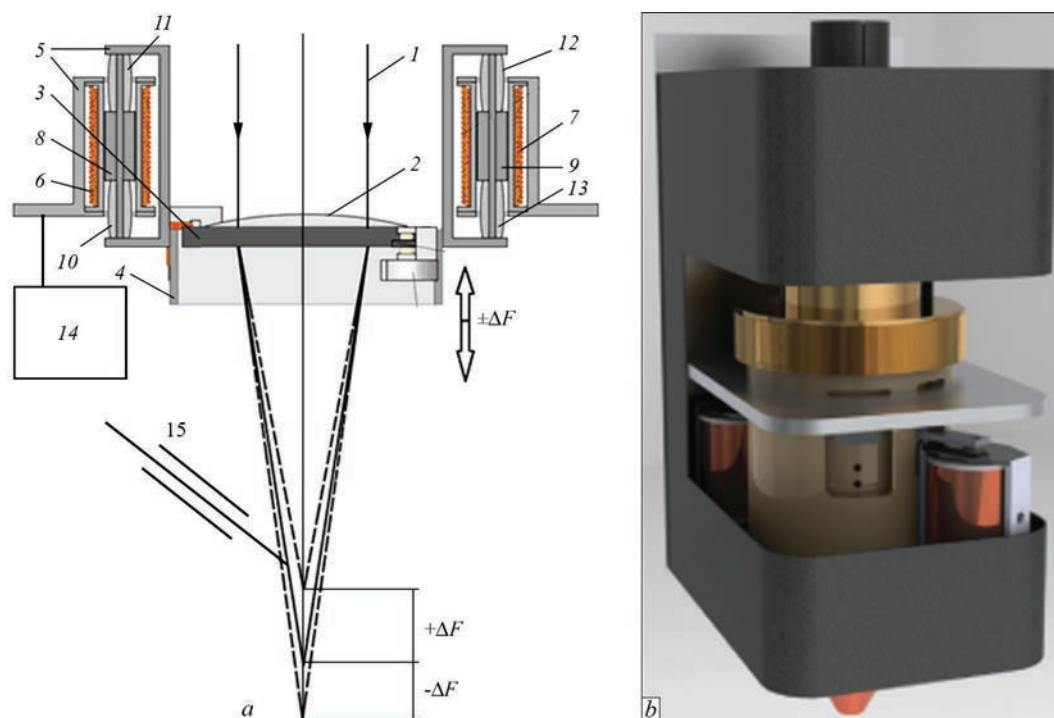


**Figure 6.** Scheme of design (a) and general appearance (b) of the head for laser and hybrid laser-MIG welding with the system of reciprocating movement (scanning) of the focus ( $\pm\Delta F$ ) along the axis of the radiation (designations see in the text)

amplitude  $A = \pm (0-5)$  mm, which provides the corresponding vertical focus oscillations. At the same time, rubber pads 10–13 soften and inhibit the movement of anchors.

After the start of vertical oscillations of the focus of laser radiation 1, the electrode wire is driven by the wire feed mechanism, the electric contact of which with the positive potential of the arc power source is performed using nozzle 15. After touching the electrode wire with a part to be welded under the negative potential of the source, an electric arc appears that is «attached» to an oscillating focus and also gets the opportunity to realize an oscillation movements. In the case of welding in the flat position, these are vertical oscillations. After this, the process of hybrid laser-MIG welding begins, in which due to the vertical scanning of the focus with certain frequency and amplitude, the effect of increasing the penetration depth without increasing the laser radiation power, as well as the effects of a more uniform weld alloying along the entire height of the metal electrode wire and eliminating the formation of inner pores are achieved by improving the conditions for the floating of gas bubbles on the weld pool surface.

Thus, the described technical solution for manufacturing head for laser-MIG welding with focus scanning along the axis of laser radiation provides new technological possibilities. These possibilities can be more fully revealed when the focus scanning frequency is increased, for example, during welding of steels to the optimum values of a pulsed effect on

the weld pool (as is shown in [12]), or to the values of the order of 500 Hz. Such a frequency of effect on the molten pool is threshold, after which the metal of the pool stops reacting to pulsed oscillations. In our opinion, in the long term, the proposed equipment and the technologies of hybrid welding implemented with the help of it, as compared to conventional laser-MIG welding, can have the following advantages:

- more than twice increase in the penetration depth without growing the power of laser radiation;
- possibility of welding loose adjacent edges due to oscillations of the arc of the consumable electrode during the welding process;
- possibility of increasing the welding speed by 2 or more times without increasing the radiation power;
- possibility of modifying the thermal cycle of welding, which helps to eliminate the formation of undesired quenching structures in welds;
- possibility of a more uniform weld alloying along its entire height by the metal of the electrode wire;
- reducing the risk of inner pores formation in the welds.

Verification of the effectiveness of the proposed method was performed at the E.O. Paton Electric Welding Institute by conducting the necessary experiments in the robotic laboratory bench created for this purpose (Figure 7). The bench consisted of anthropomorphic robot-manipulator for moving integrated head for laser-MIG welding, as well as the head itself, mechanism for electrode wire feed, electrical pow-



**Figure 7.** Appearance of robotic laboratory bench for laser arc welding with laser focus oscillations

er systems (including MIG power source, providing welding current of up to 500 A), control and supply of shielding gases. The integrated head for hybrid laser-MIG welding consisted of focusing system with a focus scanning along the axis of laser radiation and MIG torch. The vertical scanning system provided focusing of radiation by the lens with a focal length  $f = 300$  mm and vertical reciprocating oscillations of the lens with a frequency of 0–100 Hz and an amplitude of  $\pm(0-5)$  mm. The tests of this bench were carried out using radiation from a disc laser of the model TruDisc 10002 (TRUMPF Company) with a radiation power of up to 10.0 kW. In this case, penetrations and butt welds were produced in the flat position using specimens of  $300 \times 100 \times \delta$  mm in size of steels SM41B (09Mn2Si or 09G2S) of  $\delta = 4-18$  mm thickness, AN36 (A36) of  $\delta = 4-18$  mm thickness, and also SUS304 (08Kh18N10) with a thickness of  $\delta = 8-10$  mm using welding wires of the solid cross-section 08Mn2Si (Sv-08G2S) and 01Cr18Ni10 (Sv-01Kh18N10) with a diameter of 1.2 mm (Table 1).

**Table 1.** Chemical composition (wt.%) of materials of welded specimens and welding wires

| Material        | C           | Si         | Mn         | Cr         | Ni         | Ti         | Cu         | S           | P     | Other          |
|-----------------|-------------|------------|------------|------------|------------|------------|------------|-------------|-------|----------------|
| 09Mn2Si         | $\leq 0.12$ | 0.5–0.8    | 1.3–1.7    | $\leq 0.3$ | $\leq 0.3$ | –          | $\leq 0.3$ | $\leq 0.04$ | 0.035 | $N \leq 0.008$ |
| AH36            | $\leq 0.18$ | $\leq 0.5$ | 0.9–1.6    | –          | –          | –          | –          | 0.035       | 0.035 | –              |
| SUS304          | $\leq 0.8$  | $\leq 0.8$ | $\leq 0.2$ | 17–19      | 9–11       | $\leq 0.5$ | $\leq 0.3$ | 0.02        | 0.035 | –              |
| Wire 08Mn2Si    | 0.05–0.11   | 0.70–0.95  | 1.8–2.1    | 0.20       | 0.25       | –          | –          | 0.025       | 0.030 | –              |
| Wire 01Cr18Ni10 | 0.02        | 0.4        | 1.0–2.0    | 17.0–19.0  | 9.5–11.0   | –          | –          | 0.02        | 0.02  | –              |

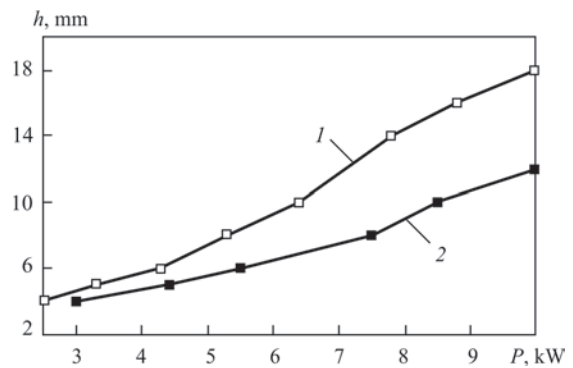


**Figure 8.** Dependence of the penetration depth  $h$  on the radiation power  $P$  during laser-MIG welding with focus scanning ( $f = 100$  Hz,  $A = 3$  mm) along the radiation axis (curve 1) and without scanning (curve 2)

During the experiments the results of welds formation during butt laser-arc welding of plates of the mentioned steels, produced in the flat position with and without vertical focus oscillation, were compared. In this case, the focus oscillation frequency was 100 Hz, and the amplitude was selected close to half of the thickness of welded edges. The focus was scanned so that its deepening relative to the top of the plates being welded in the upper position was 1–2 mm. Based on the results of the experiments, a diagram was plotted showing the dependence of the thickness of the edges of the welded sheets (penetration depth  $h$ ) of carbon steel on the laser radiation power during welding at a speed of about 80–90 m/h, welding current of about 220–250 A and arc voltage of 22–24 V (Figure 8).

Tests on static strength were carried out using the MTS Criterion 45.305 tensile testing machine (with a load of up to 300 kN) on the specimens of type XIII (XIIIa) (GOST 6996–66), which were cut out from butt welded steel plates of SUS304 steel with a thickness of  $\delta = 10$  mm. 3 groups of specimens were subjected to rupture tests — produced using laser-MIG welding with and without focus scanning, as well as cut out from the plates of base metal. Each group included 3 specimens; the obtained test results were averaged. The welded specimens were mostly ruptured identically — the upper ones to about 3 mm along the fusion line, then through the weld to the opposite fusion zone. The tensile strength of the specimens welded without a focus scanning was 620–640 MPa and with scanning — 630–650 MPa. For the base metal, the tensile strength was 640–660 MPa. Thus,

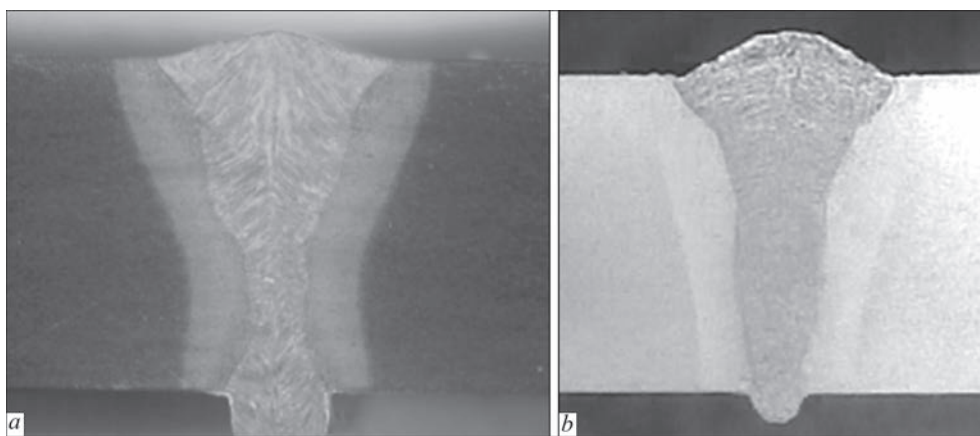


**Figure 9.** High-quality joints of high-strength steel 10 mm thick (*a*) and corrosion-resistant steel SUS304 8 mm thick (*b*), produced using focus scanning along the axis of radiation in hybrid laser-MIG welding

**Table 2.** Change in energy input of laser-MIG welding depending on thickness of welded edges

| Energy input<br><i>E</i> , kJ/m | Thickness of welded edges $\delta$ , mm |         |         |         |         |         |         |         |         |
|---------------------------------|---|---------|---------|---------|---------|---------|---------|---------|---------|
|                                 | 4                                       | 5       | 6       | 8       | 10      | 12      | 14      | 16      | 18      |
| Without scanning                | 320–330                                 | 390–400 | 440–450 | 520–540 | 570–590 | 640–650 | –       | –       | –       |
| With scanning                   | 300–320                                 | 340–360 | 390–410 | 430–450 | 480–500 | 510–530 | 550–560 | 590–610 | 650–670 |

the strength of welds produced by welding without scanning amounted to about 98–99 % relative to the base metal, and with scanning to 99–100 %.

To carry out metallographic examinations according to standard procedures, the specimens of cross-sections of the produced welds were prepared, which were studied with the use of the Neophot-32 optical microscope at magnifications of up to 1500 times. As a result, it was found that introduction of focus scanning along the axis of radiation improves the formation of welds and increases the uniformity of their alloying with the metal of the electrode wire over their height (Figure 9). In addition, the size of dendrite grains of the cast zone of the welds is reduced as compared to conventional hybrid laser-MIG welding.

It can be assumed that overheating and increase in the volume of remelted metal, as well as increase in the penetration depth in case of introducing focus oscillations along the radiation axis at a fixed radiation power, lead to improvement in the absorption of laser radiation and increase in the efficiency of welding. The input energy of laser-arc welding is reduced by about 15–20 % (Table 2). The carried out experiments showed that the use of vertical focus oscillations allows increasing penetration depth by 20–50 % without increasing the radiation power. The effect of increasing penetration depth due to scanning of the radiation focus becomes noticeable at thicknesses larger than 4–5 mm and affects the more, the thicker the welded edges. This allows performing laser and hybrid welding of the edges of metal parts of significant

(up to 10 and up to 18 mm, respectively) thicknesses with a minimal consumption of laser radiation power (for example, up to 6.0 kW).

## Conclusions

1. A new approach to laser and laser-arc welding, which consists in supplementing the existing technological schemes of processes by scanning the focus along the axis of laser radiation with a certain frequency and amplitude, allows increasing the intensity of melt flows in the weld pool (including vertical direction) and further modifying the thermal cycle of welding, which increases the uniformity of distribution the alloying additives along the height of the weld, minimizes the risk of formation of inner pores and at the same time by 20–50 % increases the efficiency of the process and reduces its energy input by at least 15–20 %.

2. An increase in the efficiency of laser and laser-arc welding can consist in either an increase in the speed of the process, or in the possibility of welding edges of larger thickness without increasing the energy input. In this case, the effect of increasing the penetration depth due to scanning the radiation focus becomes noticeable at the thicknesses over 4–5 mm and affects the more, the thicker the welded edges.

3. Mechanical tests showed that tensile strength of corrosion-resistant steel joints produced by laser-arc welding with a focus scanning along the radiation axis approximately corresponds to the strength of the base metal. Metallographic examinations showed an improvement in the formation of welds, an increase in

the uniformity of their alloying with the metal of the electrode wire in height, a decrease in the grain size of the dendrites of the cast zone of the welds as compared to the conventional hybrid laser-MIG welding.

4. To increase the efficiency of the proposed approach to laser and laser-arc welding, it is advisable to optimize the frequency and amplitude of focus scanning along the axis of the laser radiation.

*Note. The work was carried out in the framework of the Project No.2018GDASCX-0803 «Research and development of laser and plasma technologies for hybrid welding and cutting», Guangzhou, China.*

1. Grigoryants, A.G., Shiganov, I.N. (1988) *Laser technique and technology*. In: 7 books. Book 5: Laser welding of metals. Ed. by A.G. Grigoryants. Moscow, Vysshaya Shkola [in Russian].
2. Vvedenov, A.A., Gladush, G.G., Yavokhin, A.N. (1983) On mechanism of maintain of deep key hole in liquid using laser beam. *PMTF*, **1** 48–41 [in Russian].
3. Oikawa, M., Minamida, K., Yoshida, Y., Suzuki, N. (2004) Development of all laser welded honeycomb structure for civil transports. *Nippon Steel Technical Report*, **89**, January, 96–101.
4. Shelyagin, V.D., Khaskin, V.Yu. (2002) Tendencies in development of laser-arc welding (Review). *The Paton Welding J.*, **6**, 25–28.
5. Shelyagin, V.D., Khaskin, V.Yu., Garashchuk, V.P. et al. (2002) Hybrid CO<sub>2</sub>-laser and CO<sub>2</sub> consumable-arc welding. *Ibid.*, **10**, 35–37.
6. Engström, H., Nilsson, K., Flinkfeldt, J. et al. (2001) Laser hybrid welding of high strength steels. In: *Proc. of ICA-LEO 2001, 20th Int. Congress on Applications of Lasers & Electro-Optics (October 15–18, 2001, Jacksonville, Florida, USA)*. Ed. Xiangli Chen, Laser Institute of America, 2001, 125–134.
7. Unt, A., Poutiainen, I., Salminen, A. (2015) Influence of filler wire feed rate in laser-arc hybrid welding of T-butt joint in shipbuilding steel with different optical setups. *Physica Procedia*, **78**, 45–52.
8. Frostevarga, J., Kaplan, A. F.H. (2014) Undercuts in laser arc hybrid welding. *Ibid.*, **56**, 663–672.
9. Alam, Md. M. (2009) *A study of the fatigue behaviour of laser and hybrid laser welds* (Licentiate thesis). Luleå, Luleå Tekniska Universitet, **133**.
10. Krivtsun, I.V., Khaskin, V.Yu., Korzhik, V.N., Ziyi Luo (2015) Industrial application of hybrid laser-arc welding (Review). *The Paton Welding J.*, **7**, 41–46.
11. Golubev, V.S. (2009) Hydrodynamic phenomena in laser welding with channeling penetration of radiation. In: *Deep channeling and filamentation of power laser radiation in substance*. Ed. by V.Ya. Panchenko. Moscow, Intercontact Nauka, 35–63 [in Russian].
12. Khaskin, V.Yu., Pavlovsky, S.Yu., Garashchuk, V.P. et al. (2001) Peculiarities of welding thin-sheet low-carbon steels using a pulsed-periodic radiation of CO<sub>2</sub>-laser. *The Paton Welding J.*, **2**, 42–46.

Received 21.10.2019

WORLD TRADE FAIR FOR WELDING ENGINEERING —  
JOINING, CUTTING, SURFACING

LET'S JOIN  
THE WORLD!

13. – 17. September, 2021

REGISTER NOW!

www.schweissen-schneiden.com

DVS GERMAN WELDING SOCIETY

MESSE ESSEN

## ARC AND PLASMA-POWDER SURFACING OF SEALING SURFACES OF PUMP IMPELLERS

O.S. Kostornoy and M.O. Laktionov

JSC «Research and Design Institute of Nuclear and Power Pump Construction»  
2 2nd Zaliznychna Str., 40003, Sumy, Ukraine. E-mail: kostornoy@vniiaen.sumy.ua

Technology of gas-shielded robotic arc surfacing of sealing surfaces of pump impellers with flux-cored wire of ARTINIT DUR 500 grade was developed. Corrosion resistance testing of deposited metal of this type according to GOST 9.912–89 showed that it is on the level of 12Kh18N12M3TL steel. Application of flux-cored wire ARTINIT DUR 500 for surfacing these parts is envisaged by the respective standards: GOST 31901–2013 (Appendix H) and GOST 33258–2015 (Appendix B). Technology of plasma-powder surfacing of sealing surfaces of pump impellers in automatic unit PM-302 with application of powders of cobalt alloys (stellite) was also developed. A particular method of surfacing the sealing surfaces of pump impellers is selected proceeding from the conditions of their operation and economic parameters. 9 Ref., 2 Figures.

*Keywords:* plasma-powder surfacing, arc surfacing, surfacing of sealing surfaces, deposited metal types, flux-cored wire for robotic surfacing

In hydraulic units the joints of movable parts are widely used, which are made with a guaranteed small gap and provide a mutual movement of parts and a certain degree of sealing without the use of special seals and tools. Such a seal, called a groove seal, represents a capillary groove, at the appropriate size and length of which the necessary resistance to the flow of fluid can be created. Their sealing effect is based on the use of hydraulic resistance of annular throttles with a small radial gap. A radial gap is considered to be minimal, in case that reliable assembly and operation of the rotating and stationary elements of the pump are provided without the metal contact.

During operation of the pumps, the surfaces joined in the sealing zone can be destroyed as a result of corrosion and erosion effects of the flow of working environment. Inaccuracies during the assembly of pump units, deformation of shafts and impellers during operation can lead to local contacts of groove sealing surfaces, which causes mechanical wear of groove sealing surfaces by friction forces. The abovementioned factors are the main causes of premature failure of equipment.

Based on the conditions of pumps operation, the sealing surfaces of impellers should meet the following requirements:

- be resistant to erosion damage when exposed to the flow of the working environment;
- have a high resistance to fretting and adhesion of contact surfaces;
- be resistant to general and intercrystalline corrosion;

- maintain structural stability in the conditions of contact friction and heating.

At the same time it is necessary to take into account the economic and technological parameters of the materials used.

In the designs of pumps for nuclear and heat power engineering, oilfield equipment and chemical industry, the impellers of steels 10Kh18N9L, 12Kh18N-12M3TL and the like are widely used. At present, the main way of producing reliable sealing surfaces of a pump impeller is surfacing with wear-resistant and corrosion-resistant materials. The experience was gained in the use of three types of materials for deposition of sealing surfaces of pump impellers made of the mentioned steels [1].

The first type includes electrodes of grade TsN-6L and flux-cored wire PP-AN133 [2], which provide a production of deposited metal of type 08Kh17N8S6G. They have satisfactory welding and technological properties. The metal deposited with the use of electrodes TsN-6L and wire PP-AN133 has a relatively low susceptibility to cracking.

The second type of surfacing materials, which includes electrodes TsN-12M and flux-cored wire PP-AN157 [2], provides a deposited metal of type Kh16N8M5S5G4B with a higher hardness and, accordingly, resistance to fretting and adhesion in the contact zone, as compared to the first type. However, a high susceptibility of such metal to cracking requires high temperatures of product heating during surfacing and immediate heat treatment after surfacing.

During surfacing stop valves and pump impellers, stellites are also used. These are cobalt-based alloys which can be attributed to the third type of surfacing

materials used for these purposes. The deposited metal of this type provides the best set of necessary properties — resistance to erosion and corrosion, excellent wear resistance during friction of metal against metal and structural stability in the process of heating during friction [3].

The stage centrifugal pumps TsNS-180 for pumping water into oil reservoirs with the purpose of maintaining pressure in a reservoir are in series production. The reservoir water is quite aggressive and therefore for manufacture of TsNS pumps the steel 12Kh18N12M3TL is used. The surfaces of impellers in the areas of groove seals were previously surfaced by manual argon arc welding with cobalt based rods of grades Pr-V3K or Stellite 6. The surfacing process envisaged a high preheating (550–650 °C) and immediate heat treatment after surfacing.

In order to optimize the surfacing process, the work was carried out aimed at solving the following tasks:

- increasing the labour efficiency;
- reducing the temperature of preliminary and accompanying heating of products during surfacing;
- improving working conditions of welders;
- reducing the costs for purchasing surfacing materials.

For automatic arc surfacing of sealing surfaces of impellers of rotary stage centrifugal pumps of TsNS-180 type, the wire of grade ARTINIT DUR 500 of the Bohler Company was selected. Welding and technological properties of the wire were evaluated during argon arc surfacing of separate beads on the plates of steels 12Kh18N10T and 12Kh18N12M3TL. The optimum welding mode was determined at which minimum spattering is observed. For measurements of

hardness on 16 mm thick plates of steels 12Kh18N10T and 12Kh18N12M3TL, surfacing was performed in one, two and five layers. The hardness of deposited metal in the initial state and after heat treatment was measured at different temperatures. Heat treatment can increase the hardness of deposited metal; the most significant increase in hardness by 10–15 units of *HRC* is observed during heat treatment in the temperature range of 500–550 °C. At the temperatures above 860 °C, the strength of deposited metal may be reduced — coagulation of secondary carbides occurs, resulting in a decrease in the hardness of deposited metal.

The microstructure of the deposited metal in the initial state consists of austenite and ferrite (more than 50 % of the ferrite phase). Heating and holding at 550 °C did not lead to significant changes in the microstructure. The formation of excessive secondary phases is observed mainly along the boundaries and inside the ferrite regions.

The tests of the deposited metal for corrosion resistance were performed according to the instruction ITsK-01–99 (determination of weight losses) and in accordance with GOST 9.912–89 [4]. The corrosion resistance of the deposited metal was found at the level of steel 12Kh18N12M3TL.

To specify the technology, surfacing of a full-scale specimen, simulating the groove geometry and the impeller diameter in the surfacing area, was performed. Surfacing was performed without a preheating, of temperature of the specimen between surfacing of separate layers did not exceed 400 °C. After surfacing, slow cooling of the specimen was provided.

Visual inspection and colour flaw detection were performed after sequential grinding of deposited metal to a thickness of 0.5 mm. At the thickness of deposited layer of 2.5 mm a finish grinding was performed. No defects of deposited metal were detected by visual inspection and flaw detection testing. The hardness of the deposited metal in the initial state is *HRC* 40–43, after heat treatment at 860 °C *HRC* is 43–47.

The developed robotic and mechanized technology of argon arc surfacing of sealing surfaces of stage centrifugal pump impellers with the use of flux-cored wire of grade DUR 500 was introduced into production. Currently, the application of the flux-cored wire ARTINIT DUR 500 for surfacing is envisaged by the standards: GOST 31901–2013 (Appendix H) [5] and GOST 33258–2015 (Appendix B) [1].

Plasma-powder method is also used for surfacing sealing surfaces of pump impellers. A great advantage of this method is negligible stirring of deposited metal with base metal (3–8 %) and the possibility of surfacing thin layers (0.5–3.0 mm). Due to a low penetra-



Figure 1. Installation PM-302 for plasma-powder surfacing

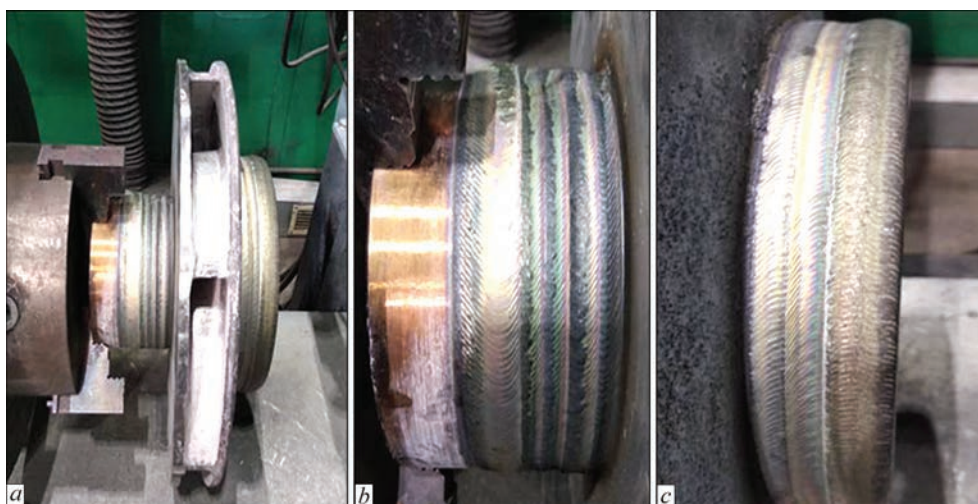


**Figure 2.** Plasma-powder surfacing of pump impeller (a) and appearance of deposited surface on small (b) and larger (c) diameters of impeller

tion of base metal, the required hardness and specified chemical composition of deposited metal are provided already in the first deposited layer [6–8].

In this case, as surfacing materials the alloy powders based on cobalt (stellites) and nickel (colmonoys) are used. In our experiments, a cobalt-based Stellite 6 alloy was used.

For surfacing the sealing surfaces of pump parts, a universal automated installation PM-302 for plasma-powder surfacing, manufactured by Plasma Master Company, was used (Figure 1).

Before surfacing, the operator of the installation PM-302 introduces the basic process parameters: direct arc current, powder consumption rate, surfacing speed, amplitude and oscillation frequency of the plasmatron, displacement of the arc from zenith and distance from the plasmatron to the product, gas consumption: plasma-forming one, transporting powder and shielding one. The selection of parameters depends on the size of the surfacing layer, dimensions and design of products and thermophysical properties of base and filler material. The criteria of optimality of the selected modes are a good formation of deposited bead, minimal penetration of base metal and absence of defects in the deposited layer (cracks, pores, nonmetallic inclusions, etc.).

Surfacing of sealing surfaces of pump impellers in the installation PM-302 is performed in an automatic mode, which provides a high quality of deposited surfaces (Figure 2). Visual inspection and colour flaw detection showed that there were no defects in deposited metal.

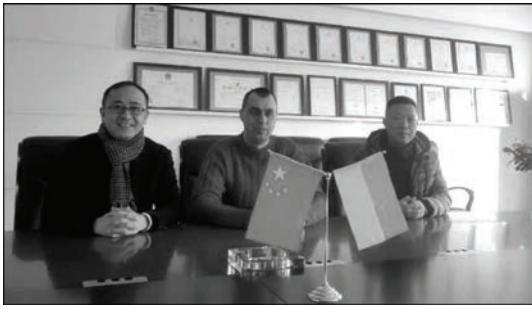
## Conclusion

The technology of gas-shielded robotic arc surfacing of sealing surfaces of pump impellers with flux-cored wire of ARTINIT DUR 500 grade was developed. The technology of plasma-powder surfacing of these parts in automatic unit PM-302 with application of powder of cobalt alloy Stellite 6 was also developed. Both methods provide a high efficiency and a high quality of deposited metal at a low consumption of expensive surfacing materials and minimal costs. The choice of the method of surfacing sealing surfaces of pump impellers is made on the basis of their operating conditions and economic indicators.

1. (2015) *GOST 33258–2015*: Pipeline valves. Surfacing and quality control of surfaced surfaces. Technical requirements [in Russian].
2. (1979) *Surfacing materials of countries-members of CMEA*: Catalogue. Ed. by I.I. Frumin. Kiev-Moscow, Int. Center of Sci. and Techn. Information [in Russian].
3. Gladky, P.V., Pereplyotchikov, E.F. (1997) Properties of cobalt-chrome-tungsten surfacing alloys doped with boron and nickel. *Avtomatich. Svarka*, **7**, 14–28 (in Russian).
4. (1989) *GOST 9.912–89*: United system of corrosion and ageing protection. Corrosion resistant steels and alloys. Methods of accelerated tests for resistance to pitting corrosion [in Russian].
5. (2013) *GOST 31901–2013*: Pipeline valves for nuclear stations. General specifications [in Russian].
6. Pereplyotchikov, E.F. (2007) *Plasma-powder surfacing in valve manufacturing*. Kiev, Ekotekhnologiya [in Russian].
7. Gladky, P.V., Pereplyotchikov, E.F., Ryabtsev, I.A. (2007) *Plasma surfacing*. Kiev, Ekotekhnologiya [in Russian].
8. Ryabtsev, I.A., Senchenkov, I.K., Turik, E.V. (2015) *Surfacing. Materials, technologies, mathematical modeling*. Gliwice, Silesia Polytechn. Inst.

Received 24.10.2019

## INTERNATIONAL COOPERATION



During the negotiations, from left to right: Gao Fen, Director General of New Huayang Company, P.S. Shlenskii, Director of Scientific-Engineering Center «Explosion Treatment of Materials», Li Jingwei, Explosion Welding Production Manager of New Huayang Company

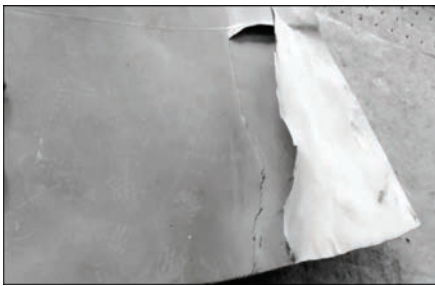
In 2019 by the initiative of China-Ukraine E.O. Paton Institute of Welding (CUIW), specialists of the E.O. Paton Electric Welding Institute of the National Academy of Sciences of Ukraine (PWI) and Guangdong Association for Science and Technology (Guangzhou, PRC) business contacts were established and a cooperation agreement was signed between PWI and Chinese Company Liaoning New Huayang Weiye Equipment & Manufacturing Co., Ltd (New Huayang), Tieling, Liaoning Province, PRC. In July and November-December 2019 PWI specialist travelled to China, in order to discuss a number of tasks on the explosion welding technology, which are to be jointly solved.

New Huayang Company is located in the high-tech industrial zone of Tieling City. It is a limited liability company reorganized from the Shenyang Titanium Equipment Plant, founded in 1988. In PRC territory the Company is one of the pioneers in the field of explosion welding with more than 30 years experience of operation.

The Company has two production shops — the Eastern and Western one, and its own explosive storage and an open site for performance of explosion welding operations with the allowed blasting mass of 500 kg of explosive in TNT equivalent. At present the following bimetals are produced: steel + stainless steel, steel + titanium, steel + copper alloys. The Company is one of the few enterprises in the world, which make bimetal plates of about 20 m<sup>2</sup> area. In the near future it is planned to increase the plate area up to 33 m<sup>2</sup>. Achieving such a result will bring the Company closer to achievements of leading world producers. A feature of New Huayang Company is the fact that the produced bimetal is not only sold to customers, but is also extensively used in domestic manufacturing of chemical and petroleum equipment.

By the results of the first visit (July, 2019) of PWI specialist to New Huayang Company, the first contract was signed for rendering the scientific-consultation services on supporting the explosion welding technology.

In November-December 2019 within the scope of the contract, PWI specialist performed studies of the detonation properties of explosives used by the Company in explosion welding operations.



Defects in titanium-steel bimetal production

Until recently, the New Huayang Company performed explosion welding with explosive of one composition that does not allow welding a broad range of bimetals.

In this connection, special experiments were performed on measurement of the detonation velocities of mixtures of this explosive with different percentage of salt (NaCl) and sand, at different charge heights.

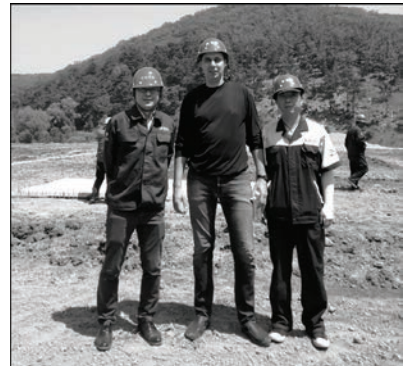
As a result of the performed work, the New Huayang Company was able to regulate (control) the velocity of detonation in a specified

layer of explosive during performance of explosion welding operations that, in its turn, improved the finished product quality.

As such defects as violation of the cladding layer integrity can develop in production of the bimetal by explosion welding, model experiments were conducted to determine the possibility of restoration (repair) of titanium-steel bimetal.

The conducted experiment showed the possibility of restoration of a defective bimetal plate and its application in further work that, in its turn, will allow improving the production cost-effectiveness.

The directions of further joint work were discussed, which implies signing a new contract.



In the production site



Appearance of bimetal after restoration

P.S. Shlenskii, Gao Fen